

**STUDIES OF THE RELATIONSHIP
BETWEEN SUBMICRON MARINE
AEROSOL AND INITIAL MARINE
STRATUS PROPERTIES**

**by: Tara L. Jensen-Leute and Sonia M. Kreidenweis
Department of Atmospheric Science
Colorado State University
Fort Collins, CO 80523**

Funding Agencies:

**National Aeronautics & Space Administration,
Global Change Fellowship Under
Training Grant Number NGT-30106
Colorado State University Faculty Research Grant**

**Colorado
State
University**

**DEPARTMENT OF
ATMOSPHERIC SCIENCE**

PAPER NO. 545

**STUDIES OF THE RELATIONSHIP BETWEEN SUBMICRON MARINE
AEROSOL AND INITIAL MARINE STRATUS PROPERTIES**

**Tara L. Jensen-Leute
Sonia M. Kreidenweis
Department of Atmospheric Science
Colorado State University
Fort Collins, CO 80523**

Research Supported by

**NASA Global Change Fellowship
under NASA Training Grant Number NGT-30106**

and

Colorado State University Faculty Research Grant

December, 1993

Atmospheric Science Paper No. 545



018401 9558997

34 292CSU XL2 1540
08/02 28-000-01



QC
852
.C6
NO. 545
ATMOS

ABSTRACT

STUDIES OF THE RELATIONSHIP BETWEEN SUBMICRON MARINE AEROSOL AND NITIAL MARINE STRATUS PROPERTIES

A systematic study of the relationship between submicron aerosols and the marine stratus cloud properties has been undertaken. The first part of the study included participation in the Atlantic Stratocumulus Transition Experiment - Marine Aerosol and Gas Exchange (ASTEX/MAGE) cooperative research experiment. Measurements of submicron marine aerosol were collected using the Differential Mobility Particle Sizing (DMSP) system for determining the typical chemical composition and aerosol size distribution of marine aerosol. The second part of the investigation involved cloud process simulation with the Colorado State University dynamic cloud chamber.

Marine aerosol distribution measurements were taken over a 25 day period from June 1 to June 25, 1992. Analysis of the data showed that the distributions were generally bimodal in clean air masses with total number concentrations ranging from 100 to 900 particles cm^{-3} , while distributions were generally monomodal in polluted air masses with total number concentrations ranging from 800 to 1400 particles cm^{-3} .

Using the "typical" thermodynamic and aerosol characteristics observed during the field project, the Colorado State University dynamic cloud chamber was used to conduct a well controlled study of the effects of submicron aerosol on the formation of marine stratus type clouds. Selected size distributions of ammonium sulfate were injected into the chamber and exposed to adiabatic expansions that simulated typical

marine updraft velocities. Observations from the experiments were compared to model predictions from a one dimensional cloud model as well as other published modeling results.

The dynamic cloud chamber, as configured for this study, was shown to be suitable for use in making stratus cloud simulations at updraft velocities greater than 1.0 m s^{-1} . Mean diameter, liquid water content and dispersion coefficient values appeared to be comparable to the model predictions. Nucleated aerosol fraction trends agreed with model results. Details of the design, implementation and data interpretation are presented.

ACKNOWLEDGEMENTS

Tara Jensen Leute:

I would like to thank my advisor, Dr. Sonia Kreidenweis, for her assistance, guidance, and availability over the past two years. Also, the opportunity she provided for me to gain valuable experience in the field and the laboratory was infinitely appreciated. I would also like to express my gratitude to Professor Lewis Grant and Dr. Carol McConica for the valuable ideas they shared.

I extend a heartfelt thanks to Dr. Paul DeMott and Dr. David Rogers for their thought provoking questions, excellent guidance in the use of the Colorado State University dynamic cloud chamber, and programming assistance. I could not have completed this work without the assistance of Brian Jesse. His ingenious technical assistance, long hours and late nights in getting ready for both the field project and in conducting the chamber experiments were greatly appreciated. Thank you to all three for their patience with my insistence that either the dynamic cloud chamber was possessed or it just didn't like my aura. My appreciation goes to Debra Youngblood and Wendy Richardson for allowing me to vent my frustrations on sympathetic ears and for always giving me a mental break just when I needed one.

I would like to thank Dr. Young Kim, Dr. Herman Sievering, and Dr. Alex Pszenny for sharing the data they collected during the ASTEX/MAGE field project.

I am grateful to Dr. Abdul Alkezweeny for convincing me that atmospheric chemistry was an excellent subject to pursue. I also thank Dr. Tony Grainger, Leon Osborne, Dr. Ron Rinehart, Dr. Don Burrows, Dr. Jeff Stith, Erwin Prather, Fred Remer, Jon Ness, and Roger Tilbury for assisting me in gaining the self confidence and knowledge necessary to survive graduate school.

I extend a thank you to Jane Wilkins and Sandy Progen for their friendship and administrative assistance. I would also like to thank Judy Gueswel, Stephanie Ouren and Marilyn Gross for patiently answering all of my questions about purchase orders and other pertinent issues. I extend my sincere gratitude to Kris Das for skillfully arranging all of my travel, even when the dates changed at the last minute.

I extend a thank you to John and Mindy Knowles for their continuing friendship and support over the past two years. I am also grateful to John and Mindy, as well as Steve and Cathy Finley, Debra Youngblood and Jerry Harrington, for welcoming me into their homes while I was finishing up this work.

My loving appreciation goes to my father and mother, Dale and Joanne Jensen, and my sister, Kim Jensen, for their moral and emotional support they have always given to me. Also, thank you for caring enough to attempt to understand the concepts of my research.

I conclude by thanking my husband, Tony, for helping me with the big decisions and for understanding my desire to finish this project. His love, support and faith in me has been infinitely important to me over the past two years.

I gratefully acknowledge the support of a NASA Global Change Fellowship.

Sonia M. Kreidenweis:

Portions of this work were supported by a Colorado State University Faculty Research Grant.

TABLE OF CONTENTS

Chapter 1	Introduction	1
1.1	Background	1
1.2	Objectives	2
1.2a	Goals of Field Project	3
1.2b	Goals of Field Project	3
1.3	General Approach	4
Chapter 2	Literature Review	6
2.1	Marine Aerosol Measurements (Atlantic Ocean)	6
2.2	CCN Activation	7
2.2a	Theoretical Investigations	7
2.2b	Modeling Studies	9
2.2c	Natural Cloud Studies	11
2.2d	Cloud Chamber Studies	13
Chapter 3	Marine Aerosol Measurement - Project Description and Results	16

3.1	Purpose	16
3.2	Experimental Design	17
3.2a	General Approach	17
3.2b	Instrumentation	20
3.2c	Procedure	25
3.3	Instrument Limitations and Data Correction	27
3.3a	Diameter Range Limitation	27
3.3b	Counting Statistics	27
3.3c	Aerosol Dryness	29
3.3d	Tubing Losses	30
3.4	Results	32
3.4a	Behavior of System	33
3.4b	Data	36
3.4c	Observations	41
3.5	Summary	44
Chapter 4	Cloud Chamber Study - Project Description and Results	45
4.1	Purpose	45
4.2	Experimental Design	46
4.2a	General Approach	46

	4.2b Instrumentation	54
	4.2c Procedure	58
	4.3 Instrument Limitations and Data Correction	61
	4.3a DMA	61
	4.3b Cloud Chamber	62
	4.3c FSSP	65
	4.3d Dewpoint Hygrometers	68
	4.4 Results	69
	4.4a Thermodynamics	69
	4.4b. Microphysics	76
	4.4c Case Studies	90
	4.5 Summary	105
Chapter 5	Conclusions	109
Chapter 6	Recommendations for Future Research	113
	6.1 Marine Aerosol Measurement	113
	6.1a Data Set	113
	6.1b Technologic Improvements	114
	6.2 Cloud Chamber Studies	115
	6.2a Data Set	115

	6.2b Technologic Improvements	115
	6.2c Other Suggestions	117
References		118
Appendix A	Instrumentation	123
Appendix B	Forward Scattering Spectrometer Probe (FSSP) Velocity Acceptance Ratio and Sample Volume Relationship	134
Appendix C	Forward Scattering Spectrometer Probe (FSSP) Calibrations	151
Appendix D	Differential Mobility Particle Sizer (DMPS) Theory	168
Appendix E	Cloud Chamber Experimental Procedures	177

LIST OF SYMBOLS

N or n	number concentration
S	supersaturation
S_c	critical supersaturation
σ	fractional uncertainty
σ	dispersion coefficient
Q	CNC flow
t	time
c_p	specific heat at constant pressure
T	temperature
α	density of air
p	pressure
z	height above ground
g	gravity
Γ	dry adiabatic lapse rate
Γ_s	moist adiabatic lapse rate
L	latent heat of condensation
w_s	saturation mixing ratio
R	gas constant
θ	potential temperature
i	degree of ionic dissociation
m_v	molecular weight of water
M	mass of solute
ρ_L	density of water
m_s	molecular weight of solute
$\overline{D_d}$	geometric mean droplet diameter
D_d	diameter midpoint of each diameter bin
$[N_d]$	total droplet concentration
$[N_a]$	total aerosol concentration
S	standard deviation
c	constant defined by air mass type (see Table 2.1 on pg. 8)
k	0.286
ϵ	0.622

CHAPTER 1

INTRODUCTION

1.1 Background

In the past, cloud physicists have concentrated more on convective clouds than on stratiform clouds. One possible reason for this may be the difficulty of taking representative measurements in the wide-spread cloud layers of a stratiform cloud region, which often cover areas of 10^6 km² and may last for several days. Recently, however, stratiform clouds have come under increasing attention because of their importance in determining the global energy budget. Of particular interest is the relationship between aerosol size and number concentration and cloud microphysical properties because of the impact on radiative properties of these clouds.

Aerosol particles may indirectly impact the global energy budget by affecting the microphysics of clouds, including their role in the formation of precipitation. Drop size distributions and total number concentration are initially determined by the fraction of aerosol particles that act as cloud condensation nuclei (CCN). Changes in drop size distributions may alter cloud radiative properties (Twomey, 1977; Charlson et al., 1987; and Penner et al., 1991). Aerosols have also been shown to affect formation of drizzle and precipitation and thus impact the fractional cloudiness observed (Albrecht, 1989). Clouds in marine regions have been shown to be sensitive to changes in aerosol number loading (Hegg et al., 1984 and Radke, 1989). Approximately two-thirds of the Earth's

surface is covered by marine regions. Therefore, changes caused by aerosol loading and updraft velocity in marine cloud microphysical structure and longevity could impact the global energy budget.

Making accurate measurements of CCN is an important part of understanding the relationship between aerosol and cloud properties. Submicron aerosol, especially those in the diameter range of 0.1 μm to 1.0 μm in diameter, represent a significant portion of the particles activated as CCN. Although differential mobility analyzers (DMAs) have been used in several studies that investigate the role of submicron aerosols and marine stratus in the global energy budget (i.e., Hegg, 1993), the commercial version of the Differential Mobility Particle Sizer (DMPS) system (manufactured by Thermo Systems Inc. (TSI), St. Paul, MN.) has been used infrequently for measurements pertaining to stratiform clouds. This thesis details measurements of submicron aerosol taken with the DMPS in the field and laboratory and applies this information to the study of the impact of submicron marine aerosol on marine stratiform clouds. The validity of using the Colorado State University dynamic cloud chamber (see Appendix A for a full description) for studies of a marine nature is also discussed, and observations on the effect of submicron aerosol number loading and variations in updraft velocity are presented.

1.2 Objectives

The objective of this thesis was to conduct a well characterized study of the effect of submicron marine aerosol on stratus cloud properties. To attain this goal, a combined approach of field, lab and numerical studies was employed. First, a system including the TSI DMPS system was devised for use in measurement of submicron aerosol in both the

field and the laboratory. Second, the CSU dynamic cloud chamber's capability of performing slow updraft, low concentration experiments similar to marine conditions was determined. Finally, information on the effect of submicron aerosol number loading and variations in updraft velocity on marine stratus clouds was acquired.

1.2a Goals for Field Project

The primary objective of the field study was to support the overall Marine Aerosol and Gas Exchange (MAGE) program objectives by providing submicron aerosol size spectra. In the process, the following were specific CSU goals:

- 1) Ascertain the ability of the DMPS system to measure submicron aerosol size distributions.
- 2) Develop a description of a typical North Atlantic marine atmospheric environment including air temperature, dewpoint temperature, and submicron aerosol size distribution and composition for use in laboratory simulations of the role of marine aerosols on initial cloud properties

1.2b Goals for Laboratory Study

The primary objective of the laboratory study was to investigate the formation of marine stratus clouds on submicron aerosol injected into the CSU dynamic cloud chamber. This was done by using the ASTEX/MAGE data as a template for the injected aerosol distribution and initial "surface" conditions. First, it had to be determined

whether a study of this nature is feasible in the cloud chamber. Once this was done, the specific laboratory objectives were to:

- 1) Determine how cloud droplet spectra vary with submicron aerosol number loading and variations in updraft velocity.
- 2) Determine minimum boundaries on updraft velocity, number concentration and feasible aerosol distributions for use in future studies of this nature.

1.3 General Approach

In the first part of the study, a particle sizing system, referred to as the DMPS system and consisting of a DMA, a condensation nucleus counter (CNC), a dry, compressed air supply, and computer controlled data acquisition system, was deployed on the NOAA ship *Malcolm Baldrige* in the summer of 1992. Aerosol size distributions were measured in support of the Atlantic Stratocumulus Transition Experiment - Marine Aerosol and Gas Exchange (ASTEX/MAGE) field experiment and compared with other shipboard measurements for quality assurance. Post-cruise laboratory studies established representative particle losses that were applied as corrections to the data. These data were then submitted to the ASTEX/MAGE data base.

In the second part of the study, the DMA was used to generate aerosol of known distribution which were used as CCN in the CSU dynamic cloud chamber. The injected aerosol size distribution was verified using the DMPS system. A series of experiments at various updraft velocities and initial submicron aerosol loadings was performed to test the performance of the chamber against theory. Initial conditions and aerosol loading was determined from the measurements taken during ASTEX/MAGE. Several

modifications to the chamber and previously established experimental approach were required for this investigation. The slow updraft experimental data were compared with the model simulations, which predict the number concentration, size distribution and statistics for a theoretical cloud activated from the experimental initial conditions.

The following sections review past scientific contributions and theoretical basis for the project. Details of the design, implementation and data interpretation for both of the project parts are then presented.

CHAPTER 2

LITERATURE REVIEW

2.1 Marine Aerosol Measurements (Atlantic Ocean)

Knowledge of the physical and chemical properties of marine aerosol is important because of the role they play in the global climate. Fitzgerald (1991) presented a review of the information already gathered on the physical and chemical composition of marine aerosol. He stated that examination of particles using electron microscopy showed that a high percentage of the nucleation and accumulation mode particles are similar in chemical form and structure to ammonium sulfate. Seinfeld (1986) stated that the typical distribution of atmospheric aerosol can often be divided into three modes. Particles in the nuclei mode, extending from 0.005 to 0.1 μm in diameter, form from condensation of hot vapors from combustion and from nucleation of atmospheric gas-phase species. The source of particles in the accumulation mode, from 0.1 to 1 μm in diameter, is from coagulation of nucleation mode particles and condensation of vapors onto existing particles. The coarse mode, from 1 to 100 μm in diameter, usually consists of man-made and natural dust particles.

Hoppel et al. (1990) discussed the typical submicron aerosol distributions found over the North Atlantic Ocean (near the Canary Islands). In remote marine areas, a typical distribution consisted of a bimodal curve with an average total aerosol concentration of 243 particles cm^{-3} . In areas where an air mass transition had taken

place, i.e. from remote marine to continental air masses, the aerosol distribution was found to be monomodal with an average concentration of approximately 747 particles cm^{-3} . Aerosol distribution measurements gathered during ASTEX/MAGE, described in Chapter 3, were made in a region in proximity to where Hoppel et al. made their measurements, and generally confirmed these observations.

2.2 CCN Activation

The atmosphere contains significant concentrations of micron and submicron particles which have the ability to take up water and serve as sites for cloud droplet condensation. The number and size of cloud condensation nuclei, CCN, available can affect the concentration and size distribution of the nucleated cloud droplets (Rogers and Yau, 1989). Aerosol number loading generally impacts the cloud droplet spectra positively. The larger the aerosol number loading, the higher the nucleated cloud droplet concentration (Hindman et al., 1977a; and Hobbs et al., 1980). Updraft velocity can also indirectly affect the number of nucleated cloud droplets by increasing the supersaturation of the air with respect to water (Warner, 1969 and Cooper, 1989). Twomey (1959), Mordy (1959), and Chuang and Penner (1990) have considered the contributions of both aerosol number loading and updraft velocities on the cloud droplet spectra. Their studies as well as many others are discussed in this section.

2.2a Theoretical Investigations

Twomey (1959) observed that theoretical calculations of cloud droplet nucleation based on updraft-induced supersaturations do not always agree with in-cloud

observations, particularly for low concentration of CCN. Variations in supersaturation (S) in a volume of ascending air is determined by two opposing forces: cooling during ascent and heating by condensation of water. The terms "updraft" and "vertical velocity" are generally used to represent the ascent rate of a parcel of air that eventually forms a cloud. Twomey (1959) calculated nucleated droplet concentrations at different updraft velocities and initial particle concentrations using the following equation:

$$N = c S^k \quad (2.1)$$

to investigate the combined effect of aerosol number loading and updraft velocity on the number of droplets nucleated. N is the number of droplets formed, S is the supersaturation, and the constants c and k were determined from experimental data, and represent the class of ambient air the cloud forms in; i.e., maritime or continental. Table 2.1 summarizes the results of the calculations and compares them to the observed values. N' and N'' represent calculations using an S determined from an underestimation and an overestimation of the condensational heating effect respectively.

Table 2.1.
Calculated and Observed Cloud Droplet Concentration

Spectrum Type		Clean Marine (obs/calc)	Polluted Marine (obs/calc)	Continental (obs/calc)
Droplet Conc. (cm ⁻³) at 0.1 m s ⁻¹	N'	25-35/35	25-35/59	<330/281
	N''	25-35/37	25-35/60	<330/310
Droplet Conc. (cm ⁻³) at 1.0 m s ⁻¹	N'	35-40/57	65-90/87	330-560/500
	N''	40-50/61	65-90/89	330-560/554
Droplet Conc. (cm ⁻³) at 10.0 m s ⁻¹	N'	50-80/93	90-180/128	720-900/888
	N''	80-125/100	90-180/131	700-900/985

Adapted from Twomey, 1959

c=125, k=.33

c=160, k=.25

c=2000, k=.40

His work on this subject led to numerous modeling studies and theoretical investigations. (i.e. Lee et al., 1980; and Hudson and Clarke, 1992).

Hudson (1993) provides a summary of the evolution of CCN theory, including shift in focus, instrumentation and several theories presented over the years. In this paper, an equation for the critical supersaturation, S_c , was presented and is defined as:

$$S_c = \left(\frac{2.5 \times 10^5}{\text{number of soluble ions}} \right)^{0.5} \quad (2.2)$$

This calculation of S_c provided a simple means of including chemical properties in the effect of cloud droplet nucleation and size.

Pruppacher and Klett (1978) state that as a cloud droplet spectra evolves, it should theoretically become more narrow. Observations support this statement. Nevertheless, cloud droplet distributions are generally not as narrow as theory predicts (i.e. Fitzgerald, 1972). Cooper (1989) published a theoretical investigation of the effect of fluctuations in cloud-base updrafts that possibly explains this phenomena. He concluded that in unmixed regions of cumulus clouds, the widths of the droplet spectra can be determined by the spatial variability in the cloud-base updraft and a slope parameter that characterizes the CCN spectrum. He also concluded that in clouds with little to no net vertical motions, (i.e., horizontal segments of a wave cloud), the cloud droplet spectrum should broaden with variance in r^2 with increasing t^2 and in proportion to the variance in the relationship between the radius and the vertical velocity, where r is the radius of the cloud droplet and t is the time spent in cloud.

2.2b Modeling Studies

One of the first numerical studies of the growth by condensation of a population of cloud droplets was presented by Mordy (1959). He concluded that at the same aerosol

concentration, a doubling of updraft velocity seems to increase the number of growing particles by roughly a factor of three; i.e., at 50 cm s^{-1} updraft there were 1.4×10^8 growing droplets and at 100 cm s^{-1} there were 4.7×10^8 . Takeda and Kuba (1982) obtained similar results.

Using the equations presented by Twomey (1959), Fitzgerald (1972) developed a model and presented a comparative study of observations obtained in Minnesota and Florida. He looked at the effect of variations in the updraft velocity on the nucleated droplet spectra and found that an increase in the updraft results in a decrease in the standard deviation of the droplet spectra and thus also leads to a decrease in the dispersion coefficient. An increase in updraft velocity of 100% corresponded to a decrease in the dispersion coefficient of 15%, and an increase in number of cloud droplets.

Chuang and Penner (1990) used a well mixed spherical air parcel with coupled warm rain microphysics that is based on Edwards and Penner (1988). The aerosol distribution used for initializing the model was bimodal. Table 2.2 summarizes some of their findings. They theorize that a smaller latent heating term increases the supersaturation, leading to a higher nucleation fraction for the lower aerosol number

Table 2.2.
Summary of Percent of Nucleated Aerosol Fraction Data from Chuang and Penner (1990).

Aerosol Loading / Updraft Vel.	N droplet / N aerosol
100 cm^{-3}	
0.5 m s^{-1}	100 %
1.0 m s^{-1}	100 %
1000 cm^{-3}	
0.5 m s^{-1}	60 %
1.0 m s^{-1}	80 %

concentration. They also concluded that the shape of the initial aerosol size distribution only impacts the cloud drop spectra when updraft velocities are less than 1.0 m s^{-1} .

Jensen and Charlson (1984) conducted a modeling study of the activation process near cloud base using a one dimensional Lagrangian cloud model. Special attention was paid to the aerosol fraction nucleated at updraft velocities between 0.2 to 10 m s^{-1} . They found that the nucleated aerosol fraction is close to unity for the convective cases (5 to 10 m s^{-1}) and most stratiform cases (0.5 to 5 m s^{-1}) modeled except for the very low updraft velocities (0.2 to 0.5 m s^{-1}). The calculated nucleated aerosol fraction for 0.5 m s^{-1} , 1.0 m s^{-1} , and 2.0 m s^{-1} were approximately 0.95 , 0.97 , and 0.98 respectively. They also found that when aerosol loading was increased to continental concentrations (> 1000 particles cm^{-3}), a much smaller aerosol fraction was activated at weak updraft velocities, with the unactivated being smaller diameter particles.

2.2c Natural Cloud Studies

In the 1950's, several scientific efforts recognized that cloud droplet number concentration was strongly influenced by air mass origin. Squires (1956, 1958a, b) and Squires and Warner (1959) noted that transitions from marine air masses, aerosol concentrations between 10 and 100 cm^{-3} , to continental air masses, aerosol concentrations greater than 1000 cm^{-3} , corresponded to more than an order of magnitude increase in droplet concentrations. Since then, there have been numerous studies conducted with the intent to explore the microphysical differences that occur in clouds due to aerosol number loading.

Differences in drop number concentration may affect the precipitation processes, and thus the lifetime, of a cloud. Two clouds of similar size and liquid water content

have different concentrations of droplets: the cloud with a lower concentration of droplets will have a larger mean diameter droplet, and thus be more likely to produce precipitation (Rogers and Yau, 1989). Based on observations, Albrecht (1989) concluded that the lower the droplet concentration and the broader the cloud droplet spectra, the more likely the cloud would produce precipitation in its lifetime. Similar observations were made by Hegg et al. (1984). Due to wet removal of CCN and a decrease in water available in the cloudy volume, the formation of precipitation marks the latter stages of a cloud's lifetime and thus clouds that precipitate generally have a shorter lifetime than those that do not precipitate (Pruppacher and Klett, 1978).

Several studies have investigated the impact of industrial sources of CCN on cloud droplet concentrations (Hobbs et al., 1970; and Hindman et al., 1977a, b). Eagen et al. (1974) and Hobbs et al. (1980) summarized that paper mills can produce large numbers of both small CCN ($\sim .1\mu\text{m}$) and large hygroscopic CCN ($> 1.0\ \mu\text{m}$). Further evidence of industrial effects on clouds has been observed in satellite images of ship tracks. Aerosol emitted into marine stratus clouds by ship smokestacks have been thought to be the impetus of the phenomena known as ship tracks. Radke et al. (1988) presented what may be the first *in-situ* observations of ship tracks and King et al. (1993) added to the information available on ship tracks. Both works concluded that the hygroscopic particles acted to not only increase the cloud droplet number concentration, but also broaden the cloud droplet distribution. Both changes in cloud microphysics act to increase the optical depth of the affected cloudy region. Satellite imagery based on the visible part of the light spectrum indicates these areas of greater optical depth as a brighter image.

Cities have also been implicated in affecting cloud droplet distributions. Observations during the METROMEX project showed that higher cloud droplet

concentrations were associated with smaller mean droplet diameters (Braham, 1977). Alkezweeny et al. (1993) came to similar conclusions during a number of cloud physics investigations made within stratus clouds in areas near Denver and Kansas City.

A basic assumption of theory and numerical cloud modeling is that cloud droplets and hydrometeors are evenly distributed in space and far enough from each other to grow independently in a supersaturated environment (Roger and Yau, 1989). Borrmann et al. (1993) used a Holographic Droplet and Aerosol Recording (HODAR) system to investigate these hypotheses. They found that for measured absolute distances between droplets (using 10 μm as an average droplet size):

- 40 % of all droplets are closer to each other than 100 radii,
- 10 % of all droplets are closer to each other than 60 radii,
- 3 % of all droplets are closer to each other than 10 radii.

(Note: Pruppacher and Klett (1978) suggest that for the droplets to grow independently, the inter-droplet distances should be larger than 100 radii). These numbers were compiled for five case studies and do not completely represent "free atmospheric" conditions (aircraft may have disturbed the population). However, the results seem to imply that droplets in natural clouds may be close enough to interfere with each other while growing and evaporating (Borrmann et al., 1993).

2.2d Cloud Chamber Studies

Cloud chambers provide an excellent means to investigate the cloud microphysical theories. Several types of chambers exist: i.e., isothermal, dynamic, mixing and diffusion. Dynamic, or controlled slow expansion, cloud chambers can be used to study how a cloud forms in a simulated adiabatically rising parcel of air. White

et al. (1987) detail the University of Missouri cloud simulation facility that consists of two small scale dynamic-type chambers. These chambers have been instrumental in investigations of CCN activation and uptake of water by hygroscopic particles (Alofs et al., 1989 and Hagen et al., 1989). However, the sensitive time scale is limited by the relatively small size of the devices. Also, droplet spectra are not measured directly. The clouds formed are assumed to be monodisperse.

DeMott (1990) and DeMott et al. (1990) describe the dynamic cloud chamber housed at the Colorado State University Cloud Simulation Laboratory (a full description can also be found in Appendix A). This chamber is instrumented with a cloud droplet spectrometer and its large size permits longer experiments with minimum wall effects. DeMott et al. (1983), DeMott and Rogers (1990), DeMott (1990), Rogers and DeMott (1990) have performed several intensive ice nucleation studies in the dynamic cloud chamber.

Hindman (1989) used the CSU dynamic cloud chamber to study the droplet formation and evaporation processes of warm clouds at 0.6 m s^{-1} updraft velocities. Aerosol assumed to be polydisperse was injected into the chamber and counted using a CNC (Environment / One). Optical particle counters were used to measure the haze and cloud droplets from different heights in the chamber and included: a Forward Scattering Spectrometer Probe (FSSP-100; Particle Measuring Systems, PMS, Boulder Co.), an Active Scattering Aerosol Spectrometer Probe (ASASP, PMS), and a Royco model 200. These measurements were used to look at both the cloud droplet distribution with height and the vertical profile of liquid water content (LWC). Comparison of these measurements to field observations, as well as a plot of pressure, temperature and dewpoint on an adiabatic chart, supported his conclusion that the chamber was capable of simulating marine stratus characteristics. Observations in the chamber were compared to

a simple cloud model output. At 0.6 m s^{-1} , he observed significantly lower concentrations of smaller droplets than were predicted by the model. He attributed this reduction to partial evaporation and wall losses in the sample tube. He concluded that cloud chamber observations of LWC, number concentrations, mean diameter, and dispersion coefficient were within 10 to 60 % of the values computed by the model.

Most experiments in the CSU dynamic cloud chamber have been conducted at simulated updraft velocities above 2.5 m s^{-1} . There is a large void between the updraft velocity used by Hindman (1989) in his investigation (0.6 m s^{-1}) and the "usual" updraft velocity (2.5 m s^{-1}). An investigation at several updraft velocities between these two velocities is needed. Also, better characterization of the aerosol before activation, and of the chamber processes that form the cloud and the aerosol, would be useful for further marine stratus investigations. This thesis has been designed to tackle these issues.

CHAPTER 3
**MARINE AEROSOL MEASUREMENT - PROJECT DESCRIPTION AND
RESULTS**

3.1 Purpose

Primary goals of the ASTEX/MAGE cooperative research project were to study the circumstances surrounding the transition from marine stratus clouds to trade-wind cumulus clouds and to study the marine sulfur cycle in the northeast Atlantic. A secondary objective of ASTEX/MAGE was to complete the first ever Lagrangian study of an air mass. In support of this thesis, specific goals for the CSU portion of the project were:

- 1) to obtain a working knowledge of the DMPS system;
- 2) to obtain field measurement experience;
- 3) to support aerosol characterization efforts on the *Malcolm Baldrige* by sampling the submicron aerosol spectra;
- 4) to measure characteristic marine boundary layer temperatures, relative humidities, and submicron aerosol spectra, for use in simulating marine stratus conditions in the cloud chamber part of this study.

All of these specific objectives were attained in the process of preparing for, taking part in, and processing the data from ASTEX/MAGE. The details of this portion of the study are described below.

3.2 Experimental Design

3.2a General Approach

Direct measurements of marine boundary layer submicron aerosol (0.012 to 0.54 μm in diameter) size distributions were made aboard the NOAA ship *Malcolm Baldrige* in June, 1992. Measurements were taken in the area surrounding 32° N latitude and 25° W longitude in support of the ASTEX/MAGE field experiment. Figure 3.1 depicts the track of the *Malcolm Baldrige* during the field project. Other platforms involved in the

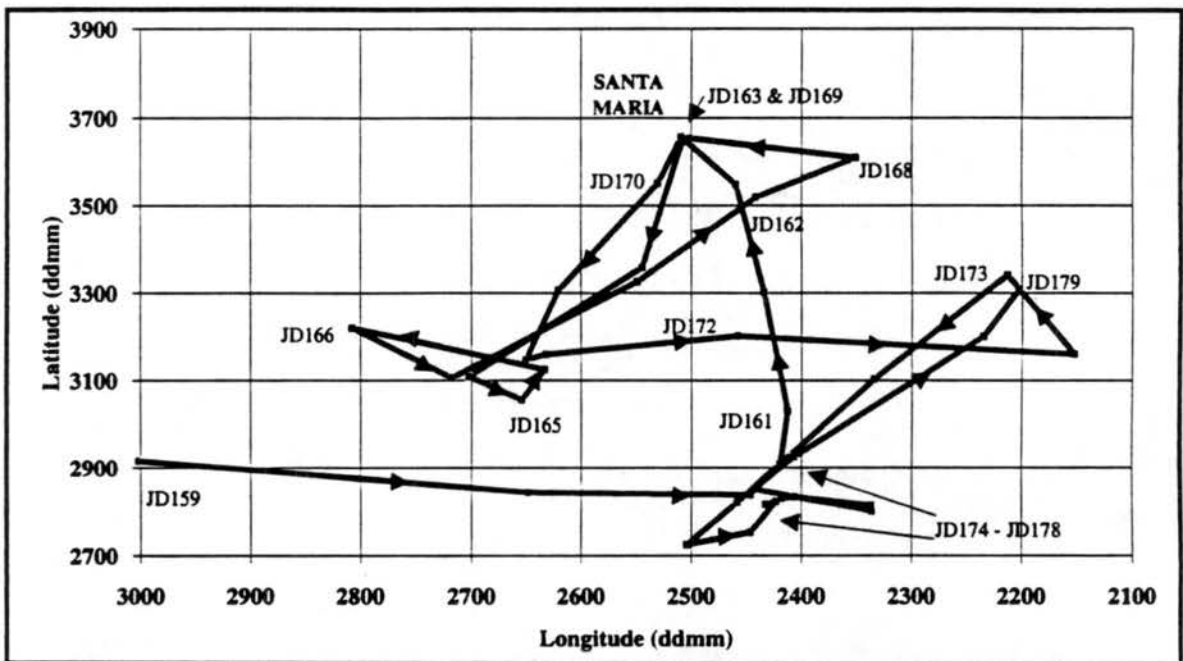


Figure 3.1 *Malcolm Baldrige* Ship Track from June 1 to June 27, 1992. JD means Julian Day.

MAGE portion of the field experiment were an island site on Santa Maria, Azores, and the NOAA ship *Oceanus*.

There were four 40-hour periods of intensive sampling in which all instruments on the ship were operational. The rest of the time, sampling of submicron aerosol was conducted as often as the meteorological conditions permitted. Operations were generally stopped when it was raining too hard, when the ship was steaming with the wind, which could have caused contamination of samples by smokestack gases, or when the ship was in port. Although measurements were not taken continuously, they were taken during every phase of the diurnal cycle. Approximately 240 distributions, representing one-hour scans, were measured. Table 3.1 generalizes the dates, times and general air mass type of measurements taken during ASTEX/MAGE. There were two intensive sampling periods when the entire compliment of MAGE participants were sampling. These are labeled Lagrangian # 1 and Lagrangian #2. There were two other intensive sampling periods that were participated in by the *Malcolm Baldrige* instruments only. These are labeled Intensive #1 (which was a practice for the Lagrangian experiments) and Intensive #4.

An air mass, with a trajectory such that it would transect the experiment area, was identified for the Lagrangian experiments using satellite imagery and meteorological charts. The trajectory was then forecasted. The *Oceanus* was directed to intercept the air mass and release constant altitude balloons and tracer gases, such as SF₆ in the air mass and then travel with the air mass while continuously sampling from it. The island site was a sampling site as well as base for the aircraft operations that took place in the air mass. The *Malcolm Baldrige* was directed to sample continuously from the release of the balloons and to intercept the air mass at the ending point of the experiment.

Table 3.1.
Summary of ASTEX/MAGE Submicron Aerosol Measurements

	Times of Collection (Julian Decimal Time)	General Air Mass Type	Average Particle Conc. (cm ⁻³)	Comments
	JD154.5548 to JD155.8044	clean marine	200	distributions consistently bimodal
Intensive #1	JD156.4586 to JD157.991 (continuous)	clean marine	300	distributions consistently bimodal
	JD159.4128 to JD164.0996	clean marine	225	distributions consistently bimodal
Lagrangian #1	JD164.1426 to JD166.3485 (continuous)	clean marine	180	distributions consistently bimodal
	JD167.5827 to JD167.7991	modified marine	225	distributions appeared to be transitional between bimodal and monomodal
Platform Intercomparison	JD168.6872 to JD168.7935 (continuous)	clean marine	150	distributions were bimodal
Lagrangian #2	JD170.8498 to JD172.5679 (continuous)	modified marine	500 (for bimodal distrib.)	primarily bimodal distributions until JD172.3436; then became monomodal with peak concentration of 1400 particle cm ⁻³ .
	JD174.4375 to JD175.5241	polluted marine	650	distributions consistently monomodal
Intensive #4	JD176.3622 to JD177.782 (continuous)	modified marine	800	distributions were primarily bimodal with monomodal distributions measured between JD177.3233 and JD177.413

A continual record of standard meteorological data (temperature, dewpoint temperature, wind speed and direction, and pressure) as well as ship position has been provided by NOAA/AOML (Miami) for the *Malcolm Baldrige* cruise. Other data sets available from the *Malcolm Baldrige* included aerosol number concentrations and distributions for particles greater than 0.5 μm , measurements of specific chemical species, such as SO₂, DMS, and ozone, and ocean and aerosol chemistry. There were also cloud microphysical measurements taken by aircraft during the Lagrangian experiments.

3.2b Instrumentation

A schematic of the shipboard measurement system is shown in Figures 3.2-3.3. The marine aerosol was drawn at a flowrate of approximately 25 lpm through approximately 50 feet of large diameter tubing (0.75 inch outer diameter, OD) that extended from 1.5 feet in front of the instrument tower to the sample van where the DMPS system resided. The inlet of the main sample tubing was made from 3 feet of 0.5 inch O.D. tubing bent so that it is faced perpendicular to the ship's main deck. A rain-shield, made of a 2 liter Nalgene plastic bottle, was attached to the tubing using a drilled bulkhead union secured in the cap of the bottle (see Figure 3.4). Gravitational and diffusional losses in the tubing were generally very small due to the size of the tube and the flow through the tube. A discussion of these losses is contained in section 3.3d.

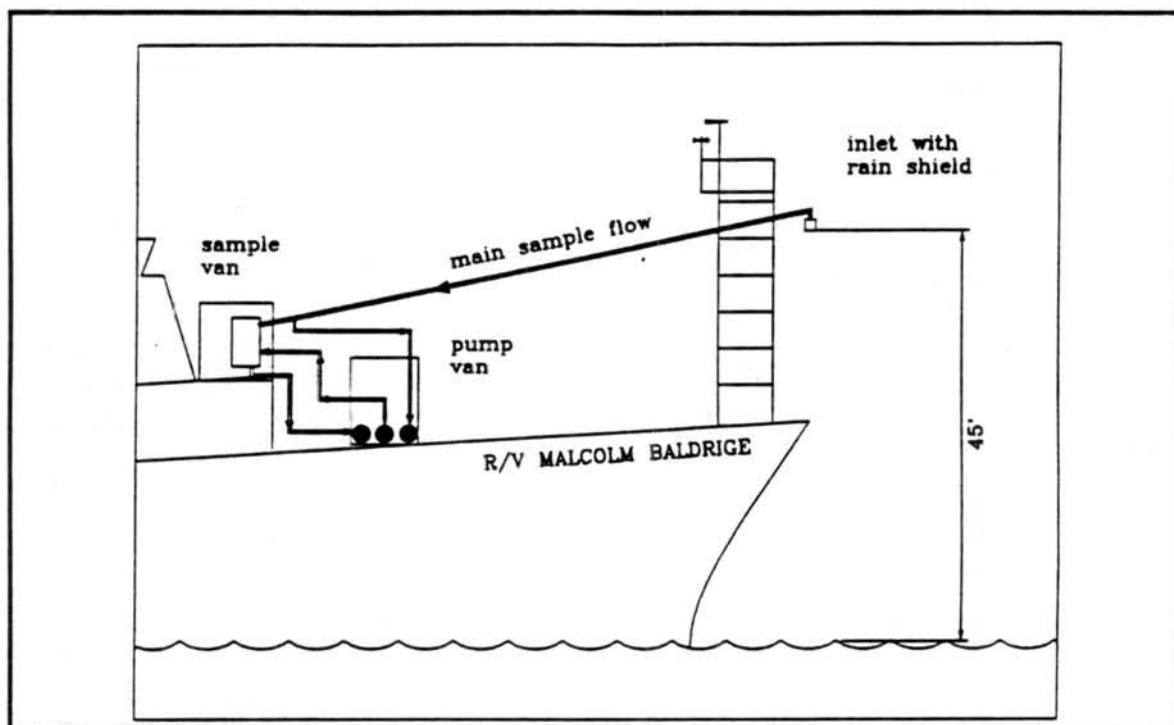


Figure 3.2 Schematic of Instrument Placement on *Malcolm Baldrige*.

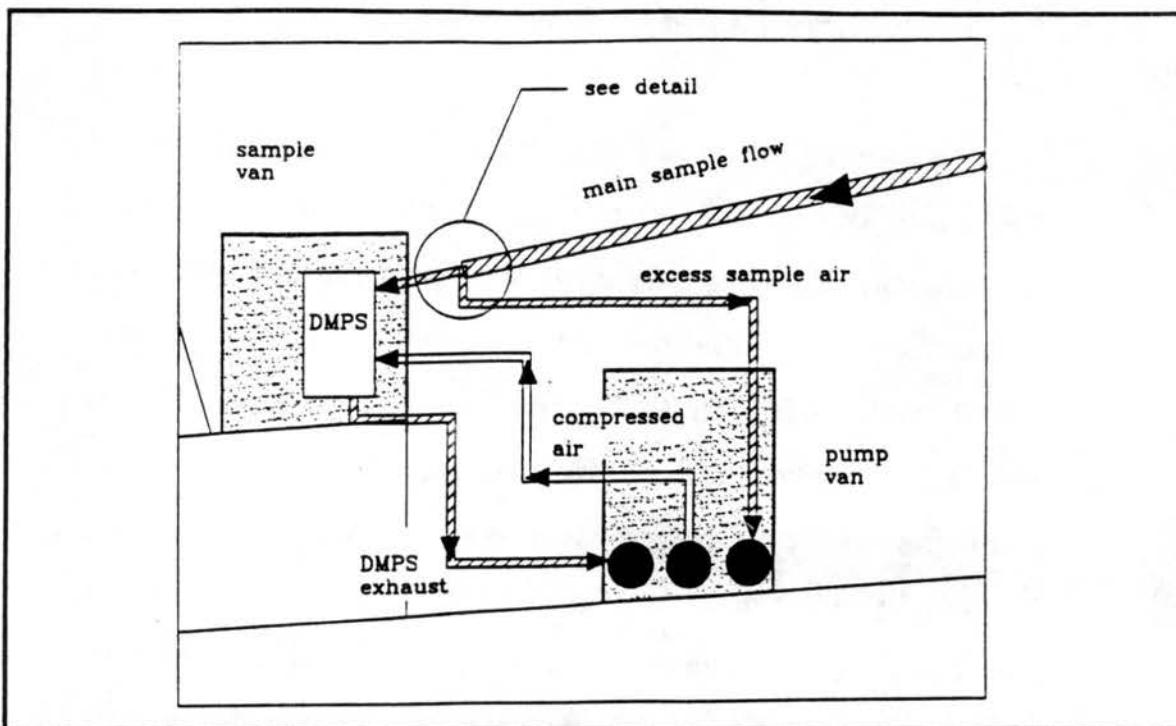


Figure 3.3 A More Detailed Look at the Instrument Set-up on the Deck of the *Malcolm Baldrige*

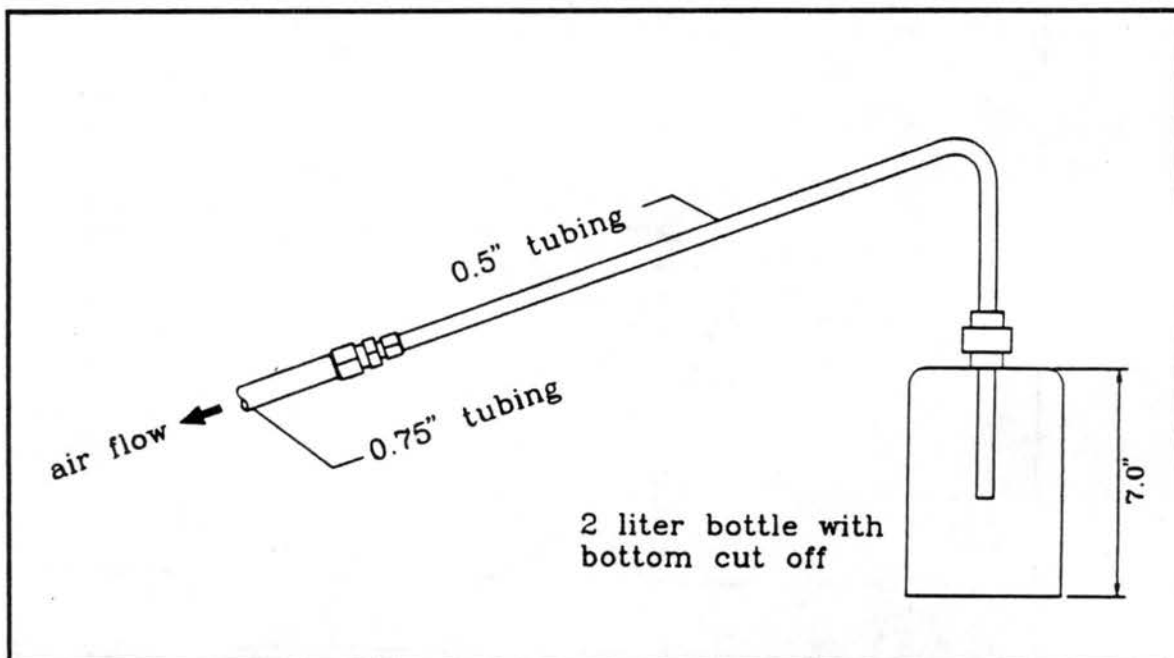


Figure 3.4 Depiction of Rainshield Used as the Main Sample Inlet.

Immediately ahead of the sample van, a small probe was inserted into a tee to allow a small sample (0.5 lpm) to be drawn from the larger flow (Figure 3.5). The excess air was drawn through a rotameter, where the total sample flow was measured, to the main sample pump housed in the pump van. The small sample pulled from the main flow was drawn through the DMPS system by a separate pump.

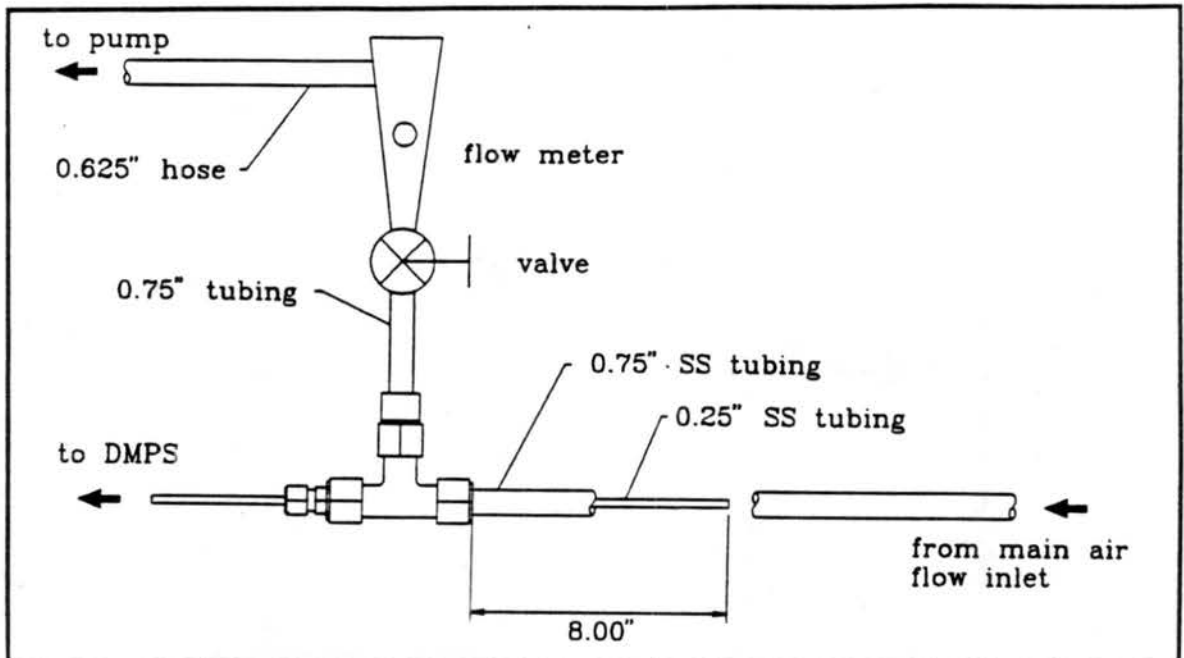


Figure 3.5 Schematic of DMPS Sample Inlet Design.

The particle measuring system used to measure the submicron aerosol consisted of a TSI DMA, a TSI Model 3022 CNC, and an IBM-compatible 386/25 MHz computer with the TSI DMPS software installed. The entire system is referred to as the DMPS system. Detailed schematics of the DMA, CNC and DMPS system used on the ship are shown in Figure 3.6-3.8. The Polydisperse Aerosol inlet on the DMA was connected to the small sample probe inserted into the main sample line. The aerosol passed through a 16 inch piece of plastic tubing before being dried by passing through a twelve inch

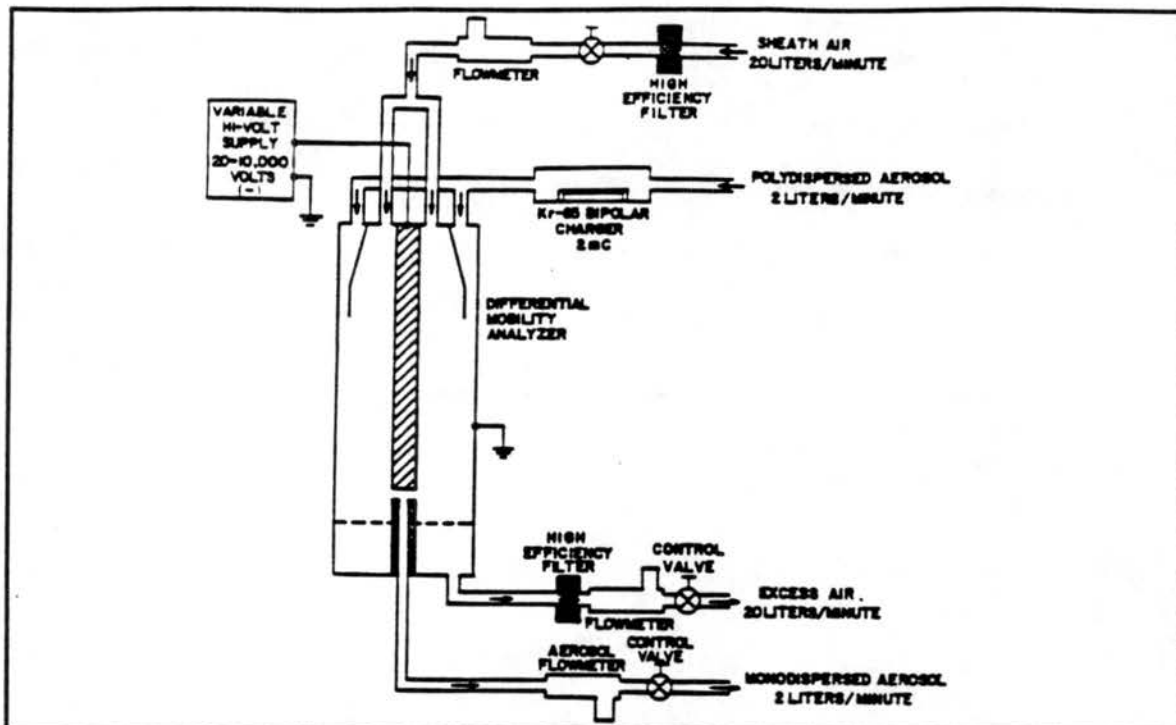


Figure 3.6 Schematic of the TSI Model 3071 Electrostatic Classifier (TSI, 1983)

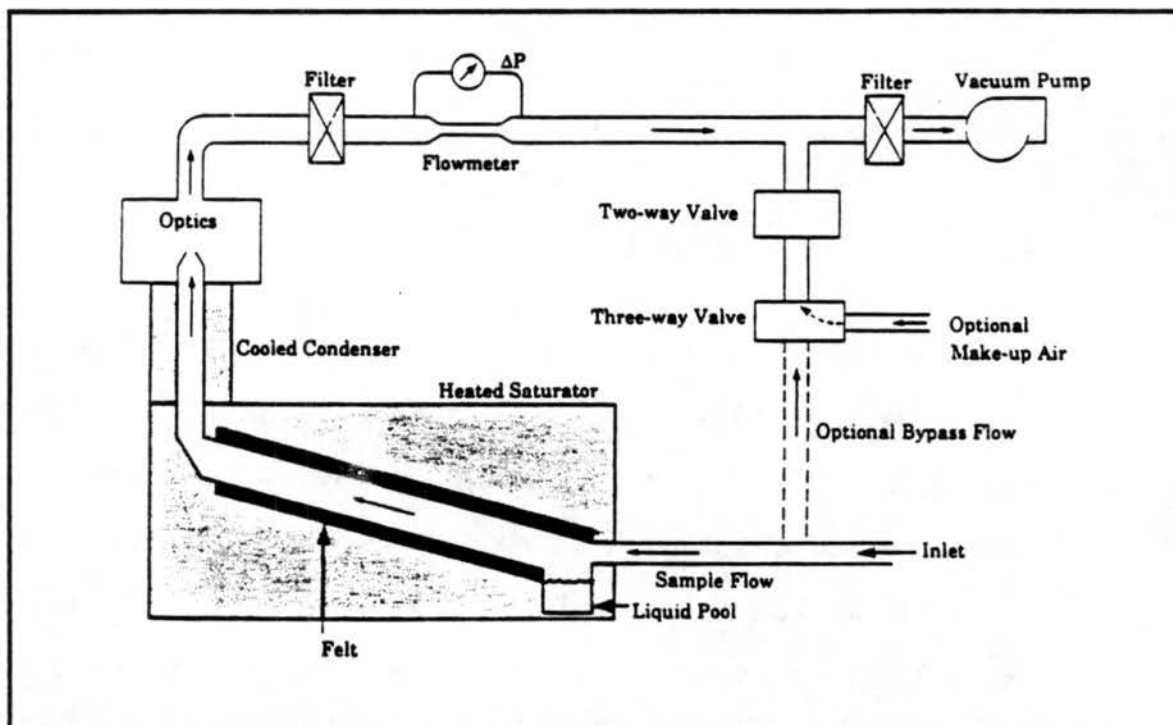


Figure 3.7 Schematic for the TSI Model 3022 CNC (TSI, 1988)

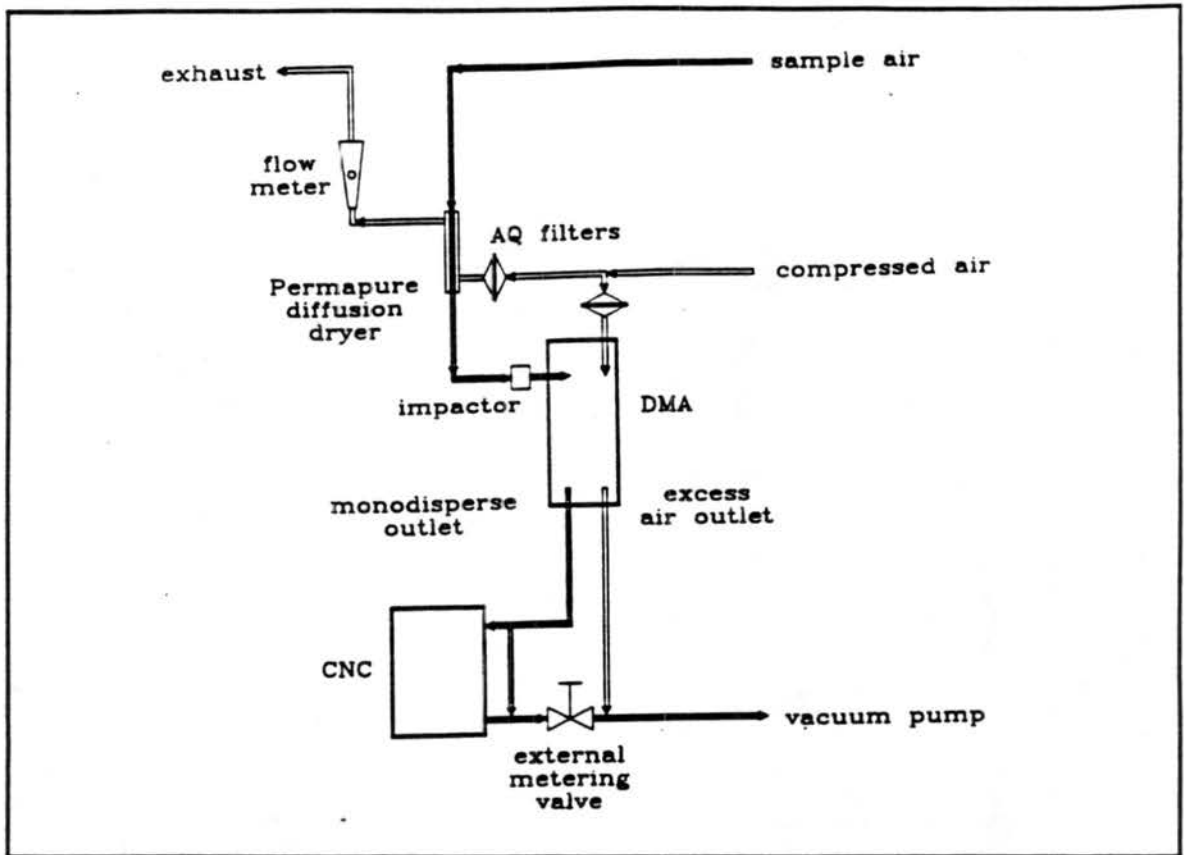


Figure 3.8 Schematic of the DMPS System Configuration Used on the *Malcolm Baldrige*.

Permapure diffusion dryer immediately upstream of an impactor with a 50 % cutpoint of $0.497 \mu\text{m}$. The stream exiting the impactor entered the DMA through the Polydisperse Aerosol inlet. The Sheath Air inlet was connected to a dry compressed air system to guarantee measurement of dry aerosol (see Figure 3.9). The flow exiting the DMA was larger than what the CNC would accept, so a tubing system connecting the Monodisperse Aerosol outlet, Excess Air outlet and the CNC inlet was designed that combined principles of operating in both overpressure and underpressure modes. The whole DMPS system, in the sample van, was connected to a different pump than the main sample line pump, in the pump van, via a fifty foot outdoor hose (see Figure 3.3).

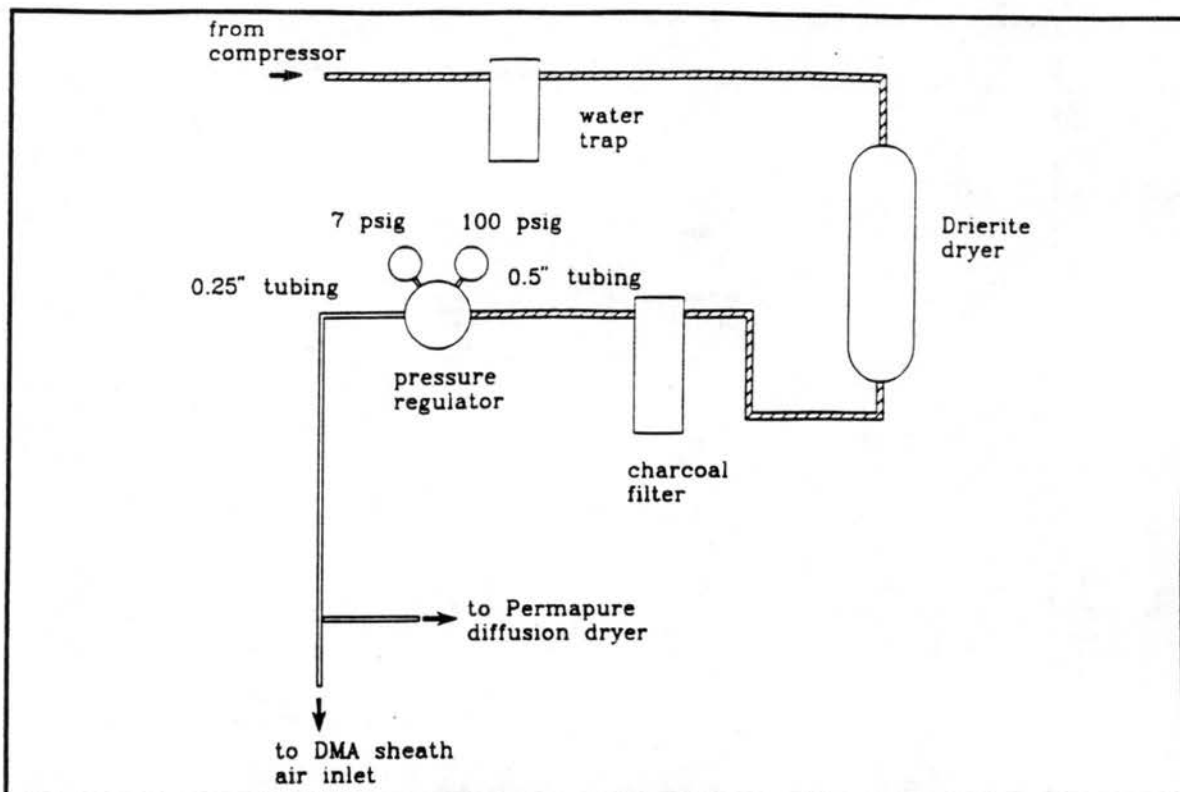


Figure 3.9 Schematic of the Compressed Air Filtering System Used on the *Malcolm Baldrige*.

3.2c Procedure

The experimental technique used to collect data during ASTEX/MAGE was finalized while the ship was steaming across the Atlantic Ocean to get into position for the field project. It was determined experimentally that distribution measurements would be taken with the time averaging of 30 seconds in every possible channel of the DMPS system. The counting statistics involved in this decision are discussed in section 3.3b.

Start-up procedure began by warming up the CNC and DMA for approximately thirty minutes. When ready, the main sample flow pump, the DMPS pump and then the air compressor, all located in the pump van, were started. The compressor was regulated

at approximately 100 psi. In the instrumentation van, the compressed air line was opened and regulated at 7 psi.

As is pointed out in Appendix E, proper aerosol measurement by the DMPS system required careful balancing of instrument flows. After adjusting the pressure of the compressed air line, the four DMA flows were matched in the following manner. The Sheath Air valve on the DMA and the external metering valve were cracked open almost simultaneously. Flow through these two valves was slowly increased while trying to maintain the proper pressure drop across the impactor on the Polydisperse inlet. When the excess air flow voltage reached its expected value, the two valves being opened were left in their position and the Monodisperse air valve was opened until the voltage for that flowmeter reached the required value. The sheath air voltage was then checked and its valve adjusted accordingly, then the excess air voltage was checked and the external metering valve was adjusted. The nudging of flows was continued until all three metered flows were in balance and the proper pressure drop occurred over the impactor. The DMA External Air valve remained open throughout the procedure. The system was now ready to take measurements.

Shutdown procedure was to shut the Monodisperse valve, shut external metering valve, shut sheath air valve and close compressed air line in the instrument van. The pumps and compressor were then turned off, and the compressor drained of any condensed water.

One aerosol size distribution measurement required one hour to complete during this field project. During the four intensive sampling periods, the measurements were synchronized with filter pack measurements being made by another research group. Otherwise, measurements were taken whenever prevailing weather conditions and ship direction allowed.

3.3 Instrument Limitations and Data Correction

3.3a Diameter Range Limitation

There is a finite diameter range that can be measured using the DMPS system. Limitations of this range are dependent on the sheath air and the polydisperse air flow rates (as detailed in Appendix C). Table 3.2 depicts the diameter ranges available based on flow. Measurements taken during the ASTEX/MAGE field project were made using the 5.0 lpm/0.5 lpm sheath/polydisperse flow combination. Therefore, the diameter range available for these measurements was 0.012 μm to 0.535 μm .

Table 3.2.
DMPS Operating Range vs. Flowrate

Sheath/Polydisperse Flow Rates (lpm)	Minimum Diameter (μm)	Maximum Diameter (μm)
3.0 / 0.3	0.017	0.886
5.0 / 0.5	0.012	0.535
7.0 / 0.7	0.011	0.391
10.0 / 1.0	0.010	0.337

(Adapted from TSI Model 3932 DMPS Instruction Manual, 1992)

3.3b Counting Statistics

At concentrations below 1000 particle cm^{-3} , each particle moving through the CNC is counted separately and the concentration is computed from the frequency of pulses. Most measurements made during the field project did not exceed 1000 particles

cm⁻³. In this mode, there is error due to particle coincidence. The DMPS program automatically corrects for this error. However, the DMPS software does not account for accuracy of the concentration reading being limited by statistical error at the lower end of the count mode. As the total number of particles decreases, the uncertainty in the average count rate increases. The statistical error of count, σ , is related to the total particle count, n , through equation 3.1.

$$\sigma = n^{0.5} \quad (3.1)$$

and the fractional uncertainty is

$$\sigma/n = 1/n^{0.5} = 1/(NQt)^{0.5} \quad (3.2)$$

where N is the measured particle concentration, Q is the CNC flow rate (5 cm³ s⁻¹), and t is the averaging time used by the DMPS system. The averaging time is set by the operator of the system. From (3.2), it can be seen that as the averaging time is increased, the fractional uncertainty is diminished. For the ASTEX/MAGE field project, the averaging time used was 30 seconds. Table 3.3 summarizes the fractional uncertainty of the aerosol size distribution measurements taken.

Based on observations, it can be concluded that most of our uncertainty in measurements due to counting statistics of the CNC were less than 2 %. However, in diameter bins containing less than 1 particle cm⁻³, an additional fractional uncertainty of 8 % may be added. This uncertainty applies to each bin and was used in addition to total measurement uncertainty, which ranged from 15 to 90 % (depending on diameter size) to determine the uncertainty of the DMPS measurements.

Table 3.3.

Fractional Uncertainty Associate with Counting Statistics. Calculated from (3.2) with $Q = 5.0 \text{ cm}^3 \text{ s}^{-1}$ and $t = 30$ seconds.

Measured Concentration (particles cm^{-3})	Fractional Uncertainty
1	0.08
10	0.02
100	0.008
1000	0.002

3.3c Aerosol Dryness

The dryness of the aerosol measured onboard the ship was not determined in the field. Two parameters affecting this measurement were the Permapure Diffusion Dryer efficiency and the sheath air dryness. To find out the efficiency of the Permapure dryer, an experiment involving the CSU dynamic cloud chamber (see Appendix A) was set up. The cloud chamber was filled with water vapor until the relative humidity in the chamber was very close to 100% at approximately 25 °C. These values represent approximated maximas measured during the cruise. Temperature on the cruise was generally 3 to 5 °C cooler, and relative humidity at those temperatures was generally between 65 and 85 %. A dewpoint hygrometer was used to measure the dewpoint of the air that was pulled from the chamber through the dryer. It was found that the dryer was capable of drying air that was initially nearly saturated to a relative humidity of approximately 11%. Aerosol at relative humidities of less than 30% is considered dry. The dewpoint hygrometer was also used to measure the dewpoint of the air coming out of the compressed air system used on the ship for the sheath air of both the DMA and the Permapure dryer. The compressed air was found to be dried to less than 2% relative humidity. Based on these

test results, it can be said that the aerosol measurements made on the ship were dry and no RH corrections to the diameter measurements were required.

3.3d Tubing Losses

Reynolds number calculations were performed first and it was determined that flows in the sampling system were laminar. Gravitational and diffusional losses in all sizes of tubing used were calculated using the method provided by Dennis (1976). The results, tabulated in Table 3.4, show that the only significant loss was diffusional losses of particles less than 0.02 μm .

The possibility that the short length of plastic tubing and Permapure dryer had caused excessive losses of particles was then investigated. Plastic tubing can become charged, which may result in aerosol losses that cannot be determined by simple calculations. These electrostatic charging aerosol losses were determined experimentally. The CSU cloud chamber was used as a source of homogeneous aerosol for this investigation. A 25 inch length of stainless steel tubing, which is approximately the same length of the plastic tubing/Permapure dryer (16 inch section of plastic tubing and the Permapure dryer) set up was used in the comparison. Dry aerosol was drawn from the chamber through the stainless steel tubing and entered the DMPS system directly through the impactor. The tubing was then changed to the plastic tubing/Permapure dryer configuration and aerosol was drawn through the DMPS system. Measurements taken through each tubing configuration were repeated several times and recorded. The stainless steel tubing measurements were considered to be the "true" distributions from which differences were figured. There appeared to be an average loss of 11% in particle number in the plastic tubing/Permapure dryer set-up. However, Table 3.4 shows that the

losses were not consistent throughout the size range of the instrument. There were significant losses of the smallest and largest particles. The corrections in Table 3.4 were applied to the data taken during ASTEX/MAGE. On average, a 12% increase in concentration was noted.

Table 3.4
Calculated Penetration of Particles Through Tubing

Tubing Size/ Type of Loss	0.01 μm	0.02 μm	0.04 μm	0.14 μm	0.45 μm
1/2" Grav.	1	1	1	1	1
1/2" Diff.	0.99	0.993	0.9963	0.999	1
3/4" Grav.	0.9998	0.9997	0.9995	0.9975	0.99
3/4" Diff.	0.95	0.975	0.986	0.997	0.999
1/4" Grav.	1	1	1	1	1
1/4" Diff.	0.92	0.95	0.9785	0.997	0.999
Plastic/Perma*	0.80	0.80	0.82	0.93	0.76
uncertainty ⁺	0.95	0.96	0.18	0.27	0.35

Grav. - Gravitational losses

Diff. - Diffusional losses

* Penetration through plastic tubing/Permapure dryer combination calculated based on laboratory results

+ Uncertainty calculated as described below

Uncertainties were calculated for the DMPS measurements using the measurements taken through the stainless steel tubing described in the paragraph above. The aerosol in the cloud chamber was considered to be homogeneous and the "average" distribution was computed for the six measurements. Deviations about the average distribution were used to determine the uncertainty of the DMPS measurements. Fluctuations in CNC flow were determined to be insignificant additions to the uncertainty calculations. Counting statistics uncertainties of the CNC were added to those bins that frequently have measurements less than 1.0 particle cm^{-3} . Calculations

(Table 3.5) showed that the greatest uncertainty in DMPS measurements to be in the measurements below 0.02 μm , which can be anywhere from 80 to 98 % (by channel). Figure 3.10 shows a representative uncorrected and corrected aerosol distribution with uncertainties plotted.

Table 3.5.
Uncertainty of number measurement differentiated by diameter bin and diameter bin width.

Diameter (μm)	Width (μm)	Uncertainty (%)	Diameter (μm)	Width (μm)	Uncertainty (%)
0.014	0.0021	95	0.093	0.013	20
0.017	0.0023	98	0.108	0.015	20
0.019	0.0027	96	0.124	0.017	26
0.022	0.0032	92	0.143	0.021	27
0.026	0.0037	73	0.166	0.023	31
0.029	0.0042	62	0.191	0.027	34
0.034	0.0049	48	0.220	0.032	34
0.039	0.0057	28	0.255	0.036	34
0.045	0.0066	18	0.294	0.042	32
0.052	0.0075	20	0.340	0.049	35
0.060	0.0087	27	0.392	0.056	35
0.070	0.010	23	0.453	0.065	35
0.081	0.012	20	0.523	0.075	30

3.4 Results

In general, the DMPS system deployed on the Malcolm Baldrige operated in a consistent manner. Once set up, the plumbing of the system proved to be acceptable. There was very little maintenance required to keep the system running, which allowed for measurements to be taken consistently throughout the entire cruise. Information obtained from the measurements include size, surface area, and volume distributions.

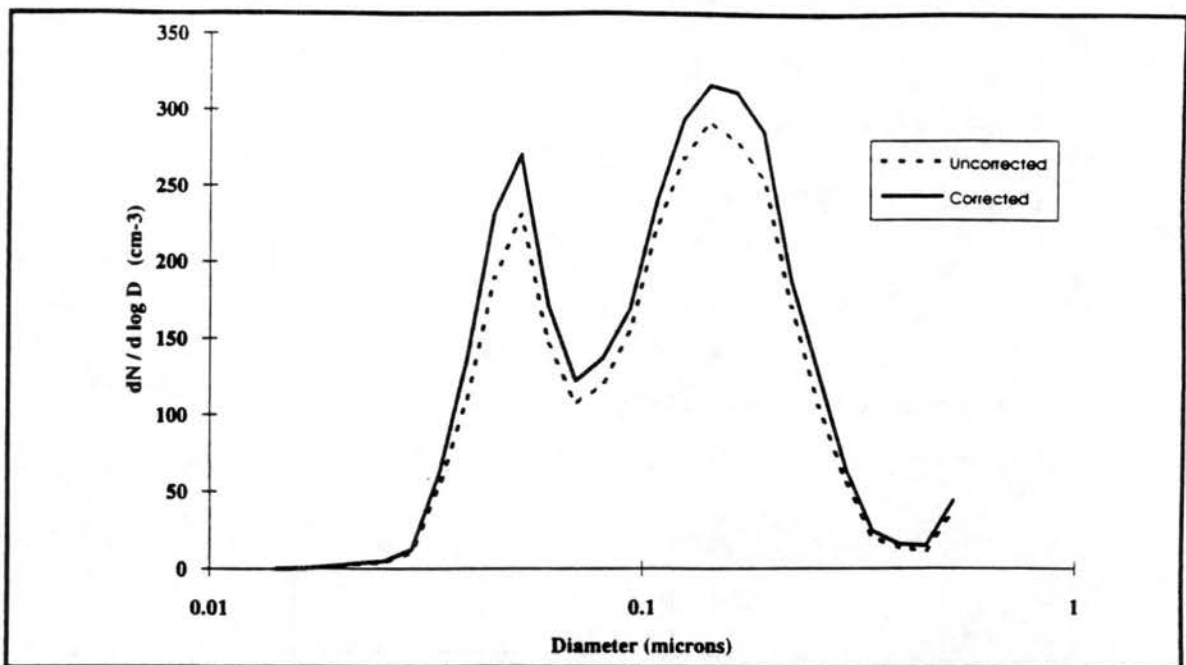


Figure 3.10 Comparison of Uncorrected Data (dashed line) to Corrected Data (solid line) for JD165.4503 (1050 UTC).

Changes in size distributions indicated areas of transition from polluted to clean air masses (or vice versa), and mesoscale variability of air mass. A discussion of these observations is provided in section 3.4c.

3.4a Behavior of System

Only one plumbing change was needed during the trans-Atlantic part of the cruise. A flowmeter, originally placed directly upstream of the main sample pump, experienced too much vacuum and became unreadable when the pump was activated. The problem was remedied by moving the flowmeter to come almost directly after the sample flow tee (see Figure 3.5). During the 40 hour intensive sampling periods, the vacuum pumps were monitored for signs of overheating. None were detected. There were no other maintenance problems that impeded the collection of data.

Comparison of DMPS accumulation mode distribution measurements to data taken by the NOAA/ARL/ERL Active Scattering Aerosol Spectrometer Probe (ASASP) instrument (0.12 to 3.1 μm in diameter) showed that the distribution shapes measured by the two instruments compared well (see Figure 3.11). The ASASP inlet was located approximately 10 feet above the DMPS main sample line inlet.

Differences of 20 to 40 % of number concentration in the overlap region of the two instruments indicated that some data correction was needed. Loss of particles in the extensive tubing system used for the measurements were investigated explain 11 to 12 % of the difference. Uncertainty in measurements could clarify most of the remaining discrepancy in the different aerosol measurements. Table 3.5 showed the percent uncertainty per bin size of the data, including statistical counting uncertainty.

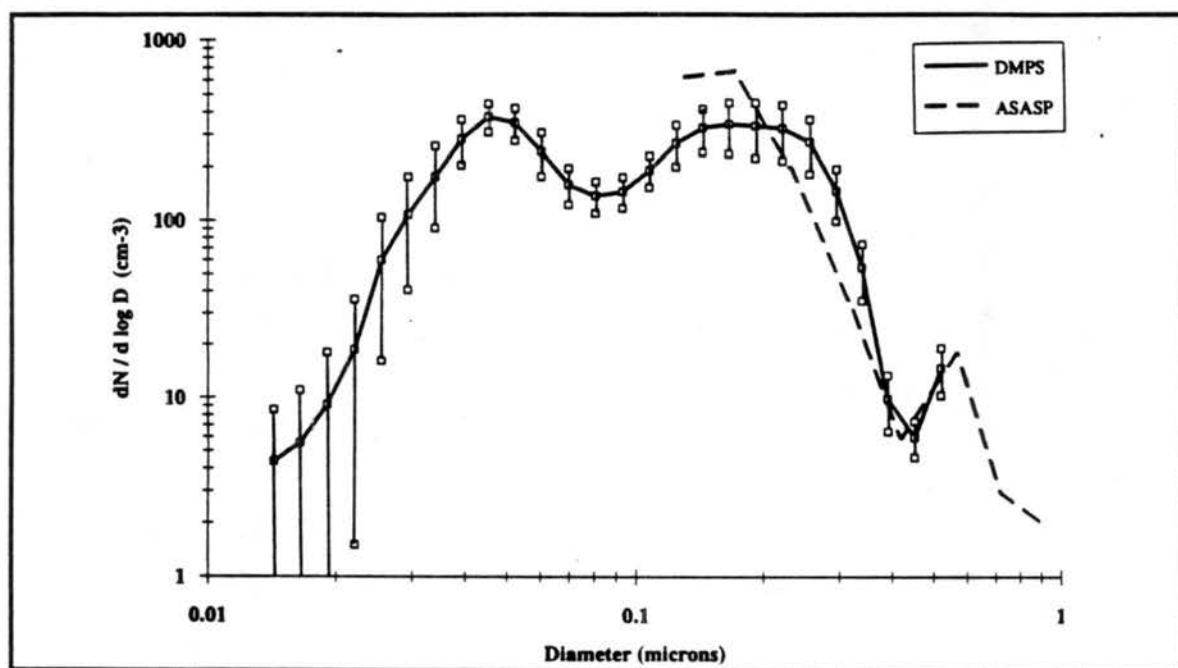


Figure 3.11 Comparison of averaged DMPS measurements (solid line) to NOAA/ARL/ERL ASASP (dashed line) measurements taken between JD164.8558 and JD165.0413. [data courtesy of H. Sievering and Y. Kim].

A portion of the overlap region between the DMPS system and the ASASP instrument was affected by these large uncertainties. There were also uncertainties associated with the calibration and measurement techniques used for the ASASP. These values had not yet been provided by the investigator in charge of this information.

Trends in total submicron aerosol number concentrations measured by the DMPS agreed with total CN concentrations measured by NOAA/AOML CNC (TSI model 3010). Figure 3.12 shows that the concentration measurements made by the CNC to be significantly higher than those measured by the DMPS. This is because the CNC also measures particles with diameters greater than $0.54 \mu\text{m}$. This information will be used in future analysis to determine the percent of aerosol in the submicron modes.

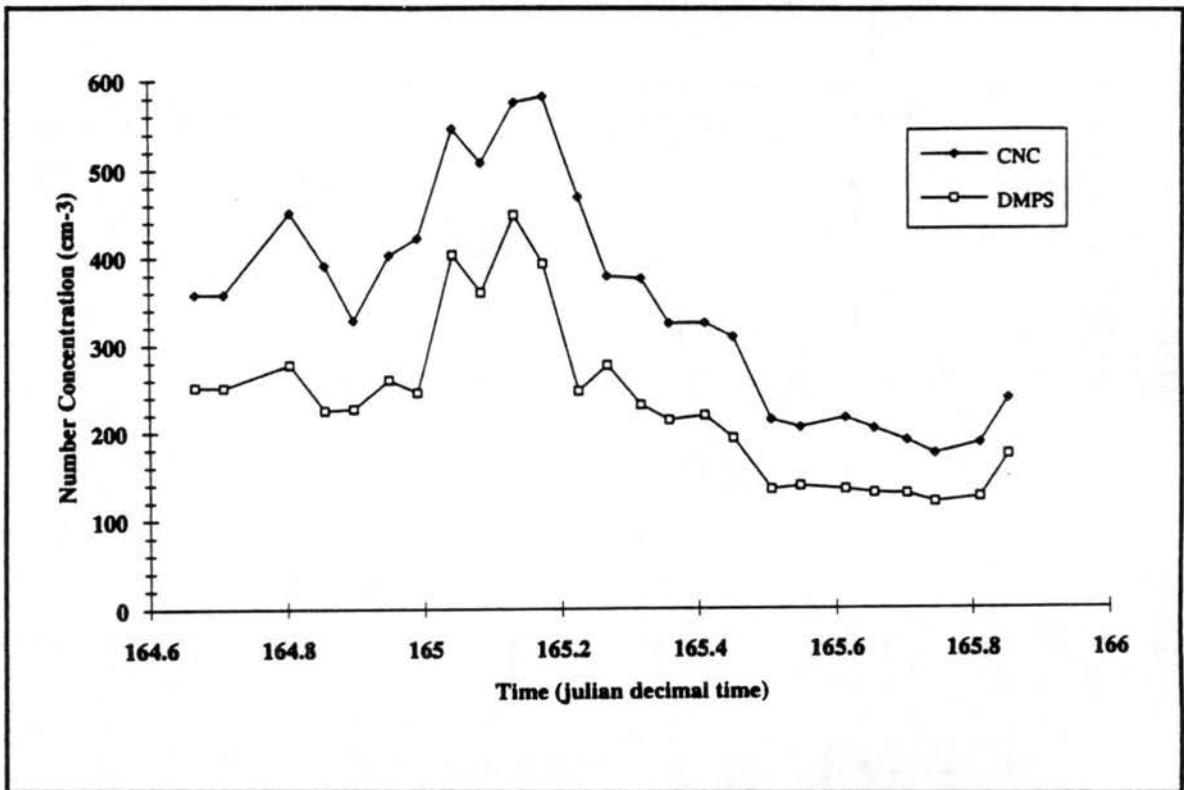


Figure 3.12 Comparison of CSU DMPS derived total number concentration (open symbols) to total aerosol concentrations from NOAA/AOML (closed symbols) [data courtesy of A. Pzsenney].

3.4b Data

Mobility distributions can be depicted in several ways by the DMPS software, including: number distributions, surface area information and volume distributions. Surface area and volume distributions were calculated by the DMPS software from the number concentration and diameter information. The analysis done, to date, used the number distribution information only. Figure 3.13 depicts the number concentration, surface area, and volume distribution for JD165.4503 (1050 UTC) respectively. As expected, the nucleation mode, even though relatively high in concentration, does not contribute much to either the surface area distribution or the volume distribution.

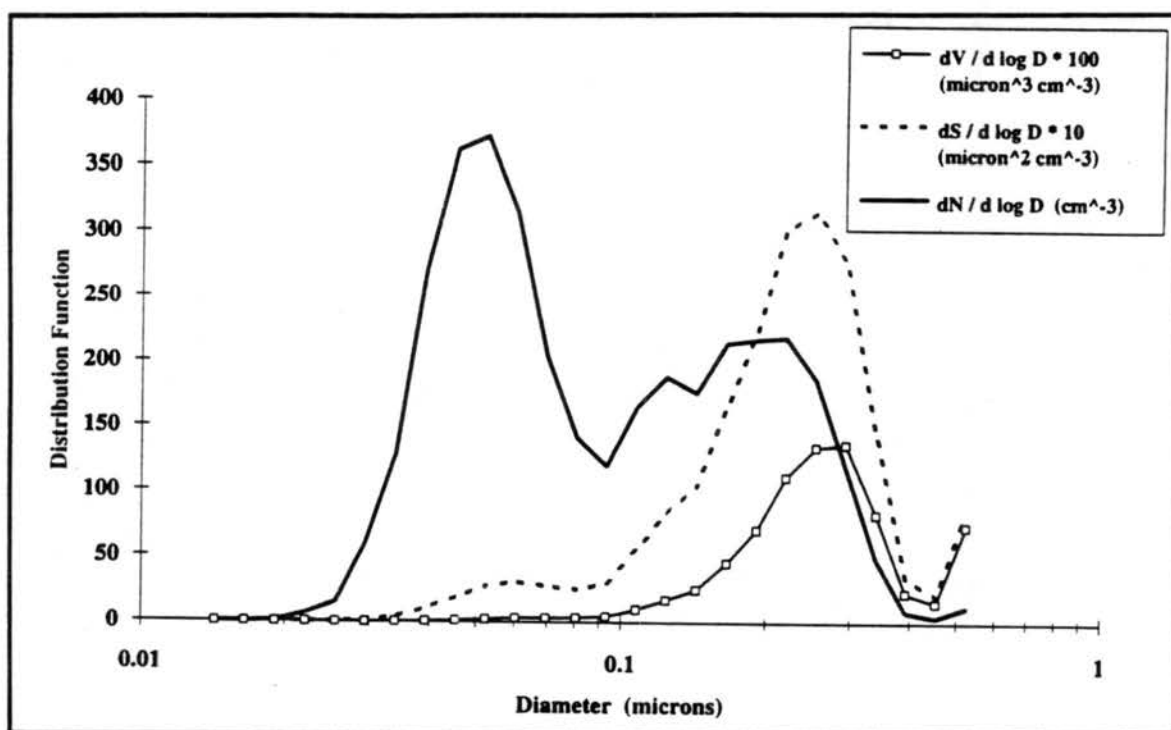


Figure 3.13 Example of a Number Distribution (solid line), Surface Area Distribution (dashed line), and Volume Distribution (solid line with open squares) calculated from mobility size distribution by DMPS system for JD165.4503

Information about the type of aerosol distributions and inferences as to aerosol origin were taken from number distributions. All distribution plots presented in this thesis were normalized to the bin widths listed in Table 3.5. For example, in Figure 3.14 distributions were generally either monomodal (having one peak; solid line) or bimodal (having two peaks; one usually in the nucleation mode and the other in the accumulation mode; dashed line). There were also a few trimodal (having three peaks; two in the nucleation mode and one in the accumulation mode; solid line with open squares) distributions measured. Trimodal distributions, which may signal a burst of gas to particle conversion (or nucleation event), usually occurred at night when aerosol concentrations were lower. The frequency of bimodal distributions was 5 times greater than monomodal distributions.

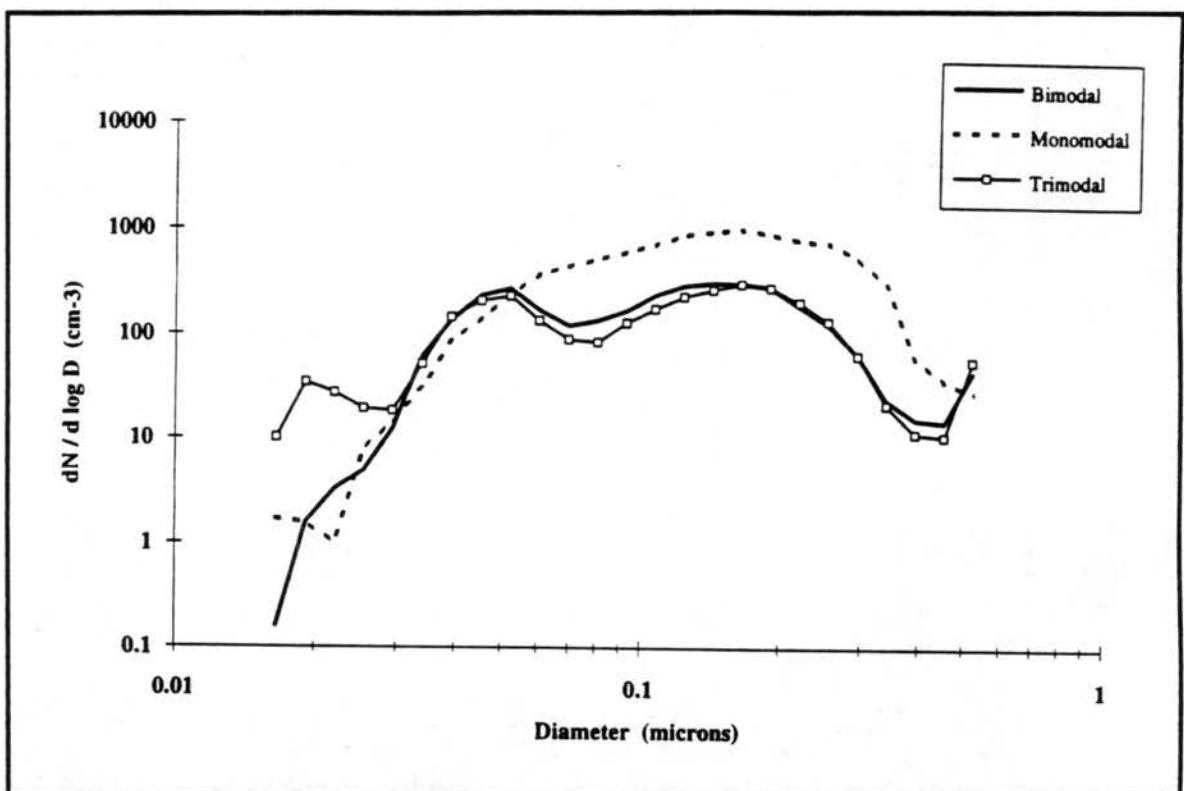


Figure 3.14 Depiction of a Typical Bimodal Distribution (solid line), Monomodal Distribution (dashed line), and Trimodal Distribution (solid line with open squares).

Large differences in number concentration and distribution characteristics between clean and polluted air masses were evident in the DMPS data collected during ASTEX/MAGE. Preliminary back trajectory analyses indicated where to expect transitions from one air mass to another. It became obvious from these that the differences stemmed from sampling in different air masses while the ship was steaming. For clean air masses, the distributions were generally bimodal with number concentrations ranging from 100 to 900 particles cm^{-3} and the diameters of the concentration peaks between 0.04 μm to 0.06 μm and at 0.17 μm . Figure 3.15 shows several representative measurements from Lagrangian #1, which took place primarily in a clean environment. Distributions were generally monomodal in polluted air masses with number concentrations ranging from 800 to 1400 cm^{-3} and peak diameters between 0.15 μm and 0.3 μm . Figure 3.16 shows representative data taken during an intensive sampling period that occurred near the end of the cruise (Intensive #4) while the ship was primarily in a polluted air mass. These measurements were very similar to those made by Hoppel et al. (1990).

Analysis of the ship's data shows that the average air temperature during the measurement periods was 20.0 $^{\circ}\text{C}$ and the dewpoint was between 14.0 and 17.0 $^{\circ}\text{C}$ (at sea level pressure). Averaging of the DMPS data indicated that the average peak diameters of the two modes of a "clean" marine distribution were 0.04 μm (nucleation mode) and 0.17 μm (accumulation mode) and the average mode of a "polluted" air mass to be 0.19 μm . The average concentrations in the peak diameter bins were 50 to 100 particles cm^{-3} .

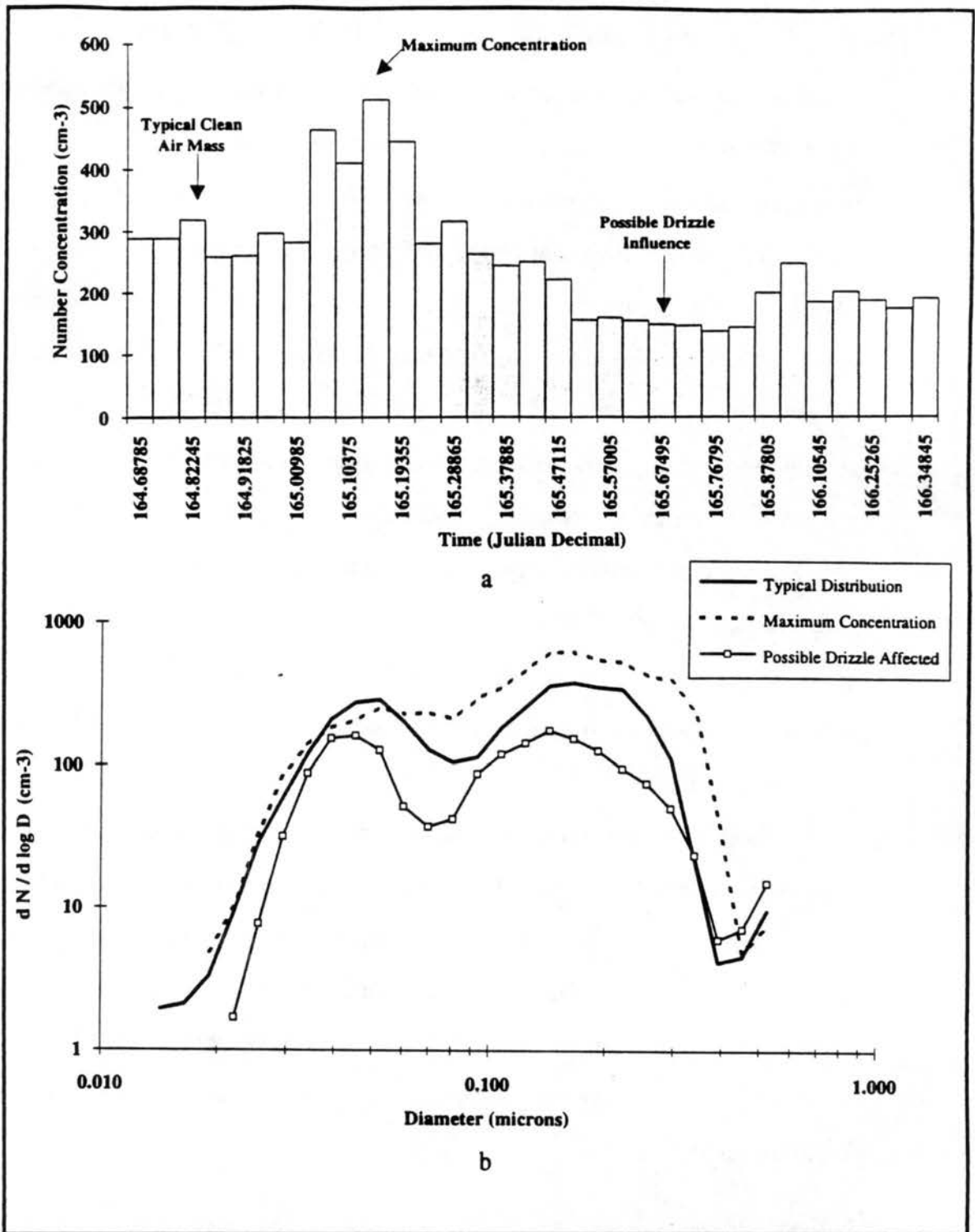


Figure 3.15 Representative Measurements of a Clean Marine Airmass. Measurements Taken during Lagrangian #1. Time History of Number Concentration Depicted in (a). Distribution of Interest Depicted in (b).

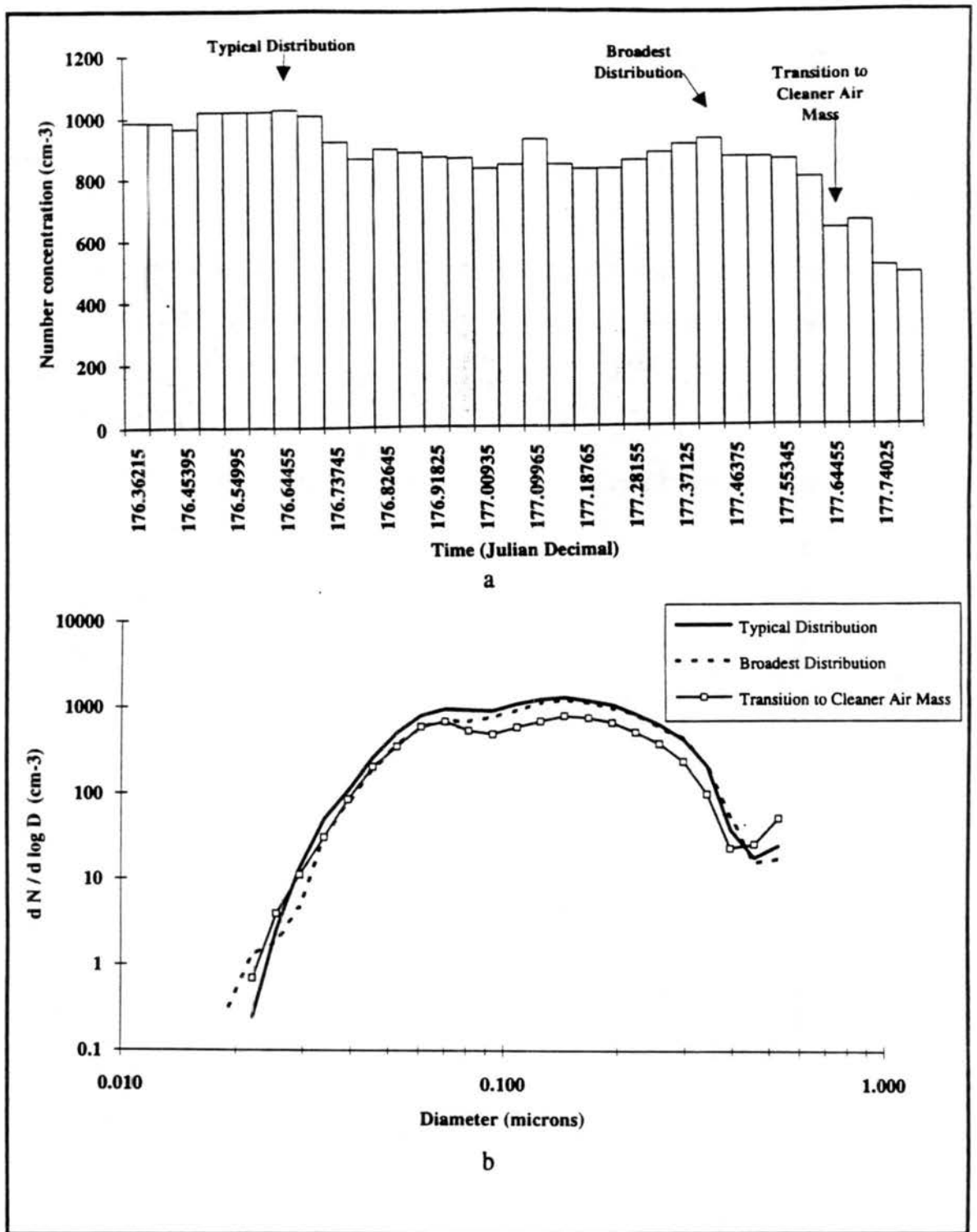


Figure 3.16 Representative Measurements of a Polluted Marine Air Mass. Measurements Taken during Intensive #4. Time History of Number Concentration Depicted in (a). Distributions of Interest Depicted in (b).

3.4c Observations

From the measurements made, it can be inferred that the air mass boundaries are fairly sharp. For example, the total integrated concentration of the submicron distributions shown in Figure 3.17 increased from 500 particles cm^{-3} in the clean air mass to 1300 particles cm^{-3} in the polluted air mass with a peak of 1400 particles cm^{-3} occurring in the intervening time. The submicron aerosol distribution also changed from bimodal to monomodal. This transition occurred within a three hour time frame, which represents approximately a 25 km distance. Measurements of total CN concentration obtained by NOAA/AOML supported the observation of the rapid change from clean to polluted air mass.

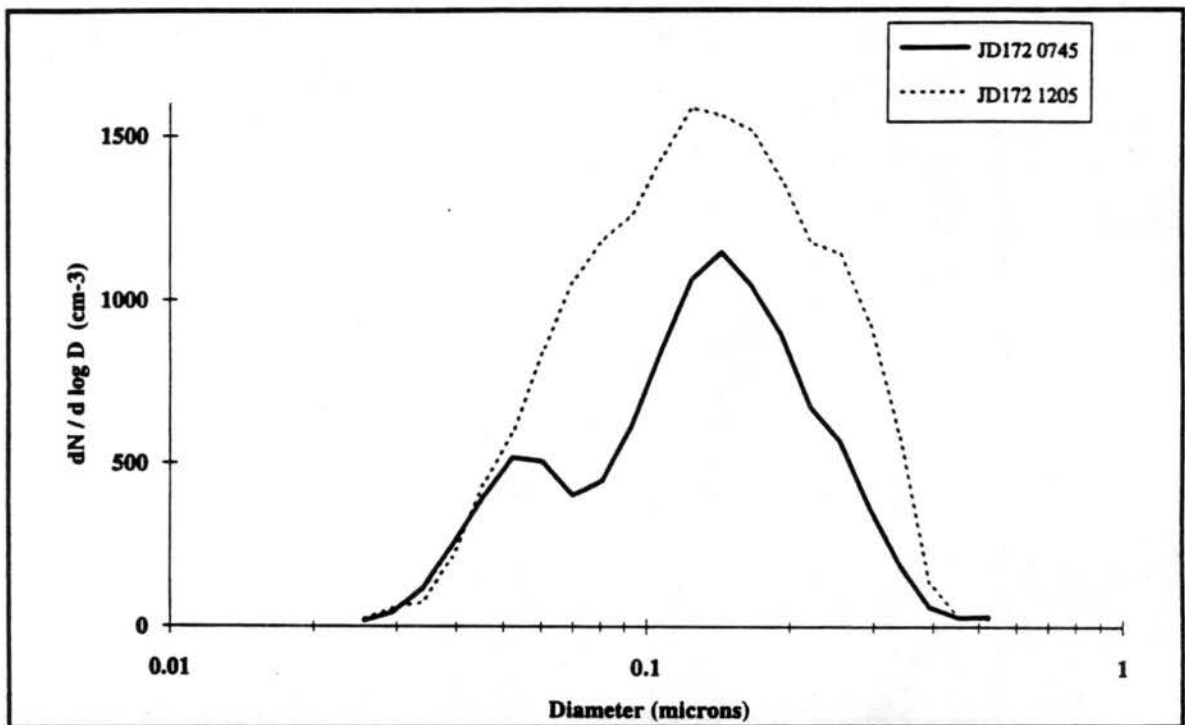


Figure 3.17 Clean Air Distribution (solid line) and Polluted Air Distribution (dashed line) measured by DMPS on JD172 starting at 0745 and 1205 respectively.

Evidence of horizontal mesoscale variability (on the order of 10 to 100 km) was also observed. For example, the aerosol fraction in each mode may vary. Figure 3.18 depicts a series of 3 measurements taken while steaming within an airmass. Several variations in the bimodal distributions can be seen. The JD165 0850 measurement had a distribution biased toward the accumulation mode, with 58 % aerosol number fraction found in this mode. The next hourly measurement indicated that the aerosol number fraction was primarily equal in both modes (for example the JD165 0950 measurement). In contrast, the JD165 1050 measurement (2 hours after the initial experiment) indicated 45 % aerosol number fraction in the accumulation mode, thus indicating a shift in bias

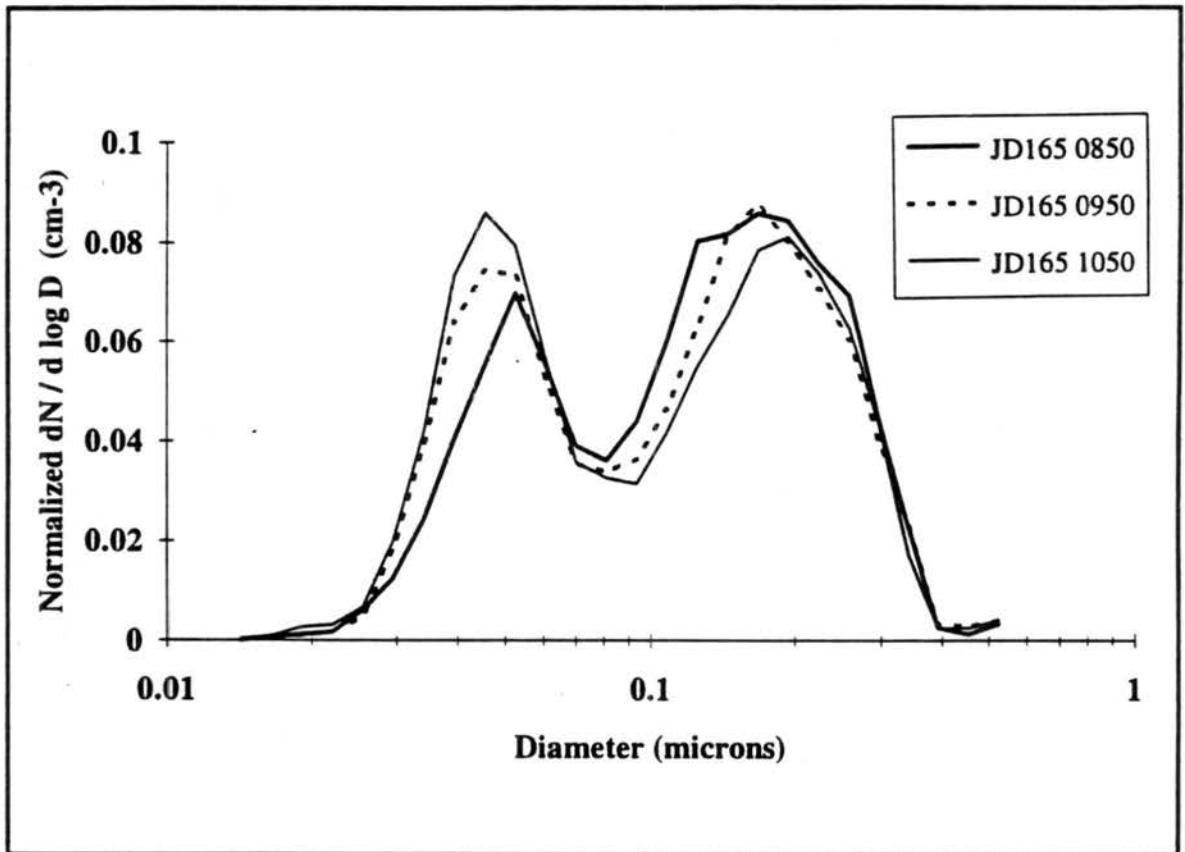


Figure 3.18. Depiction of observed horizontal air mass variability. The JD165 0850 distribution is represented by a thick solid line. The JD165 0950 distribution is represented by a dashed line. The JD165 1050 is represented by a thin solid line.

from accumulation to nucleation mode over a three hour period. These mesoscale differences were measured in an 18 km distance within what is presumed to be the same air mass. There was drizzle present in the air mass before and after the measurements were taken, so the variability may be attributed to scavenging by drizzle drops of the accumulation mode aerosol.

In contrast, Figure 3.19 shows that this variability in distribution did not always occur. There was very little change in the aerosol fraction in each mode throughout this sampling period, which spanned a 22 km distance. Weather logs show that there was no drizzle reported for several days before these measurements were taken and the atmospheric conditions were relatively stable (i.e. no significant wind shifts or changes in sea surface roughness).

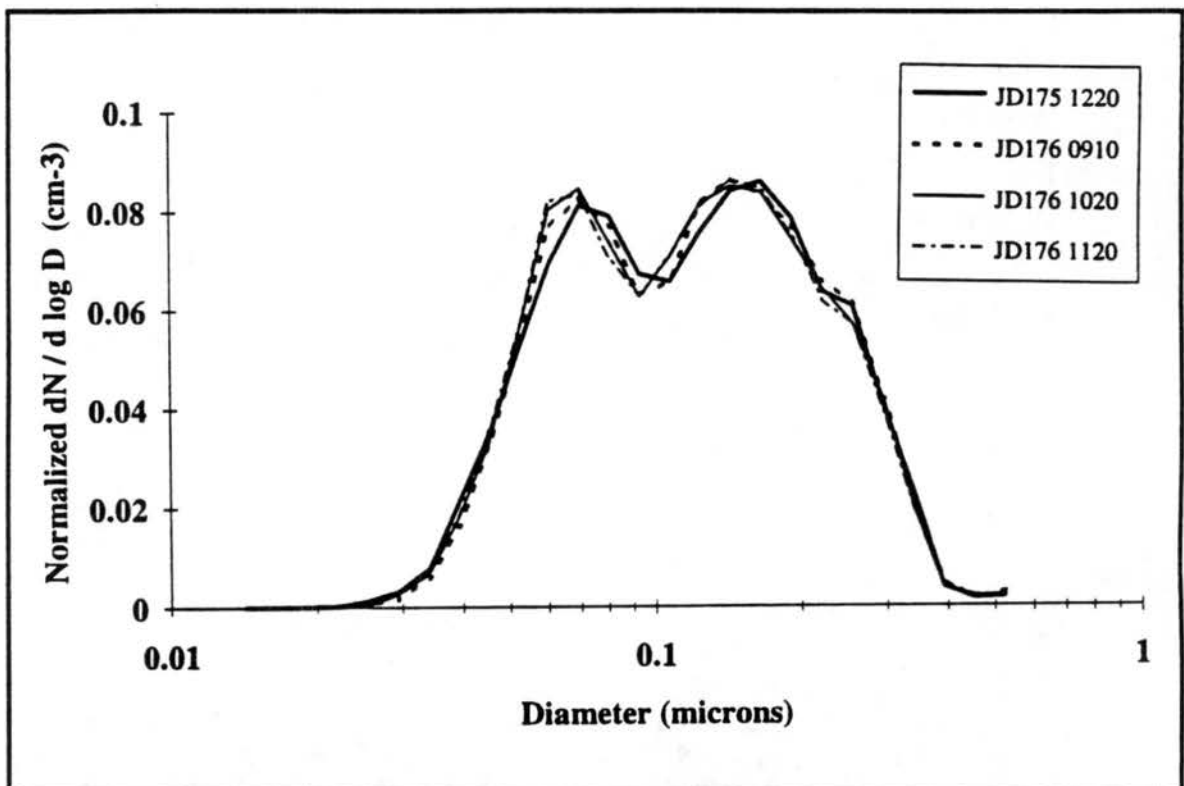


Figure 3.19 Distributions taken shortly after holding station at 28.5° latitude and 24.3° longitude on JD176.

3.5 Summary

The TSI Model 3932 DMPS system was used to take marine aerosol distribution measurements. Comparison to other, independent aerosol measurements show a general agreement in distribution shape but some disagreement in number concentration between the ASASP and DMPS measurements. An investigation into loss of particles in the tubing system uncovered an average particle loss of 12%. The rest of the number concentration discrepancy may be explained by uncertainties in both the DMPS measurements and the other measurements.

Analysis of the data showed that the distributions were generally bimodal in clean air masses with number concentrations ranging from 100 to 900 particles cm^{-3} , while distributions were generally monomodal in polluted air masses with number concentrations ranging from 800 to 1400 cm^{-3} . Both the shapes of the two types of distributions and the concentrations agree with measurements presented by Hoppel et al. (1990). Bimodal distributions occurred 5 time more frequently than monomodal distributions.

From the ship data, the temperature chosen to represent marine surface conditions in the CSU dynamic cloud chamber was 20.0 °C, and the dewpoint at sea level between 14.0 °C to 17.0 °C. The two diameters chosen to represent the two modes of a "clean" marine distribution were 0.04 μm and 0.17 μm . The average concentrations chosen to represent these peaks were 50 and 100 particles cm^{-3} .

Observations of air mass transition and horizontal mesoscale variability were made from the data set obtained during ASTEX/MAGE. Investigation of these trends is ongoing.

CHAPTER 4

CLOUD CHAMBER STUDY - PROJECT DESCRIPTION AND RESULTS

4.1 Purpose

The primary objective of the controlled cloud chamber simulations was to study how submicron aerosol loading and updraft velocity affect the microphysical properties of initial marine stratus type clouds. The following goals were set to obtain this objective:

- 1) Determine if a well controlled study of initial marine stratus clouds (i.e., slow updraft velocity, low CCN concentration, and warm initial dewpoint temperatures) can be conducted using the CSU dynamic cloud chamber and the DMPS system.
- 2) Develop a technique to generate and inject aerosols of known physical and chemical characteristics similar to those described in Chapter 3 of this thesis as cloud condensation nuclei into the CSU dynamic cloud chamber.
- 3) Use the chamber data to provide a link between modeled clouds and natural clouds, by comparing key parameters like the aerosol number fraction nucleated as cloud droplets in the cloud chamber, to both natural cloud data and model output. Conclusions about the effect of variations in updraft velocity and aerosol loading were drawn from these comparisons.

- 4) Determine lower boundaries of updraft velocity and number loading that can be successfully used in future chamber experiments

4.2 Experimental Design

4.2a General Approach

Incorporation of ASTEX/MAGE Data

As described in Chapter 3, data from the ASTEX/MAGE field project was collected and averaged. This data was used to determine the state conditions (temperature and dewpoint temperature), average aerosol distributions, and a representative chemical composition of particle used in this portion of the study. Also, distribution measurement techniques and instrumentation were incorporated into cloud chamber procedures in order to facilitate the well characterized investigation.

From the ship data, the temperature chosen to represent a marine surface condition in the CSU dynamic cloud chamber (see Appendix A) was 20.0 °C, and the dewpoint at sea level to be 14.0 °C to 17 °C. The two diameters chosen to represent the two modes of a "clean" marine distribution were 0.04 μm and 0.17 μm. The average concentrations chosen to represent these peaks were 50 and 100 particles cm⁻³.

Analysis of ion mass derived from high volume cascade impactor filter packs showed that the primary chemical composition of the marine aerosol was ammonium and sulfate. To represent this, ammonium sulfate was chosen as the chemical species for the CCN used in the cloud chamber. Ammonium sulfate was also chosen because its activation as cloud droplets is well characterized.

Description of Experiments

First, background contamination levels in the cloud chamber were determined. The aerosol injection procedure was then formulated using the DMA for the generation and the CNC as a measure of aerosol concentration in the chamber. The complete DMPS system was also used to measure and verify the distribution of the injected aerosol. The technique used for conducting adiabatic expansions to simulate the updraft velocities in the cloud chamber was then adjusted to accommodate for slower updraft velocities. Finally, the experiments were conducted as summarized next.

Clouds were activated on ammonium sulfate particles with four distinct types of aerosol distributions and at three different updraft velocities. A total of 50 experiments were conducted, however, the first five were considered exploratory experiments. The DMA was used to generate and inject the monodisperse aerosol into the cloud chamber and the DMPS system was used to verify the injected aerosol distribution. The experimental DMPS data was used to initialize a microphysical model that simulated cloud formation from initial conditions in the chamber. The droplet spectra and state variables predicted by the model were compared to experimental measurements.

The four types of aerosol included in this investigation were monodisperse, two spike, spike and polydisperse, and polydisperse. Within the monodisperse category, there were four different diameter/concentration variations chosen. Table 4.1 summarizes the average concentrations used for each distribution type. The simplest possible aerosol distribution, monodisperse, was used initially. The diameter sizes chosen for the monodisperse "spikes" were representative of the peak diameters measured in a bimodal distribution.

Concentrations representative of the peak diameter concentrations were used for CCN. These are referenced as "50 small particles", "50 large particles" and "100 large particles" in Table 4.1. The number in the distribution type label refers to the total number concentration put into the cloud chamber. As can be seen from Table 4.1, this number was an ideal number, and the actual number of aerosol injected may be slightly greater than the label reference.

Table 4.1.
Summary of General Description and Concentration of Each Aerosol Distribution Type Used in the Cloud Chamber Study.

Aerosol Distribution Type	General Description of Type	Actual Average Concentration (cm ⁻³)
50 small particles	peak at 0.04 μm	70
50 big particles	peak at 0.17 μm	50
100 big particles	peak at 0.17 μm	150
2 spike	peak at both 0.17 and 0.04 μm	200
spike and polydisperse	peak at 0.26 μm and polydisperse dist. with cut-off at 0.14 μm and peak at 0.08 μm	300
high concentration small particles	peak at 0.04 μm	1000
polydisperse	polydisperse dist. with cut-off above range of DMPS (0.535 μm and peak at 0.08 μm	1000

The results of experiments with monodisperse aerosol injected, Figures 4.1, were analyzed for deviations from theory in order to determine how closely the chamber modeled theory. The two spike distribution type, depicted in Figure 4.2, was included in the data set to represent a "first order approximation" of the bimodal aerosol distributions

measured during ASTEX/MAGE. Aerosol concentrations used for all of the types of distributions described above are much lower than had been previously used in the chamber for experiments. The spike and polydisperse distribution (Figure 4.3) was used to increase particle concentrations and determine if smaller diameter aerosols can be noticeably activated during an expansion. A high concentration monodisperse distribution of $0.04 \mu\text{m}$ particles was also included in the data set to allow for comparison to data collected using low concentrations. Also, a high concentration, monomodal polydisperse distribution of aerosol (Figures 4.4) was used for comparison to experiments that have been conducted in the chamber in the past.

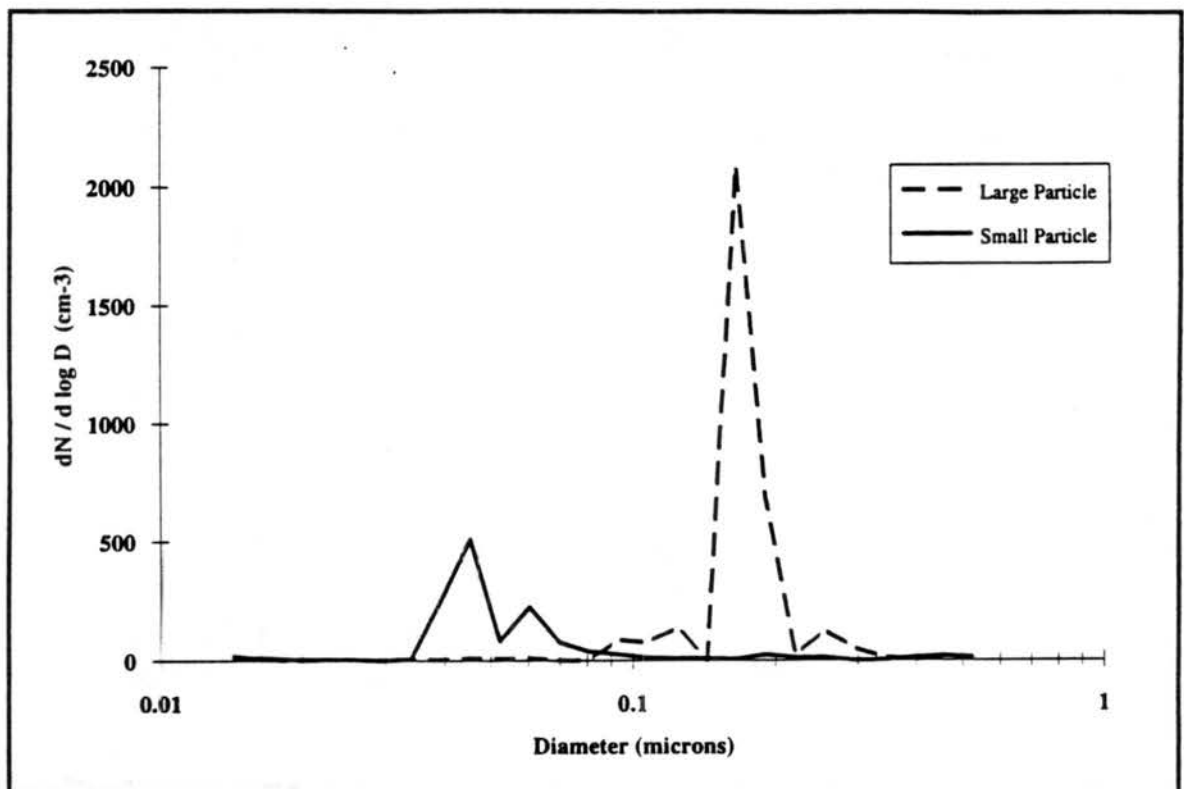


Figure 4.1 Example of 50 Small Particle (solid line) and 100 Large particle (dashed line) Aerosol Distribution injected into the Chamber.

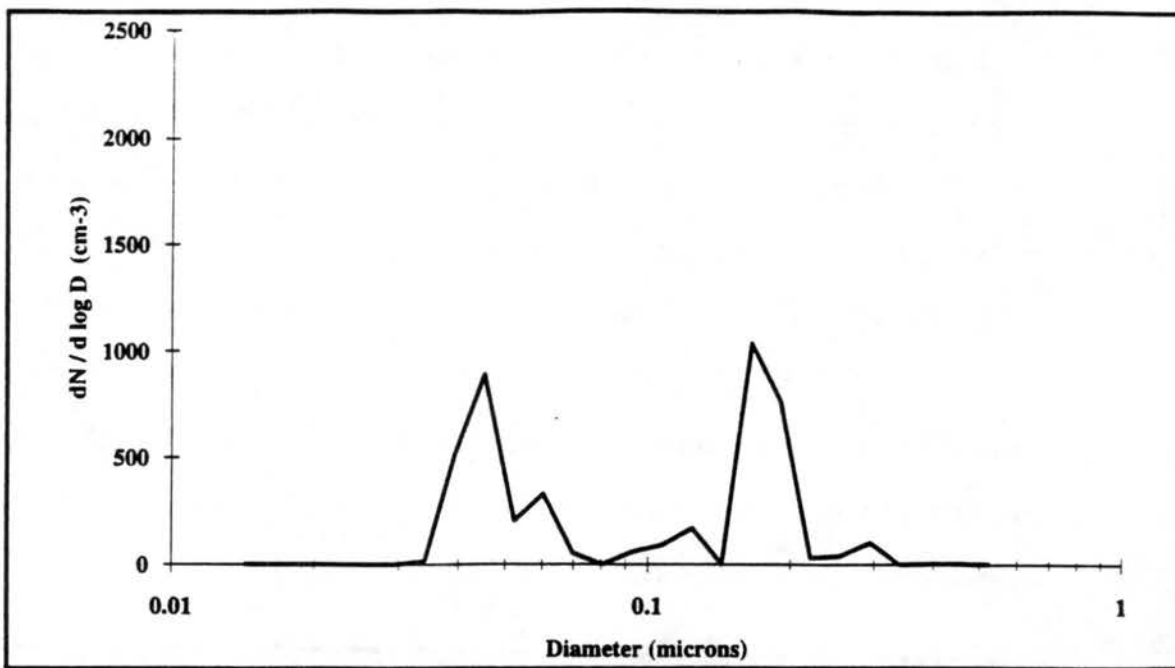


Figure 4.2 Example of 2 Spike Aerosol Distribution Injected into the Chamber

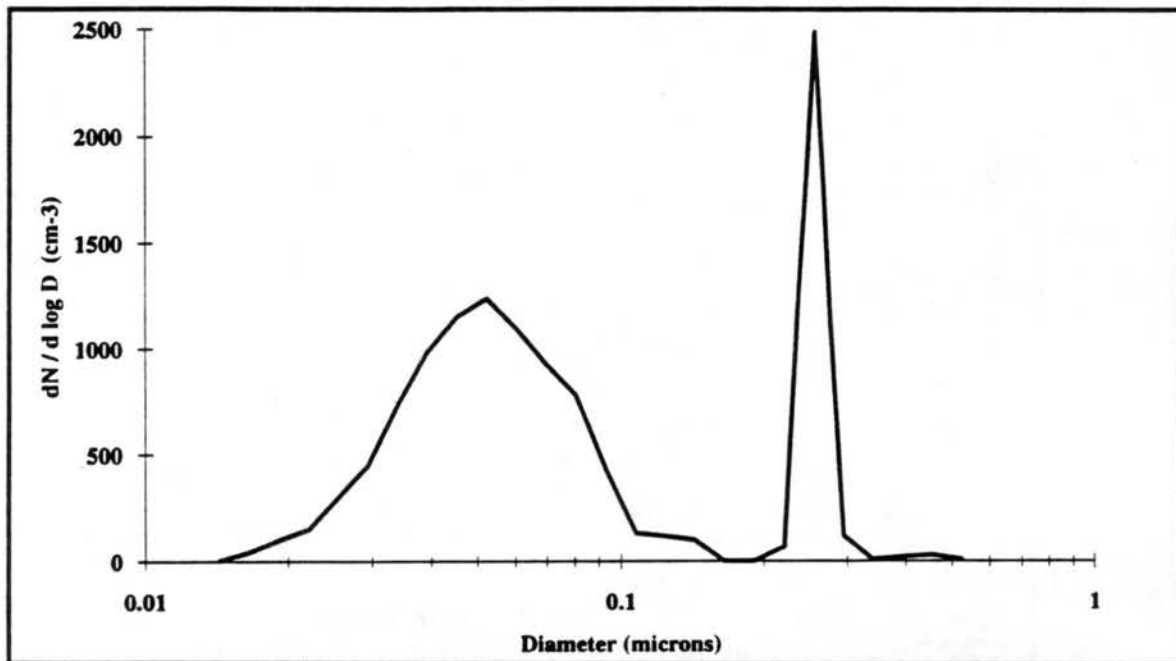


Figure 4.3 Example of Spike and Polydisperse Aerosol Distribution Injected into the Chamber.

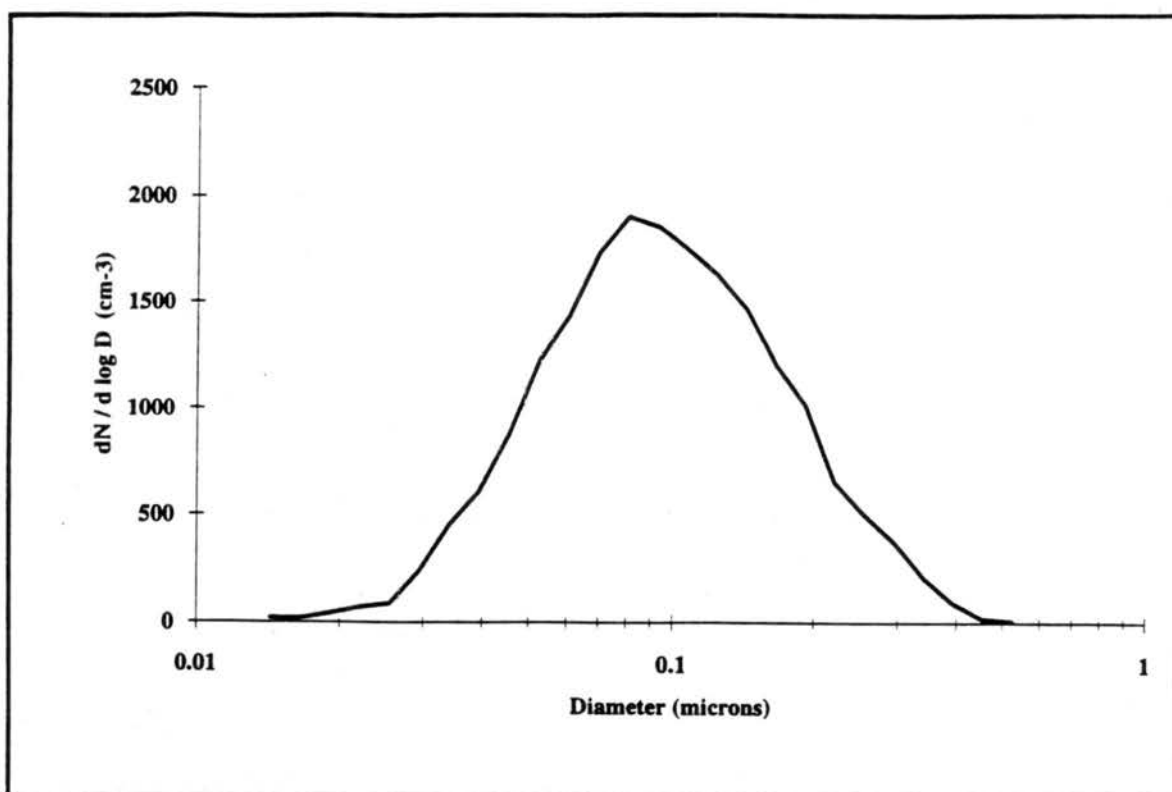


Figure 4.4 Example of Polydisperse Aerosol Distribution Injected into the Chamber.

Prior to this investigation, most experiments were conducted in the chamber at simulated updraft speeds greater than 2.5 m s^{-1} . The slowest possible expansion is listed as 0.2 m s^{-1} with no specified tolerance (DeMott, 1990). To determine more precisely the lower bound of expansion rates the chamber was capable of producing, expansion rates representative of 0.5 m s^{-1} , 1.0 m s^{-1} and 2.0 m s^{-1} updraft velocity were chosen. These rates also characterized marine stratus conditions in the chamber. Table 4.2 summarizes the aerosol distribution type and updraft velocity of each experiment, listed by experiment number. To eliminate system bias in the experimental results, the order the experiments were conducted in was somewhat random. After the initial experiments were completed, most aerosol distribution types were repeated, except the high concentration ($1000 \text{ particle cm}^{-3}$) experiments, which were only done once.

Table 4.2.
Summary of Experiments Done with Each Aerosol Distribution Type and at Each Updraft Velocity

Updraft Velocity and Aerosol Distribution Type	Experiment Numbers
2.0 m s⁻¹	
50 small particles	24, 25, 48
50 big particles	20, 21
100 big particles	22, 23, 49
2 spike	36, 37
spike and polydisperse	29, 31, 50
high concentration	40
polydisperse	45
1.0 m s⁻¹	
50 small particles	9, 10, 11, 12, 46
50 big particles	1, 2, 5, 6
100 big particles	3, 4, 7, 8, 47
2 spike	32, 35
spike and polydisperse	26, 27
high concentration	39
polydisperse	44
0.5 m s⁻¹	
50 small particles	16, 18, 41
50 big particles	13, 15
100 big particles	14, 19, 43
2 spike	33, 34
spike and polydisperse	28, 30
high concentration	17, 38
polydisperse	42

Comparison to Theory

Data from the cloud chamber expansions were compared to theoretical predictions from the Atmospheric Cloud Physics Laboratory (ACPL) adiabatic expansion

model (Marshall Space Flight Center, 1980). The ACPL model can describe the events taking place in a gas parcel of arbitrary mass, volume or shape. The physical processes considered in the model are adiabatic expansion, condensational growth of droplets on aerosol particles, and the release of latent heat of condensation as water vapor is converted to liquid water. Processes not included in the model are heat exchange between the parcel and the outside environment, needed to simulate wall effects in the chamber, and sedimentation of droplets .

There is some flexibility in the initialization of a model run. Pressure and temperature in the model run can be initialized as either ambient pressure and temperature or cloud base pressure and temperature. Condensation and thermal conductivity coefficients as well as the surface tension of the droplets can be specified. The aerosol distribution is initialized by inputting the number concentration and critical supersaturation of the dry particles and the updraft velocity and duration can also be specified. The model is capable of handling variations in the updraft velocity and duration, but for this study, that feature was not utilized. The length of time the model runs, the averaging time, and the data output frequency can also be specified in the input file. The output file includes a time history of the radii, time, pressure, temperature, supersaturation given in percent, volume, dilution of solute terms, liquid water content, mean diameter, dispersion coefficient, and droplet concentration.

For this study, the pressure and dry temperature were initialized using ambient chamber measurements and the saturation temperature was initialized as the dewpoint measurement from the General Eastern Hygrometer. For each run, thermal conductivity coefficient was assumed to be 1, the condensation coefficient to be 0.3, and surface tension to be 75 dynes cm^{-1} . For the discussion that follows, the aerosol size distribution was initialized for a "representative" case of each aerosol distribution type experiment

using DMPS measurements of number concentration per diameter midpoint, and the critical supersaturation for each diameter was taken from Figure 4.16. Updraft was specified as either 50, 100 or 200 cm s⁻¹ depending on which experiment was being modeled. The model was run on a DEC VAXstation 2000. The data were imported into Microsoft Excel for Windows and plotted against cloud chamber experiment data.

4.2b Instrumentation

Several different instruments were used to generate the monodisperse and polydisperse aerosol that was injected into the chamber. A TSI six-jet atomizer was the primary device used for generating a stream of aerosol that passed through the DMA, which allows a single mobility range to pass through a separate exit, thus discharging an essentially monodisperse aerosol. The product of the six-jet atomizer was also used for a polydisperse aerosol with a cut-off at > 0.52 μm . Due to diameter limitations of the DMPS system, the precise cut-off of the polydisperse aerosol was unable to be determined. A one-jet plastic bubbler system was used in conjunction with a Micro-orifice Uniform Deposit Impactor (MOUDI) to generate a polydisperse aerosol with a cut-off at approximately 0.14 μm . Figure 4.5 depicts the aerosol generation apparatus used. A TSI Model 3010 CNC was used to monitor the number concentration of particles in the chamber during the injection process. Figure 4.6 depicts a schematic of the injection instrument configuration. A schematic of the system used to verify the size distribution of the aerosol injected into the cloud chamber is shown in Figure 4.7. The chamber aerosol was pulled through a DMPS system composed of a second DMA (TSI Model 3071a) and CNC (also a TSI Model 3010). See Appendix A for more details.

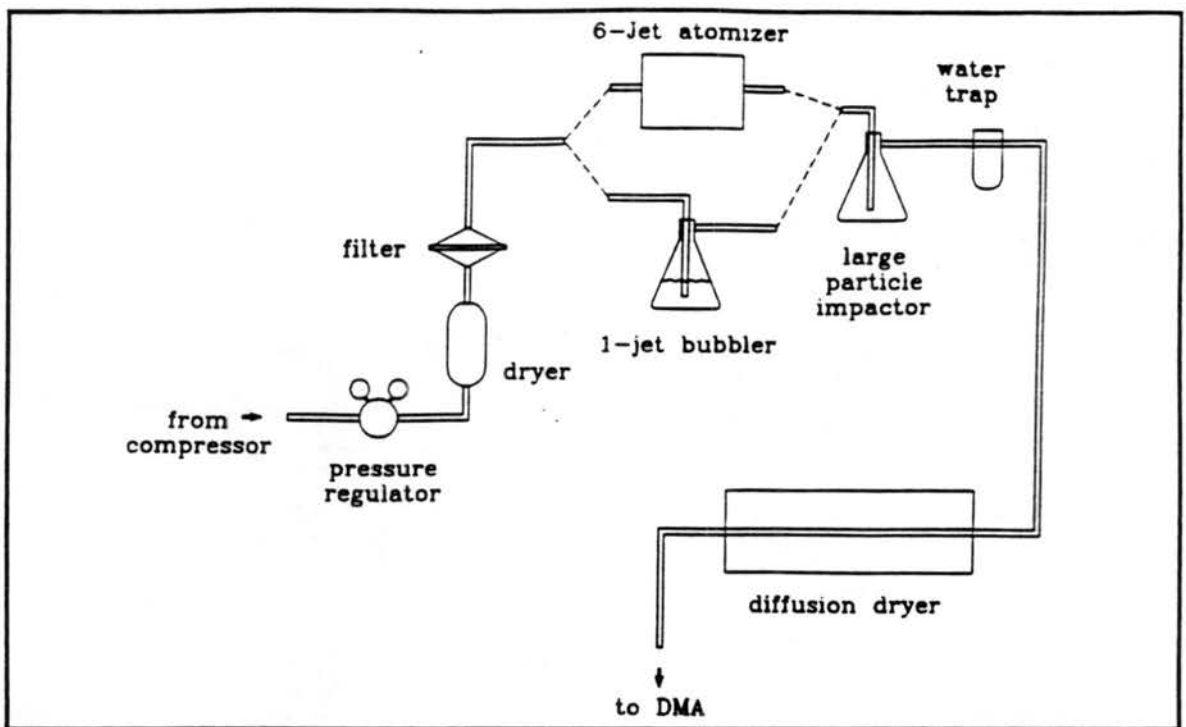


Figure 4.5 Schematic of Aerosol Generation System

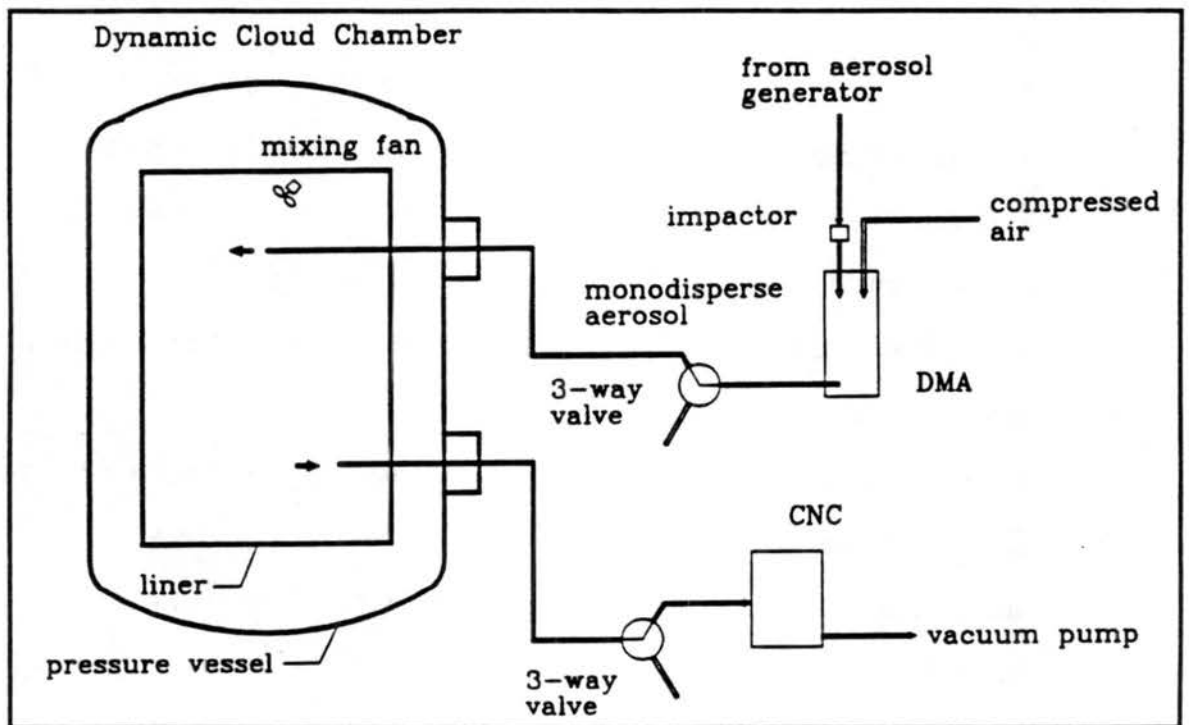


Figure 4.6 Schematic of Aerosol Injection Configuration

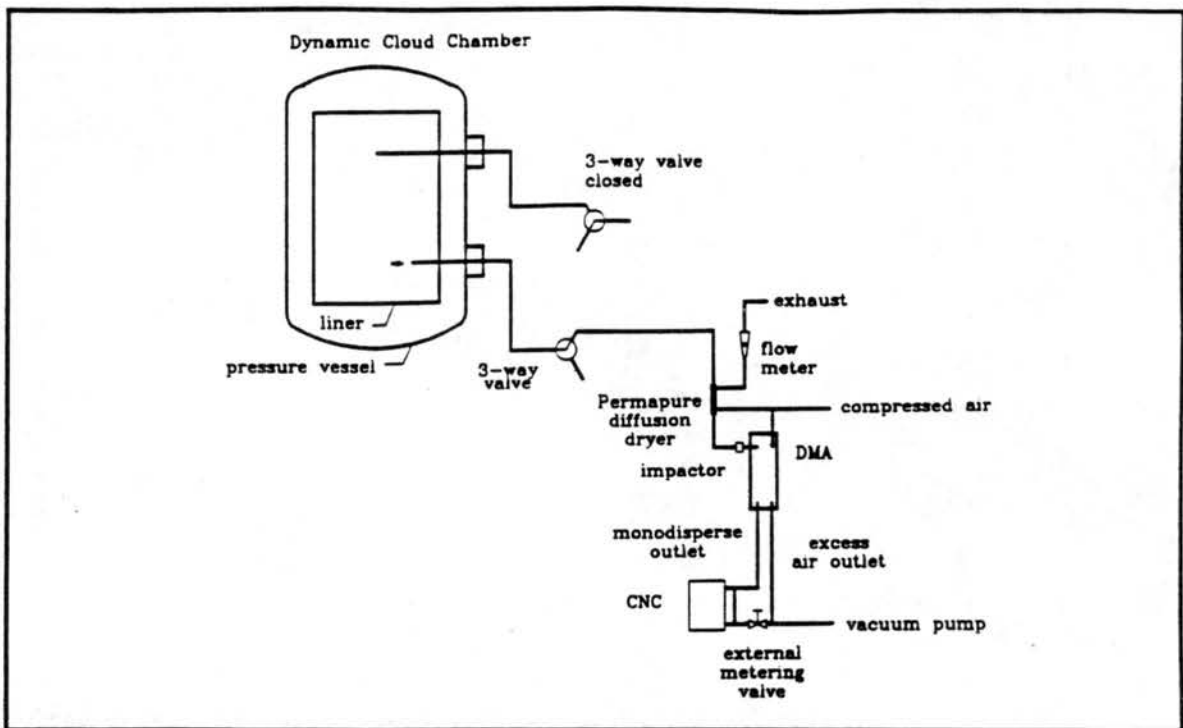


Figure 4.7 Schematic of Aerosol Verification Configuration.

The dynamic cloud chamber housed at the Colorado State University Cloud Simulation and Aerosol Laboratory was used for the CCN activation portion of this study. A full description of the chamber can be found in Appendix A. The chamber allows controlled simulations of an adiabatic ascent of a parcel of air. The primary use for this chamber is the study of small scale cloud processes. A schematic of the dynamic cloud chamber and support systems are shown in Figure 4.8.

The chamber consists of a 1.2 m³ copper inner liner with a 2.0 m³ stainless steel shell. To control initial experimental dewpoint, humidity can be added to the system using a steam boiler system that is tapped into a preconditioning system that circulates filtered air through the chamber. To simulate an adiabatic ascent, air is evacuated at a computer controlled rate from the outer shell using a vacuum pump. Changes in chamber pressure are "communicated" to the inner volume through openings in the top

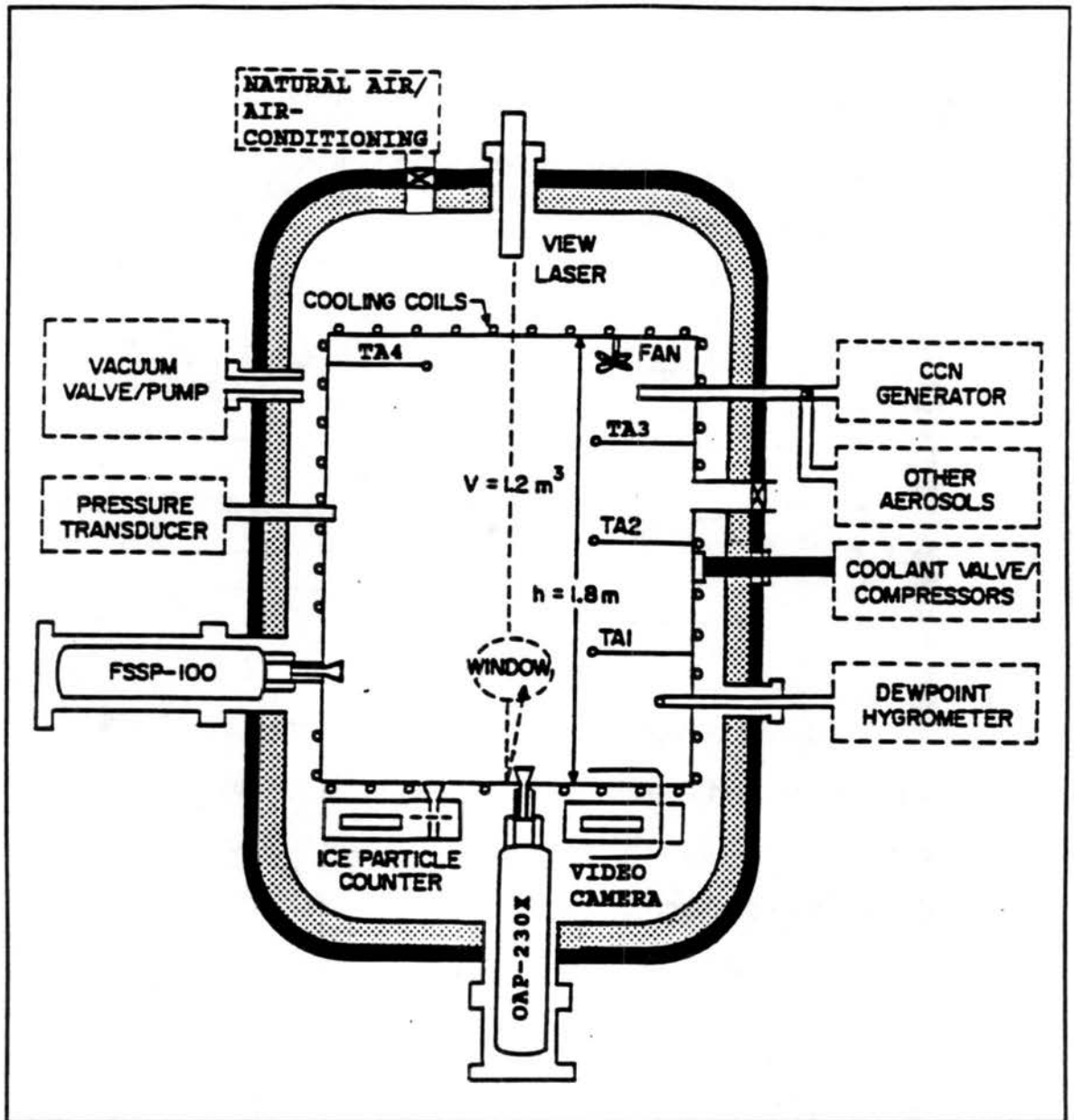


Figure 4.8 Schematic of Colorado State University Dynamic Cloud Chamber.

and bottom of the liner. As the pressure decreases in the inner working volume, the temperature decreases (based on adiabatic expansion principles). To minimize thermal gradients, the inner liner wall temperature is controlled. Standard measurements

recorded during an experiment include air, wall and program temperatures, chamber pressure, dewpoint temperature, and cloud droplet sizes, concentration, and total strobes measured by the Particle Measuring Systems (PMS) Forward Scattering Spectrometer Probe and velocity acceptance ratio (VAR). The usable ranges and system tolerances of the dynamic cloud chamber can be found in Table 4.3.

Table 4.3.
Dynamic Cloud Chamber Working Ranges and System Tolerances

Type	Range	Tolerance
Temperature	-55° to +40° C	+/- 0.2 ° C
Pressure	300 mb to 900 mb	+/- 0.5 mb
Relative Humidity	0.1 % to >100 %	+/- 0.5 in dewpoint temp.
FSSP diameter (Range 1)	2.0 to 32.0 μm	
Simulated Ascent Rate	0.2 m s^{-1} to 20 m s^{-1}	

Values taken from DeMott, 1990.

Values calculated from the FSSP data and recorded include mean diameter, liquid water content, and dispersion coefficient. The data acquisition system uses an IBM-compatible PC-386 20 MHz computer. Data are recorded every one second. More detailed descriptions of the chamber are given in Appendix A, B, and C of this thesis, and DeMott (1990), DeMott and Rogers (1990), and DeMott et al. (1990).

4.2c Procedure

Seven different categories of aerosol distributions were tested in the chamber at three different updraft velocities (see Table 4.2). Experimental procedure for injection into the cloud chamber varied slightly with aerosol distribution type of experiment.

The experimental procedure began by flushing the chamber using the precondition blower while using one of the CNCs to monitor the particle concentration in the chamber. The temperature control was set to control the wall temperature at 20 °C. The mixing fan was turned on and the injection line was flushed. When the background particle concentration in the chamber fell below 0.1 particles cm⁻³, the humidification system was turned on and the chamber was humidified to a dewpoint 15 °C, at which time the compressed air line into the chamber was opened. The chamber continued to humidify to a dewpoint of approximately 16.5 °C, which converts to approximately 14.0 °C at sea level pressure. The humidifier and precondition blower were then turned off and the chamber was locked. With the compressed air line open, the chamber was pressurized approximately 6 to 10 mb above ambient; the compressed air line was then closed. Compression of the chamber dried out the chamber and brought the dewpoint temperature to approximately 16.0 °C.

If monodisperse aerosol of either diameter was to be injected, the six-jet atomizer was used to generate aerosol that was passed through the DMA. If a strictly polydisperse aerosol distribution was desired, the DMA was taken out of the injection line and aerosol was injected directly into the chamber for approximately a half second. If a monodisperse spike in the accumulation mode with a polydisperse distribution in the nucleation mode was required, the large diameter spike was injected first, in the same manner as the monodisperse procedure. The compressed air line was then connected to the one-jet bubbler, which was connected to the MOUDI. The three-way valve was opened to the chamber for only three seconds.

Once the required aerosol concentration in the chamber was reached, the injection line was flushed with compressed air and the three-way valves on both the injection line and the sample line were closed and the mixing fan was turned off. If a representative

chamber aerosol distribution measurement was required, tubing connecting the CNC to the sample port was removed and replaced with tubing connected to a DMPS system. When the four flows were brought into equilibrium, the three-way sample valve was opened to the system, and size distribution measurement was initiated.

With five minutes left in the measurement time or right after injection (if no distribution measurement was taken), the ascent profile was computed and stored in memory by the data acquisition system for 20 °C, initial (ambient) pressure, and 1 °C below current dewpoint. The checklist provided by the computer was checked, and the system was ready to perform an expansion. When the distribution measurement was complete, the three-way valve was closed to the DMPS system and the digital cooling valve was opened to start cooling the walls of the inner liner.

At a wall temperature of 20.5 °C, the ascent profile memory was started and the expansion began. The chamber pressure was monitored constantly, to ensure it followed the program pressure, using a chart recorder. If the air pressure was more than 2 mb off the program pressure, the controlling flowmeter was adjusted accordingly. Most expansions were taken to 700 mb. For a 0.5 m s⁻¹ updraft, this expansion took approximately 2,400 seconds; for 1.0 m s⁻¹, it took approximately 1,600 seconds; and for 2.0 m s⁻¹, it took approximately 800 seconds. The data storage was turned off and pre-expansion temperature and pressure were set into the ascent controller. The temperature of the walls was warmed using an immersion heater. The pressure was returned to ambient by opening the compressed air line. When these two parameters were returned to their pre-expansion state, the precondition blower was turned on to flush the chamber of CCN and the whole procedure was repeated for the next case.

4.3 Instrument Limitations and Data Correction

4.3a DMA

Because of a double charging peak, there is a definite limit to how "monodisperse" generated aerosol can be. To evaluate this limit, a bag made out of static shielding material was filled with the monodisperse aerosol stream, and was sampled from using the DMPS system. This procedure verified that the aerosol generation system was producing generally monodisperse aerosol. However, Figure 4.9 shows that when the voltage is set at 2917 volts, the aerosol generated has essentially a three spike distribution.

The largest concentration peak (at 0.165 μm diameter) is the desired peak and made up of singly charged aerosol. The peak at 0.255 μm is due to doubly charged aerosol that had the correct mobility to leave through the monodisperse outlet.

The peak at the 0.093 μm is an artifact of passing the aerosol through the bi-polar charger twice without neutralizing the charge in between aerosol generation and distribution measurement. The information presented in this peak probably represents particles that were singly charged and in the primary peak when they extracted as monodisperse aerosol and became doubly charged when passed through the DMA for the distribution measurement by the DMPS system. The DMPS software inverts the data assuming a percent of doubly charged given for aerosol passed through the charger only once and does not take into account this increased fraction of multiply charged aerosol.

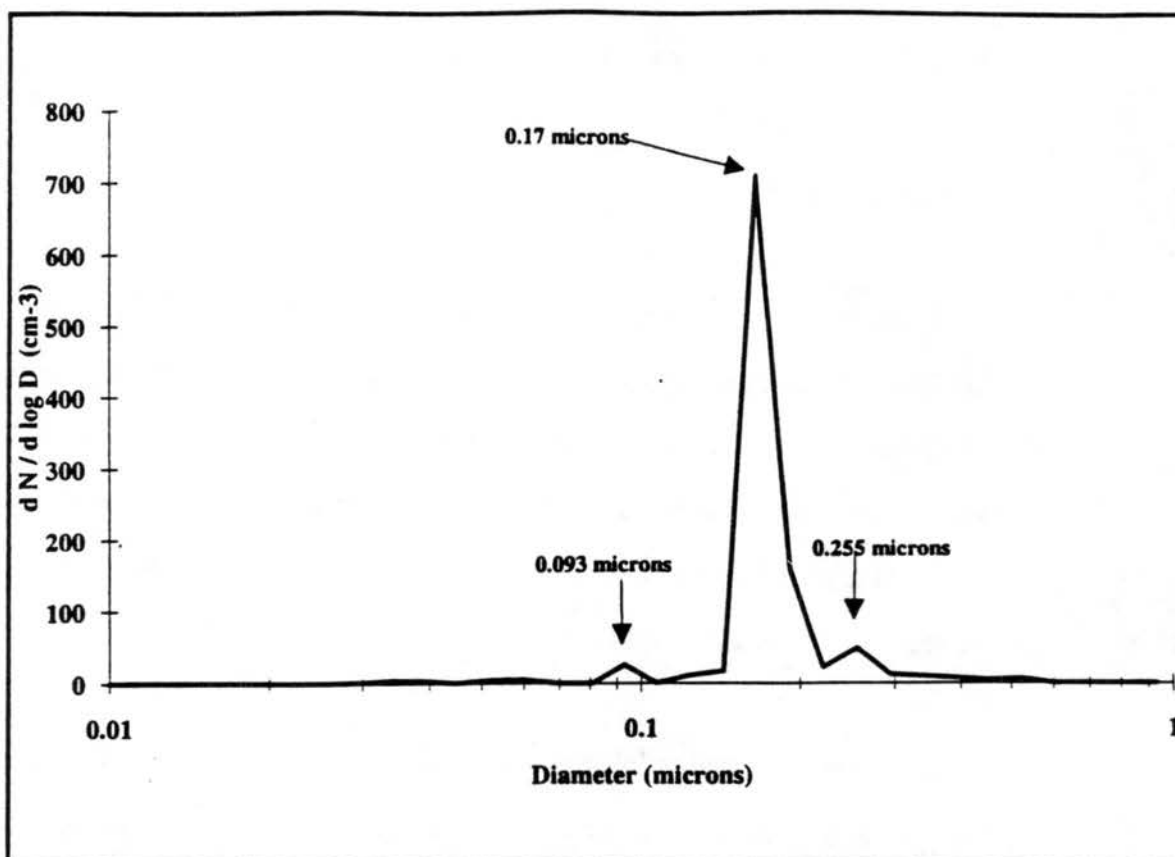


Figure 4.9 Depiction of Typical Distribution of a the Aerosol Present in the Monodisperse Aerosol Stream Generated by the DMA.

4.3b Cloud Chamber

Stability of Aerosol

Test expansions (1.0 m s^{-1} vertical velocity) were performed from 850 mb (approximate ambient pressure of cloud chamber) up to approximately 600 mb on both a "clean chamber" ($< 0.10 \text{ cm}^{-3}$) dry sample and on dry injected samples to determine if any contamination or significant losses of the injected aerosol would occur during the expansion process. The concentration of particles in the chamber was monitored above

750 mb. The flow through the CNC was not stable below 750 mb, consequently the concentrations measured at lower pressures were not determined. Table 4.4 indicates that during the time concentrations were monitored, observed increases in background concentrations were relatively small. Test expansions were also performed on injected aerosol to determine the amount, if any, of aerosol dilution that can be expected during expansion. The method of monitoring was the same as during the "clean chamber" expansion. When the concentrations measured by the CNC are corrected for the decrease in pressure (see Table 4.4), injected number concentration appeared to be constant, as expected.

Table 4.4
Test Expansion Results

Chamber Pressure (mb)	845	825	805	785	765
Clean Chamber Conc. (cm ⁻³)	0.10	0.10	0.14	0.11	0.06
Injected Aerosol Conc. (cm ⁻³)	102	98	102	97	95
Pressure Corrected Injected Aerosol Conc. (cm ⁻³)	102	100	107	104	105

Expansions simulating a 2.0 m s⁻¹ updraft were also conducted on a clean (< 0.10 cm⁻³), moist chamber to see if any cloud droplets form. Approximately 10 droplets cm⁻³ formed at approximately 720 mb, which is well below the pressure of interest for this thesis. Further investigation of the cause of this nucleation is recommended.

Control of Adiabatic Expansion

The control mechanism used in previous studies performed in the cloud chamber for both chamber pressure and wall temperature proved to be incapable of maintaining sufficient control for slower expansions. The pressure control problem stemmed from

the size of the stepping motor valve used to meter the flow being pulled out of the chamber. The valve orifice was too large to effectively handle the small flow rates necessary to perform a smooth, adiabatic expansion at less than 2.0 m s^{-1} . The response time of stepper motor, which drives the valve, was also too slow to allow for the precise control of the valve. To overcome this control problem, the automated stepper motor valve was over-ridden and a rotameter flowmeter was tapped into the vacuum line. The pressure was manually controlled by adjusting the flowmeter valve to keep the chamber pressure value within 2 mb of the program pressure computed by the data acquisition system. Figure 4.10 depicts the difference in the pressure trace between the automatic control and the manual control. By smoothing the pressure trace, uncertainties pertaining to the instantaneous simulated updraft velocity and the adiabatic nature of the experiments were eliminated.

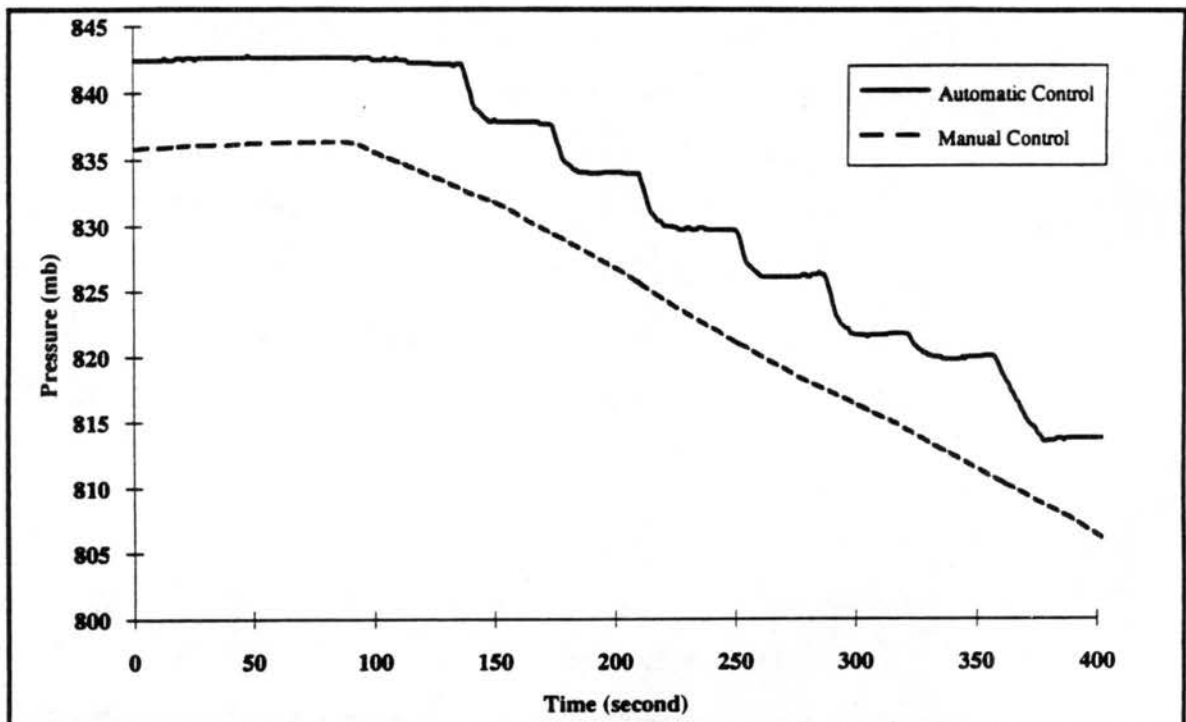


Figure 4.10 Comparison of Manual Pressure Control (dashed line) to Automated Pressure Control (solid line) at 1.0 m s^{-1} .

Temperature control of the walls was also found to be a problem in conducting the experiments. The wall temperatures were maintained by coolant that was circulated in tubing wound around the exterior of the inner liner. The coolant amount was controlled by a 8-bit (256 stage) digital valve that receives instructions from the data acquisition system. A program that compared the wall, air and program temperatures was used to determine how much coolant needed to be circulated. The interval at which these calculations were made was set by the scientist. A common value used was 15 seconds. For 1.0 m s^{-1} and 2.0 m s^{-1} expansions, this value appeared to be acceptable, but for 0.5 m s^{-1} , it was obvious that the interval was too short and was causing large oscillations in the wall temperature. A value of 40 seconds was used as the cooling interval for 0.5 m s^{-1} updraft experiments. Figure 4.11 shows that the result of changing the cooling interval was a simulated expansion with a much more adiabatic temperature profile.

4.3c FSSP

Two primary concerns affecting the data presented in this thesis were the effect of the focused sample flow (from the custom sample inlet) on the droplet concentrations recorded, and the possibility that the FSSP may have broadened the calculated dispersion coefficients of the cloud droplet distribution. A complete discussion of these can be found in Appendix B and C of this thesis.

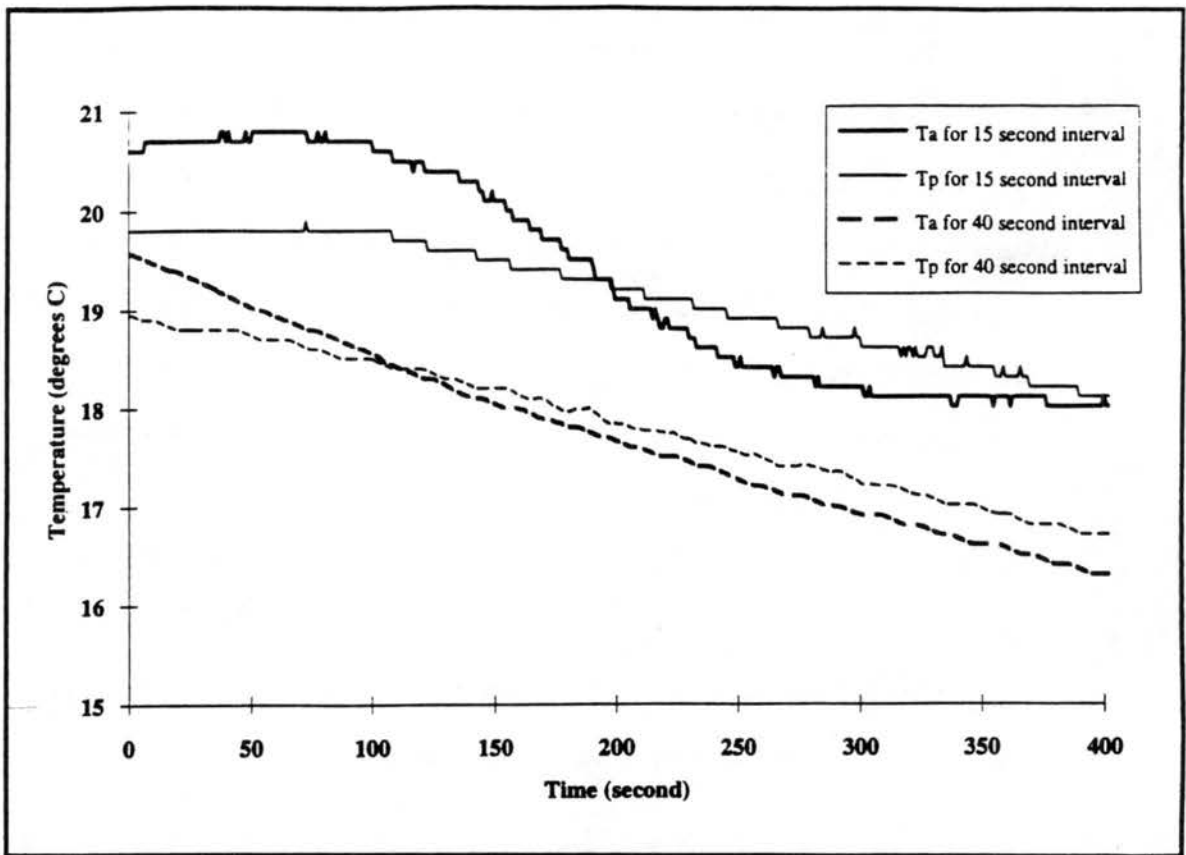


Figure 4.11 Comparison of Effect of 40 Second Cooling Interval (dashed line) and 15 Second Cooling Interval (solid line) on Temperature

Each droplet entering the laser beam is considered a strobe by the FSSP. The strobes have an individual transit time across the laser beam which are used to compute an average transit time by the FSSP. This average is used as the criteria for accepting or rejecting the strobe information for incorporation into the calculated data recorded by the data acquisition system. Strobes with larger transit times than the average are accepted by the FSSP. Essentially, the ratio of strobes accepted to the total strobes is called the Velocity Acceptance Ratio, or VAR. Arguments presented in Appendix B show that, for the sampling system used, there is a relationship between the VAR and the sample volume of the instrument, in the range of VARs seen during these experiments. Data recorded by the data acquisition system were variable VAR values that were all assumed

by the data acquisition system to be at a constant sample volume of 1 cm^3 . Figure 4.12 shows how sample volume, based on arguments presented in Appendix B, should correlate to VAR. Experimental data were corrected to assume an average, constant VAR for each experiments and the respective sample volume as depicted in Figure 4.12. Arguments are also presented in Appendix B that the uncertainty in droplet concentration, for this particular sampling design of the FSSP, may be 15 to 30 %.

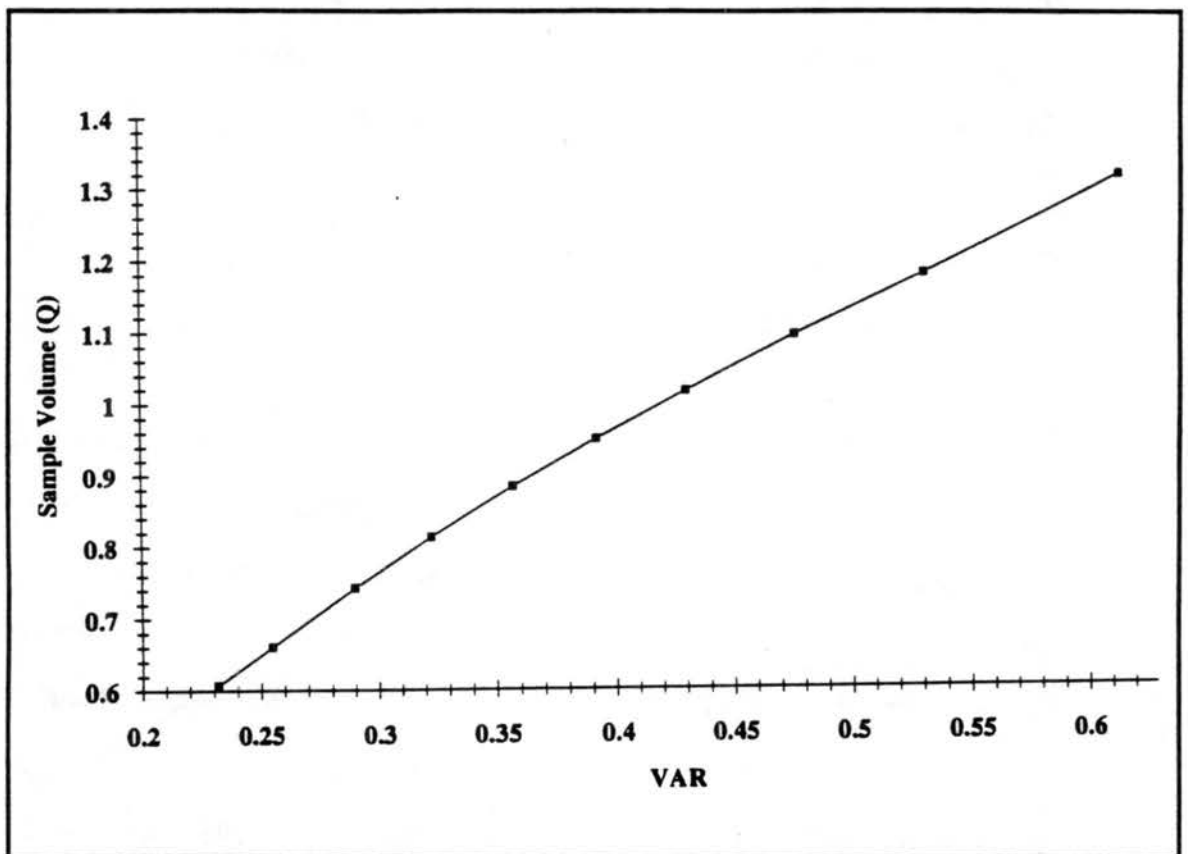


Figure 4.12 Relationship of Velocity Acceptance Ratio (VAR) to Sample Volume of the Dynamic Cloud Chamber FSSP.

Calibration of the FSSP, using glass beads and polystyrene latex beads, was performed after the completion of all the experiments. Details of the calibration can be

found in Appendix C. The calibration data was passed through a model to calculate the effect of Mie scattering peaks on the FSSP bin boundaries. Analysis of this data shows that the average bin boundaries are similar to the manufacturer specified boundaries on Range 1. However, there appears to be large uncertainties in these bin diameters, which may cause broadening of dispersion coefficient (see Appendix C).

Calibration runs using 3 μm latex beads (dispersion of 0.012) and 12 μm latex beads (dispersion of 0.159) were also done. It was found that the FSSP broadened the dispersion of these beads by 0.12 for the 3 μm and by 0.10 for the 12 μm beads. This implies that there is a likelihood that dispersion coefficients less than 0.10 may not be detected by the FSSP (see Appendix C for more details).

4.3d Dewpoint Hygrometers

The primary measurement of relative humidity (RH), or saturation, in the experiments performed was made using two optical condensation type dewpoint hygrometers (a General Eastern model 1200 and a EG & G, model 922). The tolerances of these two instruments are 0.3 and 0.5 $^{\circ}\text{C}$. The response time of both instruments is 1.5 $^{\circ}\text{C s}^{-1}$. As the expansion draws closer to cloud point, the rate of change in relative humidity of the air, which is calculated from dewpoint temperature, exceeds the response time of the instrument, especially at the faster expansion rate simulating a 2.0 m s^{-1} updraft velocity. For this reason, dewpoint measurements, and thus relative humidity values, are unreliable above approximately 98 % RH, and only qualitative information may be gained from the RH above this threshold.

4.4 Results

4.4a Thermodynamics

Equations

Equations that describe the thermodynamic conditions in the cloud chamber include the overall adiabatic process, the dry adiabatic lapse rate, and the moist adiabatic lapse rate. An adiabatic process is defined as changes in temperature of a volume that are prompted by a change in pressure or density only, and not by an addition or removal of heat. Many of the temperature changes in the atmosphere can be describe as adiabatic. Rogers and Yau (1989) present the derivation of an adiabatic process from the equation of state for dry air, this is given by:

$$c_p dT = \alpha dp \quad (4.1)$$

where c_p is the specific heat at constant pressure, T is temperature, α is density, and p is pressure. The equations for the conservation of energy and the First Law of thermodynamics were also used in the derivation.

Rogers and Yau (1989) also provide a derivation for the dry and moist adiabatic lapse rate in the atmosphere. Equation (4.1) is evaluated with respect to changing height (dz), and using the hydrostatic assumption, yields:

$$\frac{dT}{dz} = \frac{-g}{c_p} = -\Gamma \quad (4.2)$$

where g is gravity and Γ denotes the dry adiabatic lapse rate.

After the air becomes saturated, condensation occurs and the released latent heat will tend to warm the air. As a result, the temperature will decrease with falling pressure at a slower rate than before condensation occurs. By also employing the Clausius-Clapeyron equation in the derivation of an adiabatic lapse rate, the moist adiabatic lapse rate is defined as:

$$\Gamma_s = -\frac{dT}{dz} = \Gamma \frac{\left[1 + \frac{L w_s}{R' T}\right]}{\left[1 + \frac{L^2 \epsilon w_s}{R' c_p T^2}\right]} \quad (4.3)$$

where T is temperature, z is height, L is the latent heat of condensation, w_s is the saturation mixing ratio, R' is the gas constant, ϵ is 0.622 and c_p is the specific heat at constant pressure. It can be seen from (4.2) that $\Gamma_s < \Gamma$ whenever $L\epsilon > c_p T$.

These equations were used by the dynamic cloud chamber computer control system to determine the air temperature profile to expect during an expansion. Wall temperatures of the inner liner were controlled based on these calculations. The temperature of the walls, however, did not always match the adiabatic air temperature, and in many cases had a minor influence on the air temperature in the chamber.

As can be seen in (4.1), adiabatic processes are dependent on both temperature and pressure, and can be described in terms of the potential temperature, θ . Rogers and Yau (1989) gives a physical description of θ as the temperature a parcel of air would have if, starting with T and p , it was subjected to an adiabatic compression or expansion to a final pressure of 1000 mb. Therefore, potential temperature is a conservative property in dry adiabatic processes and is defined by:

$$\theta = T \left(\frac{1000 \text{ mb}}{p} \right)^k \quad (4.4)$$

where p is pressure, T is temperature in $^{\circ}\text{K}$, and $k = 0.286$ (for dry air). Potential temperature is not conserved once the parcel becomes saturated and increases steadily with decreasing pressure and temperature. Equivalent potential temperature, θ_e , which includes a latent heating term, is used to describe an moist adiabatic process. Due to uncertainties in dewpoint temperature, which affects the latent heating term, θ_e has not been used for analysis in this thesis.

Agreement to Adiabatic Conditions

The measured temperature and pressure of experiments compared with computed profiles provide a measure of the control achieved during experiments. However, it is difficult to obtain a sense for the adiabatic nature of the experiments by considering pressure and temperature separately. Under dry adiabatic conditions θ (defined in (4.4)) is conserved and includes both pressure and temperature in its calculation. Therefore, the variable θ was used to determine whether experiments were adiabatic.

Calculations of θ were done for three representative experiments, along with the corresponding ACPL model predictions, at each updraft velocity, and averaged (Figure 4.13 a-c). In Figure 4.13, the ACPL model results (dashed line) predict a constant θ for approximately the first 400 seconds. This represents the time during the ascent before the cloud forms and has very little impact on the actual cloud processes measured in the chamber. The ACPL θ then changes from a constant value to a steadily increasing value,

which represents the ACPL cloud point and the first stages of the cloud. This is where comparison of experimental θ to ACPL θ is important.

In general, the experiments were not quite adiabatic during the ascent to cloud point, but for at least the first 150 seconds of the clouds, closely approximated adiabatic conditions, but offset from the expected value. For example, in Figure 4.13a, the experimental θ seemed to oscillate about the ACPL θ for the first 300 seconds of the expansion and then appeared to match the θ profile depicted by the ACPL results. The experimental θ profile, however, does not overlap the ACPL one. This could be due to some heat added while the experimental θ oscillated about the ACPL θ . The lack of overlap of experimental θ and ACPL θ during the first 150 seconds of the ACPL cloud suggests that the experiments near cloud point are slightly drier than predicted by the

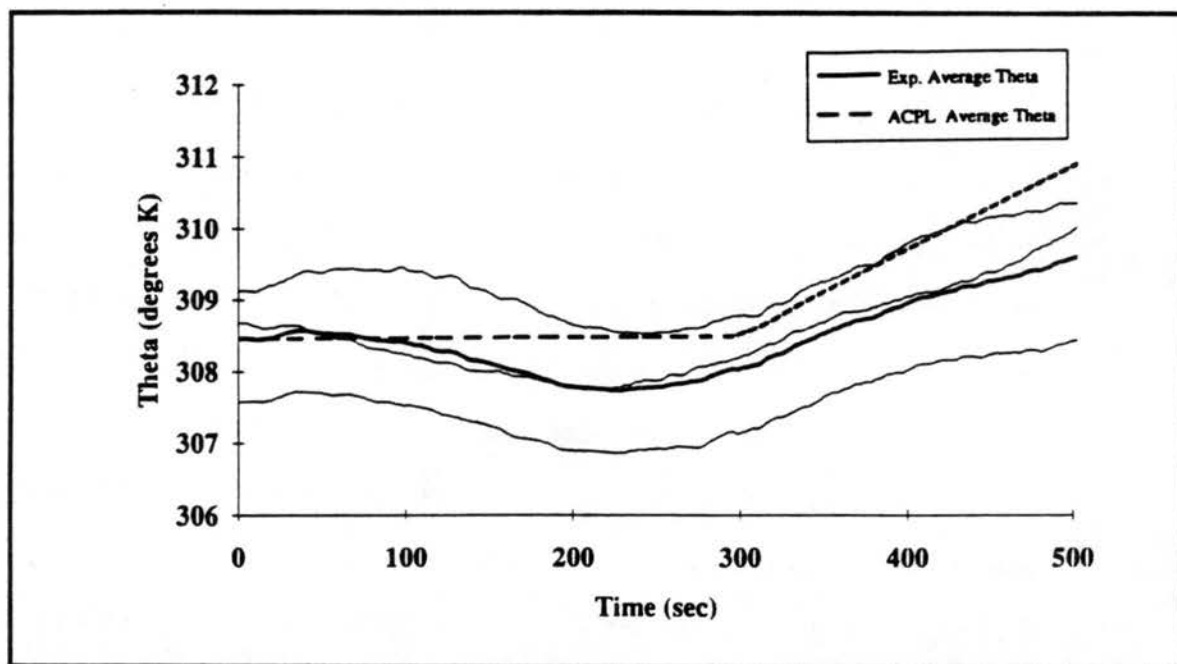


Figure 4.13a Comparison of Average Experimental θ Trace (solid line) to Average ACPL Model θ Trace (dashed line) for 2.0 m s^{-1} . The Individual Experimental θ are Depicted Using Thin Solid Lines.

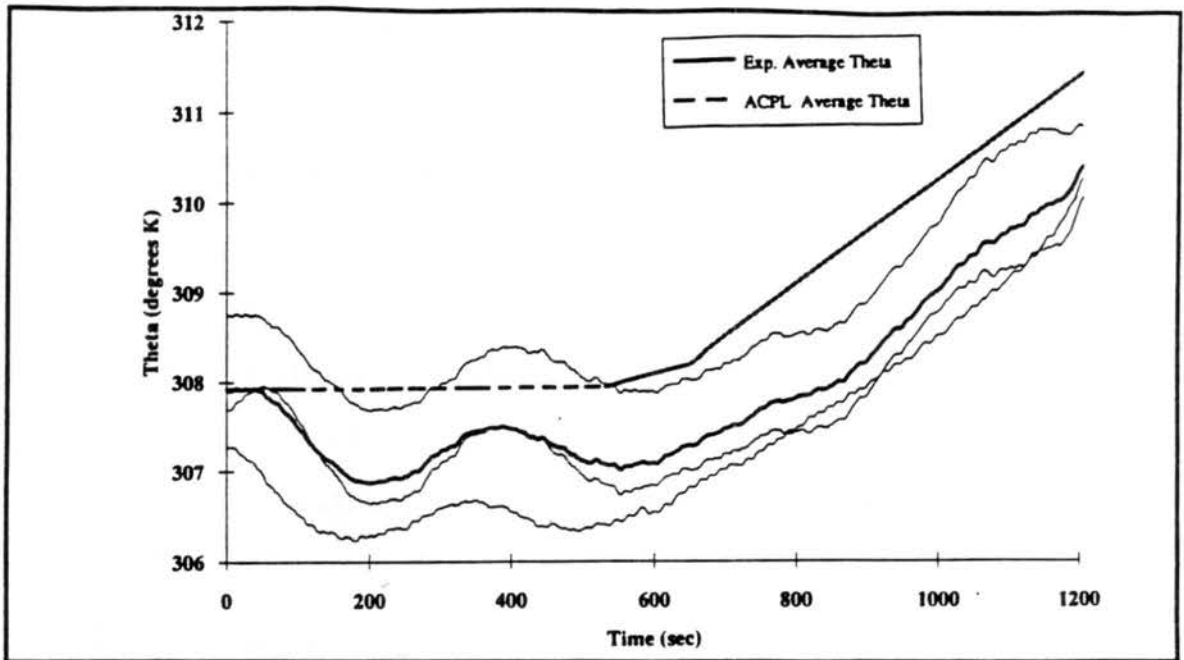


Figure 4.13b Comparison of Average Experimental θ Trace (solid line) to Average ACPL Model θ Trace (dashed line) for 1.0 m s^{-1} . The Individual Experimental θ are Depicted Using Thin Solid Lines.

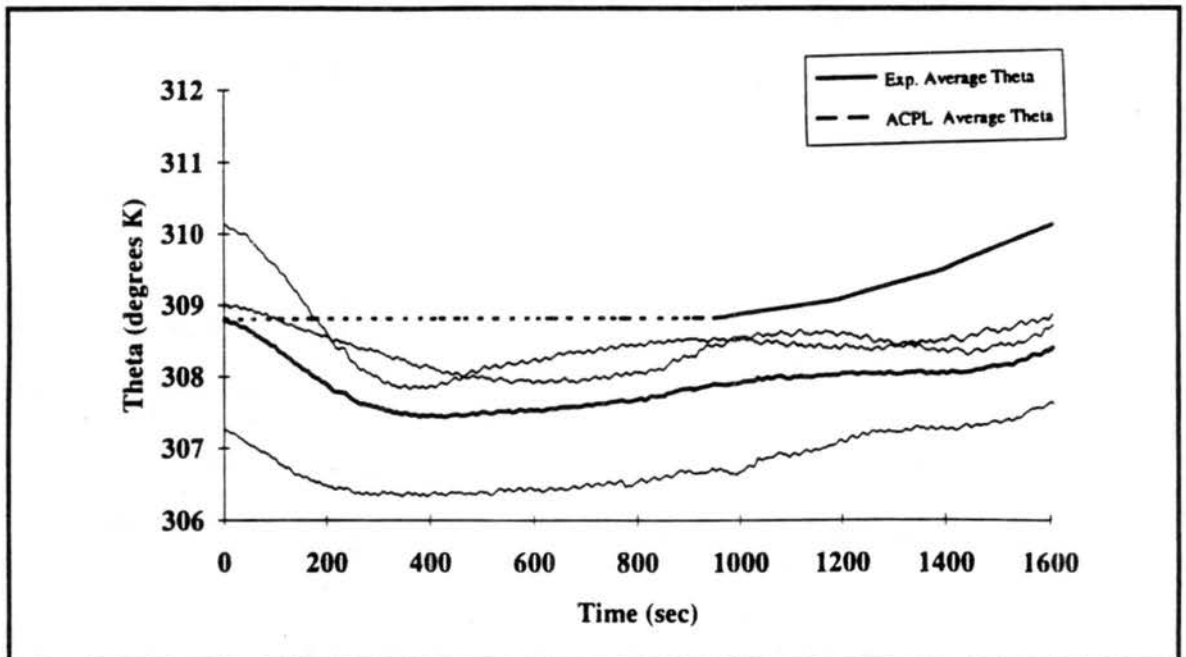


Figure 4.13c Comparison of Average Experimental θ Trace (solid line) to Average ACPL Model θ Trace (dashed line) for 0.5 m s^{-1} . The Individual Experimental θ are Depicted Using Thin Solid Lines.

ACPL model. The effect of the additional dryness would be a delay with respect to the ACPL model of the experimental cloud formation. This is in fact what was observed in the experimental data.

Oscillations of Experimental θ about the ACPL θ slope may also be seen in Figure 4.13b and 4.13c (for 1.0 m s⁻¹ and 0.5 m s⁻¹ respectively). Figure 4.13b indicates that the 1.0 m s⁻¹ experiments were relatively adiabatic during cloud formation. Figure 4.13c shows that the 0.5 m s⁻¹ experiments were not nearly as adiabatic in nature. The rapid decrease in θ in the first 100 seconds of these experiments may be attributed to the wall cooling not being controlled by the computer properly. As can be seen in all of these plots, it takes almost 200 seconds for the computer to gain its best control of the walls.

The oscillations of θ shown in Figures 4.13a-c are probably due to imprecise wall temperature control, which in turn affects air temperature. It can be seen from (4.4) that the exponent of T is much greater than of p (1 and -0.286 respectively). This indicates that T does contribute more to θ than p. However, error in both T and p contributed to the oscillations seen in θ .

One area of data analysis included considering the wall effects on the cloud droplet population. Large differences in air temperature from wall temperature may have set up a thermal gradient large enough to disturb the droplet populations and create inhomogeneities, manifesting an increase of dispersion of the droplet distribution with the measured temperature gradient. Scatter plots (Figures 4.14a-c) of dispersion coefficient vs. ΔT (air-wall) were used to analyze this possibility. Figures 4.14a-c gives an example of one such plot for an experiment at each updraft velocity. There appears to

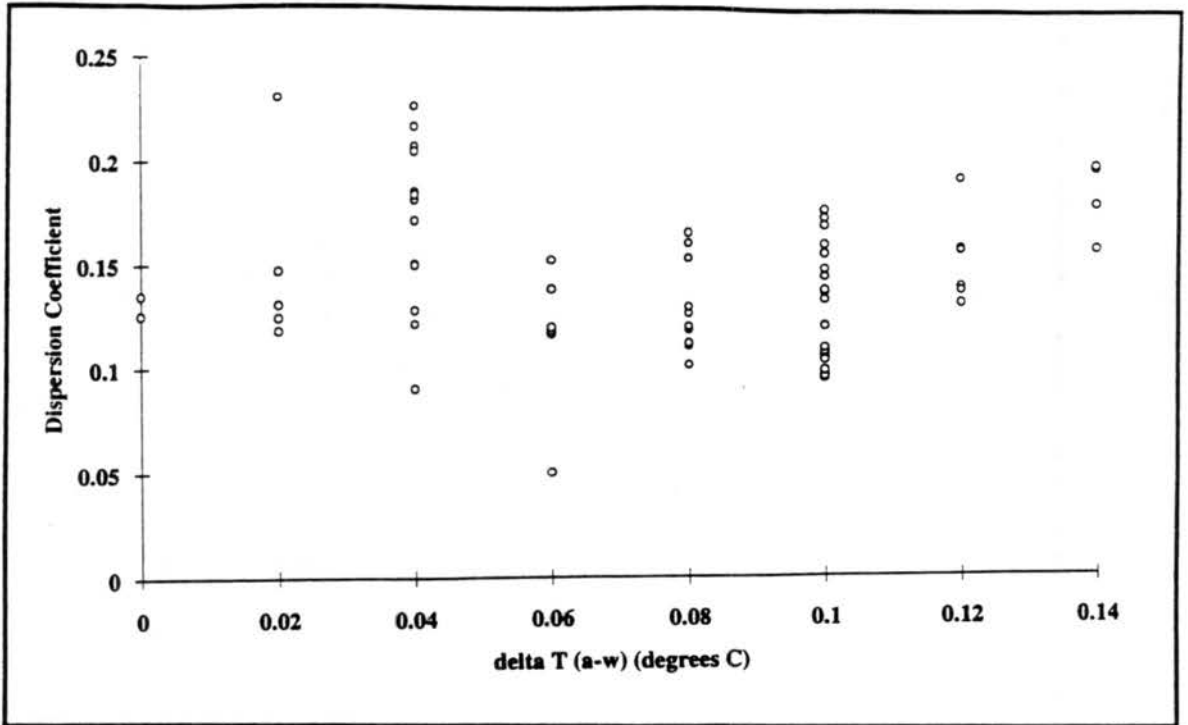


Figure 4.14a Dispersion Coefficient vs. ΔT (a-w) for 2.0 m s⁻¹.

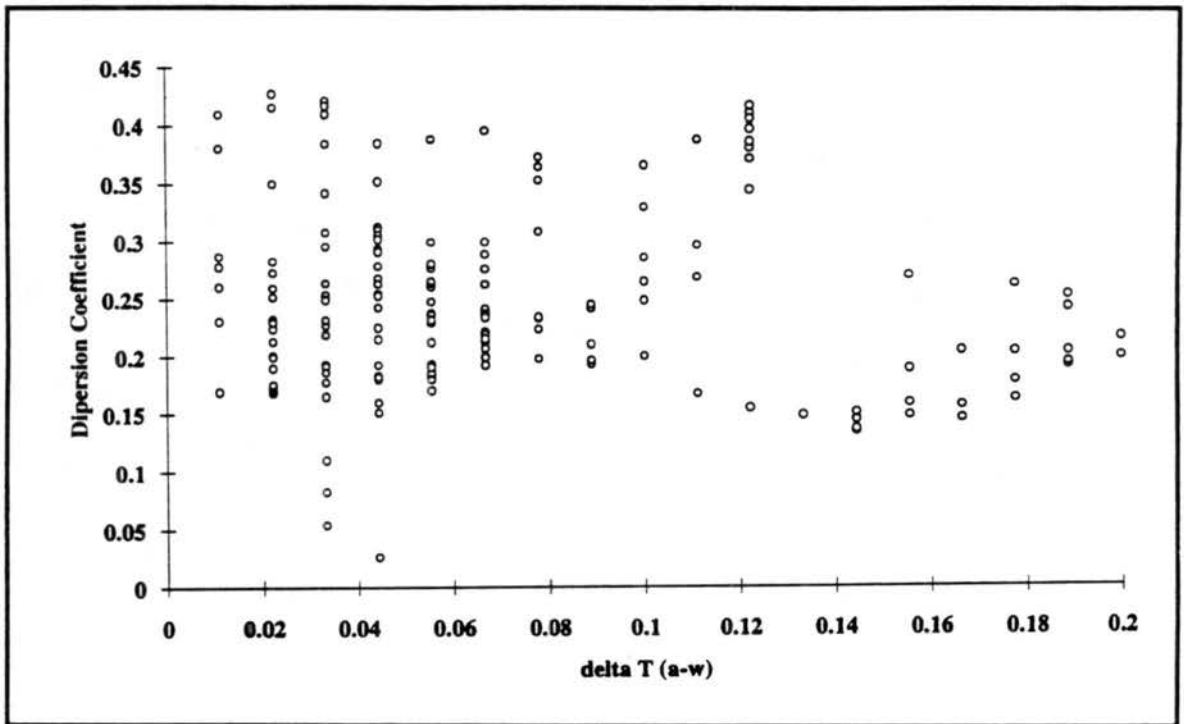


Figure 4.14b Dispersion Coefficient vs. ΔT (a-w) for 1.0 m s⁻¹.

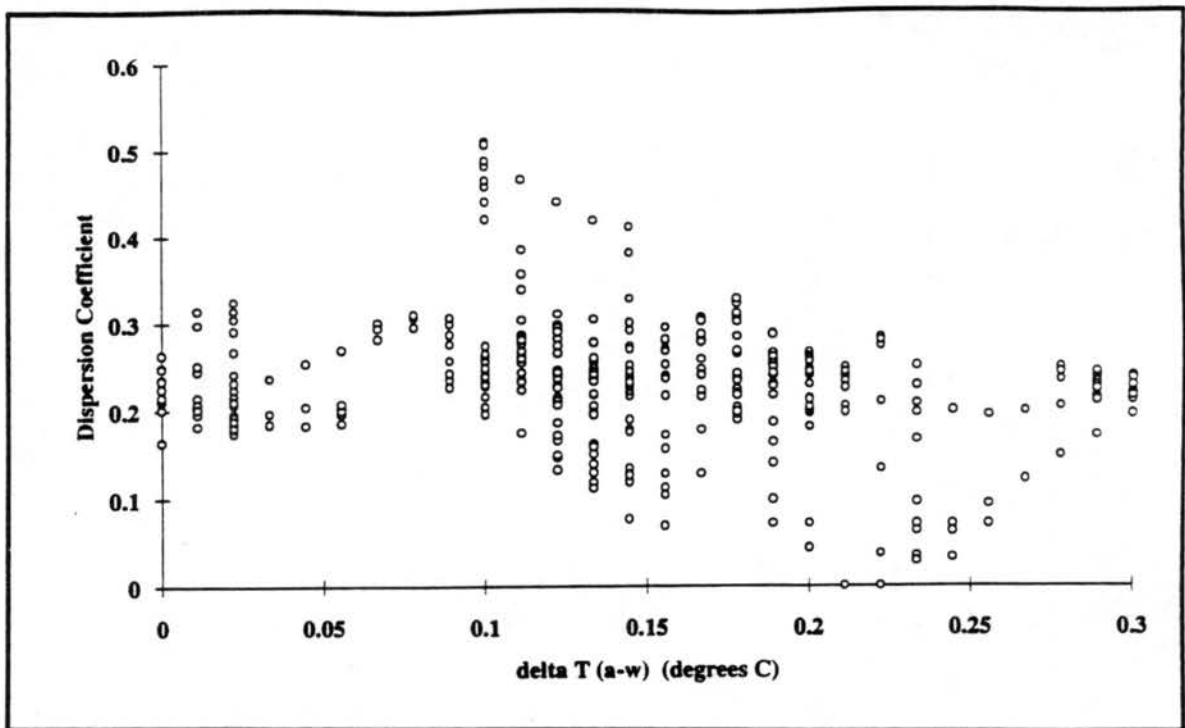


Figure 4.14c Dispersion Coefficient vs. ΔT (a-w) for 0.5 m s⁻¹.

be little to no correlation between dispersion coefficient and ΔT (air-wall), suggesting that the differences between wall and air temperature were not great enough to significantly influence the cloud droplet population. However, to eliminate the uncertainties described, steps are being taken to improve the wall control algorithm for future slow expansion rate studies.

4.4b Microphysics

Equations

The activation of CCN as cloud droplets is the underlying concern in this project. Activation can be affected not only by size of the CCN, but also by the number of CCN

available and the upward velocity of the rising parcel of air. The size of particle nucleated is determined by the parcel supersaturation. Rogers and Yau (1989) detail the equations that govern droplet nucleation by condensation, including the effect of a nonvolatile dissolved substance tending to lower the equilibrium vapor pressure of a liquid. The critical values of saturation ratio, S_c , is given by:

$$S_c = 1 + \sqrt{\frac{4a^3}{27b}} \quad (4.5)$$

where

$$a = 3.3 \times 10^{-5} / T \text{ (}^\circ\text{K)}$$

and

$$b = 3 i m_v M / 4 \pi \rho_L m_s$$

where i is the degree of ionic dissociation (3 was used for ammonium sulfate), m_v is the molecular weight of water, M is the mass of solute (in this case ammonium sulfate), ρ_L is the density water, and m_s is the molecular weight of the solute.

Figure 4.15 shows the calculated values for critical supersaturation (or saturation ratio) for ammonium sulfate as the solute. It can be seen that smaller CCN radii require greater values of supersaturation to activate as a cloud droplet.

Experimental Microphysics

Several quantities that describe the microphysical state of a cloud at any one time were diagnosed for this study. The mean droplet diameter, $\overline{D_d}$, is used to look at the growth of the cloud and is calculated using:

$$\overline{D}_d = \frac{\sum_D D_d * [N_d]}{\sum_{D_d} [N_d]} \quad (4.6)$$

where D_d is the diameter midpoint of each FSSP diameter bin and $[N_d]$ is the droplet concentration in each bin. Data associated with droplet distributions with mean diameters greater than approximately 15 μm were disregarded in this analysis, because the focus of the study was to look at nucleation and initial growth of cloud droplets. Also, once a droplet reaches a diameter greater than 15 μm , its terminal velocity becomes great enough to settle out of the chamber, thus causing irreconcilable inhomogeneities in the data.

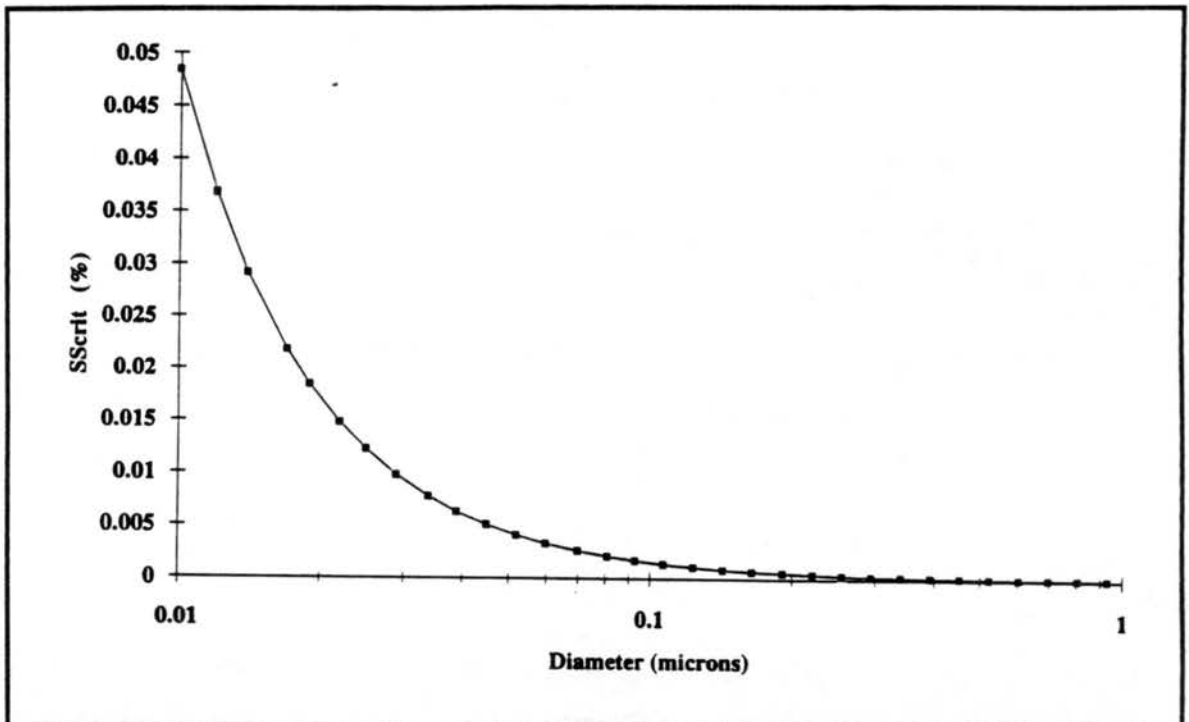


Figure 4.15 Critical Supersaturation of Ammonium Sulfate Particles as a Function of Diameter.

Another parameter used to describe a population of droplets is the dispersion of the droplet distribution, σ , which is the standard deviation of the droplet spectra normalized by the mean diameter of the distribution. The standard deviation is calculated by:

$$S = \sqrt{\sum (\overline{D}_d - D_d)^2} \quad (4.7)$$

where \overline{D}_d is the geometric mean diameter of the distribution and D_d is the actual measured diameter by size bin. Dividing (4.7) by (4.6) gives the dispersion coefficient, σ .

$$\sigma = S/\overline{D}_d \quad (4.8)$$

These relationships will be used extensively in the discussion of the microphysical properties exhibited in the experimental data.

Effects of Updraft Velocity on Cloud Microphysics

Parameters that prove useful for comparison of cloud microphysical data are nucleated aerosol fraction $[Nd]/[Na]$, mean diameter, dispersion coefficient and liquid water content (LWC). Table 4.5 shows average values as a function of updraft velocity.

Average values presented in Table 4.5 were calculated using:

$$\overline{F}_{\text{ups}} = \frac{\sum_i \overline{F}_{\text{exp}}}{N_{\text{ups}}} \quad (4.9)$$

where $\overline{F_{ups}}$ is the average of either nucleated aerosol fraction or dispersion coefficient microphysical quantity at either 0.5, 1.0, 2.0 m s⁻¹, i is all experiments conducted at that particular updraft velocity, $\overline{F_{exp}}$ is the average of all data from cloud base to the point in the experiment when the mean droplet diameter was 15 μ m for each experiment, and N_{ups} is the number of experiments at the particular updraft velocity.

One general trend evident in Table 4.5 is that increases in simulated updraft velocity correspond to increases in the nucleated aerosol fraction. In contrast, as updraft velocity increased, the dispersion coefficient decreased. The increase in nucleated aerosol fraction infers an increase in droplet number concentration, which supports Twomey's (1959) theoretical findings (see Table 2.1).

Table 4.5.
Microphysical Quantities Averaged by Updraft Velocity.

Exp Type	[Nd]/[Na]	Dispersion
2.0 m/s	0.83	0.21
1.0 m/s	0.39	0.24
0.5 m/s	0.24	0.26

DISPERSION COEFFICIENT

Theoretical considerations suggest that faster updraft velocities should produce narrower cloud droplet distributions, or smaller dispersion coefficients. As seen in Table 4.5, the dispersion coefficient (averaged over all 50 experiments) decreases by 12 to 13 %, as the updraft speed is doubled. For example, the average dispersion coefficient for a 1.0 m s⁻¹ expansion was 0.24 and for a 2.0 m s⁻¹ expansion was 0.21. This represents a decrease of 13% in the broadness of the droplet distribution. Also, the change in dispersion coefficient from an average 0.5 m s⁻¹ expansion to a 1.0 m s⁻¹ expansion is

12%. These results are similar to those observed by Fitzgerald (1972) in his modeling study of natural continental cumulus clouds. He predicted a decrease of 10 to 15 % with increasing updraft velocity. A coupling of his findings and the experimental data could suggest that as updraft velocity doubles the dispersion coefficient can decrease by 10 to 15 % regardless of cloud type.

NUCLEATED AEROSOL FRACTION

The experimental nucleated aerosol fraction trend observed in Table 4.5 is compared to ACPL model output and to results of modeling the activation of a bimodal aerosol distribution from Chuang and Penner (1990) in Table 4.6. The trend of the experimental data is similar to both ACPL model output and Chuang and Penner's results, but, the actual fraction of aerosol nucleated in the experiments is lower than predicted by either model. The average aerosol fraction nucleated in the experiments conducted at 2.0 m s^{-1} does appear to be reasonably close to that predicted by the ACPL

Table 4.6

Comparison of Seven Aerosol Distribution Type Average Experimental Nucleated Aerosol Fraction to ACPL Model Averages and Chuang and Penner Averages Delineated by Updraft Velocity.

Updraft Velocity (m s^{-1})	Aerosol Fraction Nucleated $[\text{Nd}]/[\text{Na}]$		
	Experimental	ACPL model	Chuang and Penner (1990)
0.5	0.24	0.70	0.80
1.0	0.39	0.87	0.90
2.0	0.83	0.91	n/a

model. However, these values include all seven aerosol distribution types. If the two high concentration type experiments are taken out of the average and handled separately, the lower concentration experiment aerosol fraction values become closer to those predicted by the ACPL model (see Table 4.7).

This trend in the higher concentration experiments may indicate that aerosol number loading in the higher concentration experiments affects aerosol fraction nucleated more than theoretical models predict.

Table 4.7

Comparison of Average Experimental Nucleated Aerosol Fraction to ACPL Model Averages and Chuang and Penner Averages Delineated by Aerosol Loading and Updraft Velocity.

Updraft Velocity (m s ⁻¹)	Aerosol Fraction Nucleated [Nd]/[Na] less than 500 particles cm ⁻³ / more than 500 particles cm ⁻³ aerosol loading		
	Experimental	ACPL model	Chuang and Penner (1990)
0.5	0.68 / 0.30	0.77 / 0.43	1.00 / 0.60
1.0	0.92 / 0.45	0.88 / 0.84	1.00 / 0.80
2.0	1.04 / 0.77	0.91 / 0.92	n/a

MEAN DIAMETER AND LIQUID WATER CONTENT

Figure 4.16 shows that experimental mean droplet diameter averaged over all aerosol number loading increases with increasing updraft velocity. The averages were calculated using the following equation:

$$\overline{F}_{\text{ups}} = \frac{\sum_i F_{\text{time}}}{N_{\text{ups}}} \quad (4.10)$$

where $\overline{F}_{\text{ups}}$ is the average of either mean droplet diameter or liquid water content at either 0.5, 1.0, 2.0 m s⁻¹, i is all experiments conducted at that particular updraft velocity, F_{time} is the value of either quantity at either 25, 50, 100, or 200 seconds from simulated cloud point for each experiment, and N_{ups} is the number of experiments at the particular updraft velocity.

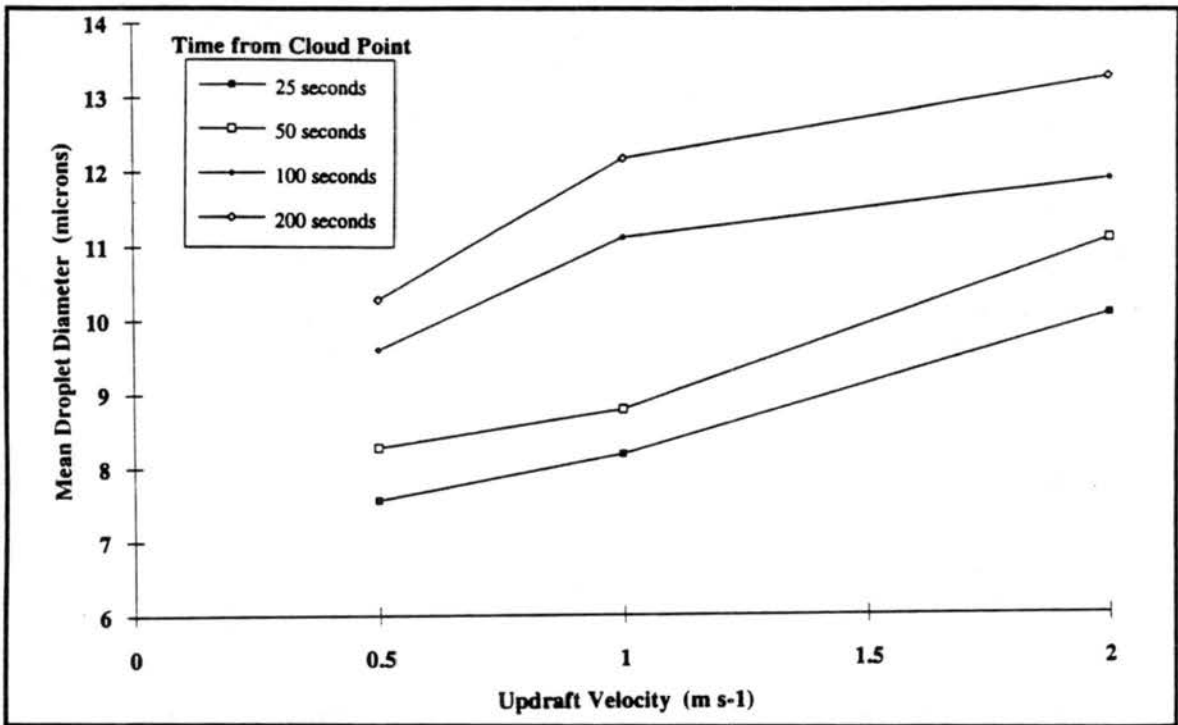


Figure 4.16 Trends in Experimental Nucleated Aerosol Fraction with Updraft Velocity. Averages Representative of Several Times from Cloud Point.

This averaged information in Figure 4.16 is represented for several times from cloud point. The increasing trend in mean diameter is expected. Pruppacher and Klett

(1978) explain that faster updraft velocities create larger maximum supersaturation values, which in turn means that there is more water vapor readily available to cloud droplets. This increase of readily available water allows for the more rapid growth of the mean diameter of a cloud droplet distribution.

The observations shown in Figure 4.17 indicate that there is also generally an increase in liquid water content with an increase in updraft velocity. The values of liquid water were calculated using the mean droplet diameter. So, it is logical that the trend in liquid water content follows that of mean diameter. It appears that liquid water increases quickly from 100 seconds into the simulated cloud to 200 seconds into the cloud.

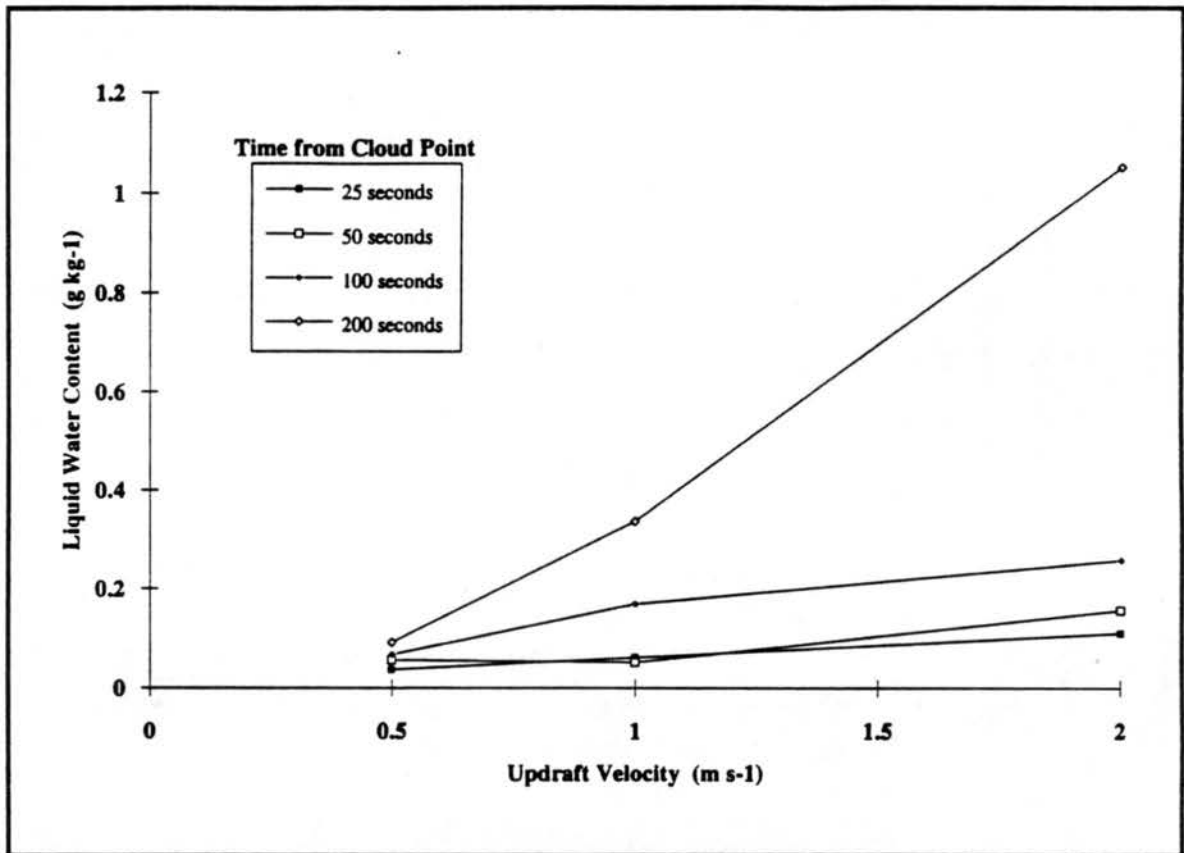


Figure 4.17 Trends in Liquid Water Content with Increasing Updraft Velocity. Averages Represent Several Times from Cloud Point.

Effect of Aerosol Number Loading on Cloud Microphysics

Table 4.8 provides mean data averaged over all updraft velocities and grouped by aerosol distribution type. These averaged were computed in a similar manner to those calculated for Table 4.5. The equation used was:

$$\overline{F_{adt}} = \frac{\sum_j \overline{F_{exp}}}{N_{adt}} \quad (4.11)$$

where $\overline{F_{adt}}$ is the average values of the nucleated aerosol fraction and dispersion coefficient (experiments were grouped by aerosol distribution type before averaging), j is all experiments when that particular aerosol distribution was injected, and N_{adt} is the number of experiments conducted using that particular aerosol distribution type. $\overline{F_{exp}}$ is the same as described for Table 4.5.

NUCLEATED AEROSOL FRACTION

Comparison of droplet number concentrations nucleated can be better done when aerosol fraction nucleated is considered. The maximum value for aerosol fraction nucleated in the theoretical ACPL model is 1.0, which occurs if 100 % of the aerosol injected are nucleated. Nucleated aerosol fraction data sets averaged over all updraft velocities and grouped by aerosol distribution type are shown in Table 4.8. Both averaged experimental data and averaged ACPL model output are included in this table. The average actual concentrations of each aerosol distribution type provided in Table 4.1 may be used to infer changes in aerosol loading.

As discussed earlier in this chapter, increasing total aerosol loading results in a decrease in aerosol fraction nucleated. However, experiments with aerosol loading less than 500 particles cm^{-3} generally appear to have a higher nucleated aerosol fraction than predicted by the ACPL model. In contrast, the average experimental nucleated fraction for the higher concentration experiments appears to be lower than predicted by the model.

Table 4.8.
Cloud Microphysical Data Grouped by Aerosol Distribution Type (defined in Table 4.1) and Averaged Over All Updraft Velocities.

Exp Type	Aer. Load (cm^{-3})	[Nd]/[Na]		Dispersion	
		Exp.	ACPL	Exp.	ACPL
50 SP	70	1.10	0.92	0.24	0.06
50 LP	50	1.03	0.95	0.20	0.03
100 LP	150	0.99	0.92	0.22	0.03
2 spike	200	0.80	0.85	0.25	0.09
spk& poly	300	0.74	0.65	0.24	0.13
high conc.	1000	0.42	0.73	0.23	0.04
polydisp.	1000	0.65	n/a	0.21	n/a

The FSSP system was studied to determine if it is biasing droplet concentration (see Appendix B). There is some support that the FSSP sampling system may be over estimating the droplet concentration. This is more clearly evident in the low droplet concentrations experiments, where nucleated aerosol fraction exceeded one for several experiments.

Another possible reason for the differences between experiment observations and model output is that the slight inhomogeneities observed in the chamber during

expansion may be enough to cause areas of enhanced droplet concentration. Borrmann et al., (1993) presents recent findings that indicate droplets in natural clouds are not as evenly spaced as theory predicts. Measurements by Politovich and Vali (1983), Hudson and Frisbie (1991) and Hegg et al (1991) also suggested that the spatial variability of aerosol may be important. As a result, there should be pockets of enhanced concentrations occurring in the atmosphere that are not predicted by theory.

DISPERSION COEFFICIENT

Comparison of number concentration to the dispersion coefficient calculated from the FSSP data shows that at droplet concentrations less than 100 droplets cm^{-3} , the dispersion coefficient becomes much more variable. Above 100 droplets cm^{-3} , the dispersion coefficients seem to remain near a particular value. Figure 4.18 shows this trend for Experiment 23, which is a monodisperse experiment that should have a relatively constant dispersion coefficient. In general, this trend appears in all experiments. The increased variability in dispersion coefficient supports the idea that there may be a problem in the counting statistics of the FSSP, because number concentration is used in the calculation of dispersion coefficient. If the concentration information is very uncertain at low droplet concentration, it may affect dispersion coefficient calculations.

Comparison of dispersion coefficient by aerosol number loading does not indicate any particular trends. When averaged by distribution type for all updraft velocities (Table 4.8), the raw FSSP dispersion coefficient appears to range from around 0.20 or 0.25, whereas the ACPL model predicts average dispersions from 0.03 to 0.13. As

described in section 4.3c, the FSSP may have broadened the experimental dispersion coefficients by as much as 0.10. Most of the dispersion coefficients predicted by the ACPL model are smaller than the possible broadening effect and differences in dispersion coefficient may not be detected by the FSSP. This is one possible reason for the apparent lack of change in the experimental dispersion coefficient values.

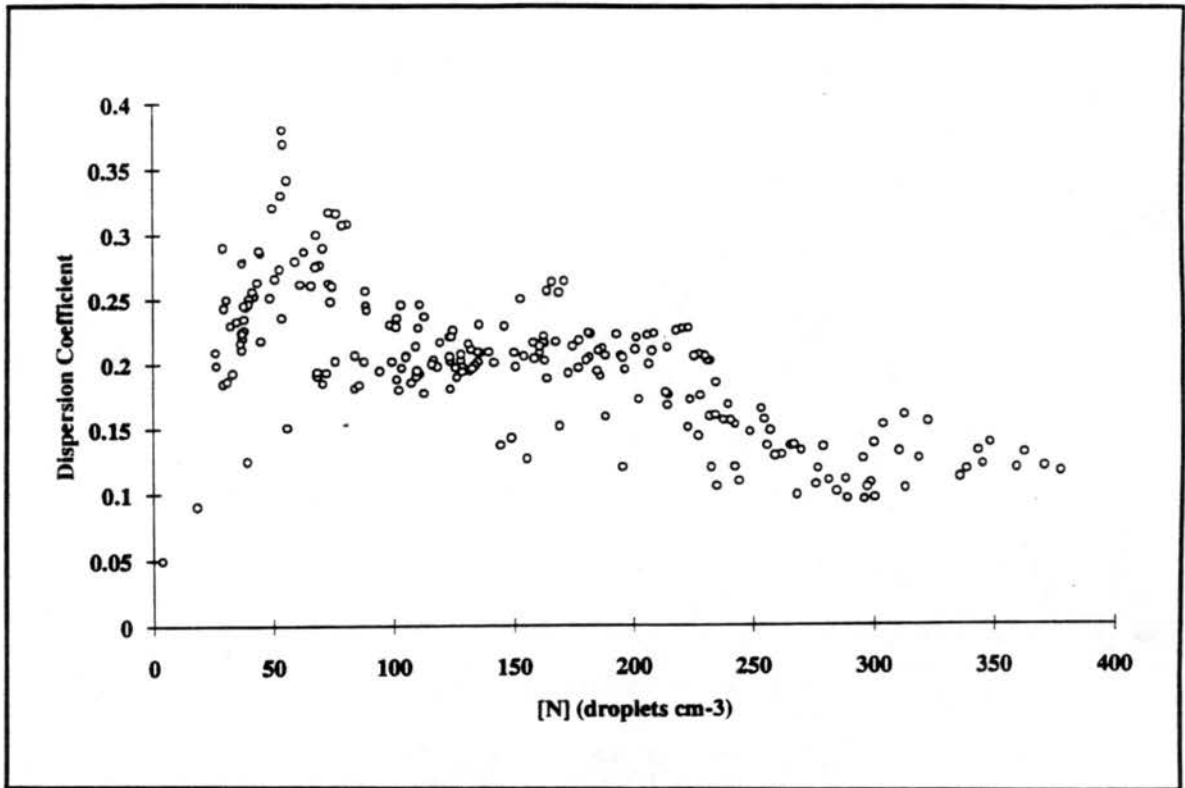


Figure 4.18 Dispersion Coefficient vs. Droplet Number Concentration for Experiment 23 (100 Large particle Experiment at 2.0 m s⁻¹) for data taken from cloud base to mean droplet diameter of 12 μm .

MEAN DIAMETER

As aerosol number concentration, and thus droplet concentration, increases in a cloud of a constant liquid water content, the mean diameter of the droplets is expected to

decrease. In Figure 4.19, the decreasing trend in mean droplet diameter with increasing aerosol loading is evident. Values for this figure were calculated using:

$$\overline{F}_{\text{ani}} = \frac{\sum_j \overline{F}_{\text{adt}}}{N_{\text{ani}}} \quad (4.12)$$

where $\overline{F}_{\text{ani}}$ is the average values of the mean droplet diameter when experiments were grouped by aerosol distribution type before averaging, j is all experiments when that particular aerosol distribution was injected, and N_{ani} is the number of aerosol distribution types that fall between the particular aerosol number loading. $\overline{F}_{\text{adt}}$ is the same as described for Table 4.8.

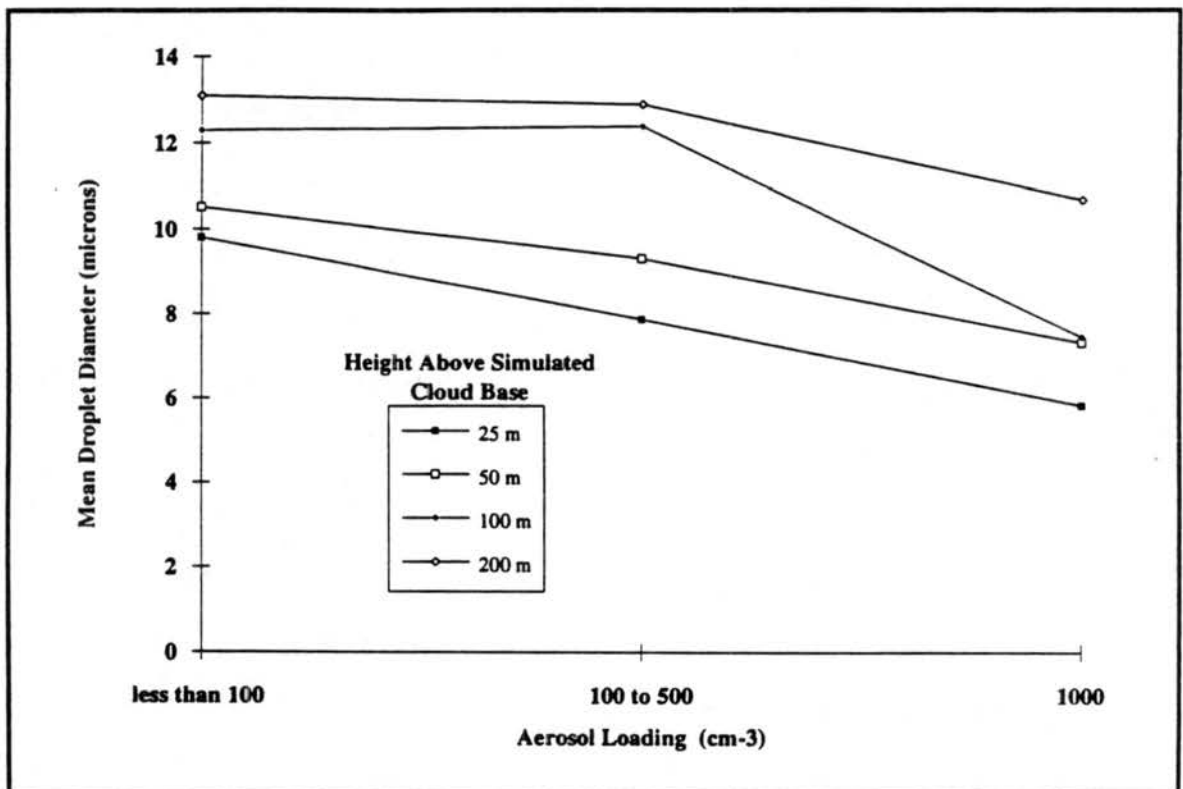


Figure 4.19 Trends in Mean Droplet Diameter with Increasing Aerosol Number Loading. Averaged Delineated by Height Above Simulated Cloud Base.

From Figure 4.19, there appears to be less difference in mean diameter the further up the parcel is from the simulated cloud base. The difference between mean droplet diameter for aerosol loading less than 500 particles cm^{-3} appears to be small. However, when aerosol number loading is increased to greater than 500 particles cm^{-3} , there is still an approximate 2 μm difference between aerosol loading less than 500 particles cm^{-3} and greater than 1000 particles cm^{-3} . This may suggest that there is very little impact on mean droplet diameter, and possibly cloud optical depth, when aerosol loading is increased but remains less than 500 particles cm^{-3} .

4.4c Case Studies

The analysis presented in section 4.4b was based on averaged data. There is much to be learned from analyzing specific cases also. Table 4.11 lists the specific experiments that will be discussed in this case study section. The one second data used in this section have been smoothed using a nine second running average and droplet number concentrations have been corrected for the VAR/sample volume relationship described in Appendix B. These data were also used to initialize a ACPL model run for each experiment listed below.

First, general comparisons of the repeatability of the most simple case, a monodisperse experiment, will be discussed using Experiments 22, 23, and 49, and the ACPL model results will be used to show agreement with theory. The remaining experiments listed in Table 4.11 will be used to point out the differences between the behavior of clouds at different updraft velocities and initial aerosol number concentrations.

The monodisperse aerosol injected into the chamber represented the most simple case possible for comparison to theory. For a single spike of CCN, all aerosol should nucleate and the cloud droplet distribution should be very monodisperse. Although several aerosol distribution types were monodisperse, the 100 large particle type experiments, represented by Experiments 22, 23, and 49, were used to look at the agreement to theory and the repeatability of experiments. All three experiments were performed at a 2.0 m s^{-1} expansion rate and approximately 150 big particles (see Table 4.1 for clarification of big particles) were initially injected. Table 4.11 indicates that the initial conditions of the three experiments (other than actual aerosol loading) are reasonably close.

Table 4.11
Experiment Initial Conditions for Case Studies.

Exp #	Aerosol Distribution Type	Updraft Speed (m s^{-1})	Initial Pressure (mb)	Initial Temp ($^{\circ}\text{C}$)	Initial Dewpoint Temp ($^{\circ}\text{C}$)	Initial Aerosol Conc. ($\# \text{ cm}^{-3}$)
22	100 LP	2.0	844	20.0	15.8	205
23	100 LP	2.0	840	20.3	16.0	220
49	100 LP	2.0	844	19.8	16.0	100
47	100 LP	1.0	848	19.7	15.9	120
43	100 LP	0.5	844	19.6	16.0	120
37	2 spike	2.0	839	19.9	15.9	210
29	spike & polydisperse	2.0	832	19.9	15.4	210
45	polydisperse	2.0	849	20.1	16.4	1100

Agreement with Adiabatic Conditions

Figure 4.20 shows the average experimental θ trace (solid line) for Experiment 22, 23 and 49 (all 100 big particles expanded at 2.0 m s^{-1}) along with the ACPL θ trace (dashed line), with individual experiment data represented by thin solid lines. The agreement to adiabatic conditions appears to be similar to that discussed about all 2.0 m s^{-1} experiments in section 4.4a. Oscillations occur in θ during the dry adiabatic expansion due to temperature control problems. However, by the time a cloud forms, the

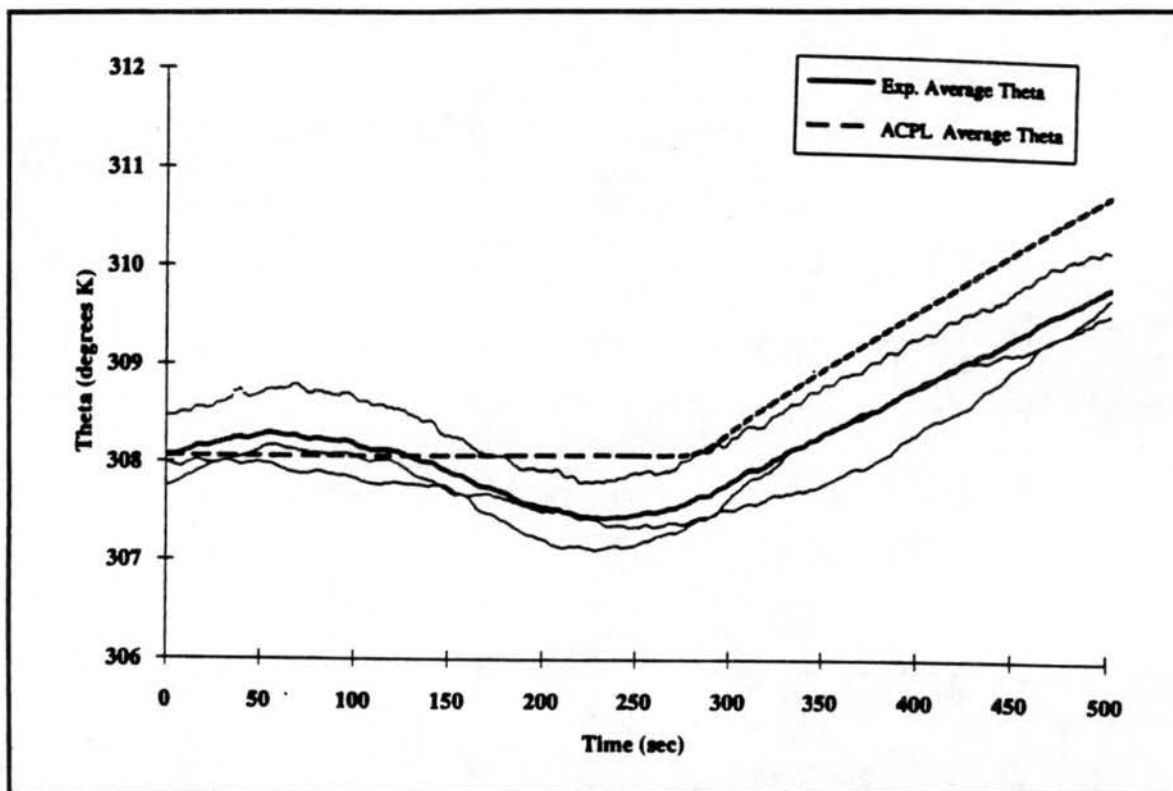


Figure 4.20 Comparison of 100 Large particle Experiment at 2.0 m s^{-1} Averaged θ (solid line) to ACPL Averaged θ (dashed line). Individual Experiments Represented by Thin Lines.

temperature is fairly well controlled. As discussed earlier, the experimental cloud may form after the ACPL predicts because of the added heat introduced during the θ oscillations. Whenever possible, comparisons of experimental data to model from this point forward will be done using time from cloud base to accommodate this effect.

NUCLEATED AEROSOL FRACTION

Figure 4.21 shows the nucleated aerosol fraction (droplet number concentration normalized by injected aerosol concentration) as a function of time from cloud base. The open symbols represent each individual experiment. After approximately the first 100 seconds of the experiments, it appears that the number concentration rapidly decreases. This is due to droplet sedimentation out of the chamber.

Repeatability of experiments appears to be fair to good. One of the limiting factors of repeatability is wall temperature control problems. For example, the open triangles (Experiment 49) show a concentration time history with lower nucleated aerosol fraction than the average nucleated aerosol fraction for the first 75 seconds of the cloud. There are indications that wall temperature at cloud point was too warm for the prescribed adiabatic ascent rate and may have slowed down the rate of saturation, thus influencing the droplet time history for that experiment. The "periodicity" of the individual experiment nucleated aerosol fractions may be attributed with fluctuation in supersaturation within the chamber related to wall temperature control. Other effects of the wall control problem will be pointed out later.

As can be seen in Figure 4.21, the aerosol fraction nucleated at the beginning of the cloud was on average 50% greater than the actual concentration injected into the chamber. This discrepancy is too large to be explained by uncertainties alone. Some of

the discrepancy may be explained by the uncertain concentration profile within the sample flow of the FSSP. Appendix B provides a complete discussion of this possibility. Also, sampling statistics for concentrations less than 500 droplets cm^{-3} may have influenced the reported droplet concentration. This over-nucleation seems to occur at the beginning of most clouds, even for the higher concentration, more polydisperse experiments. For example, comparison of the nucleated aerosol fraction measured in Experiment 29 to its respective ACPL model results indicates a peak of 1.5 aerosol fraction nucleated, but then falls off and oscillates about an aerosol fraction of 0.80. The analysis of these nucleated aerosol fraction discrepancies has illuminated the need to understand the FSSP sampling system better and work is continuing on improving the system.

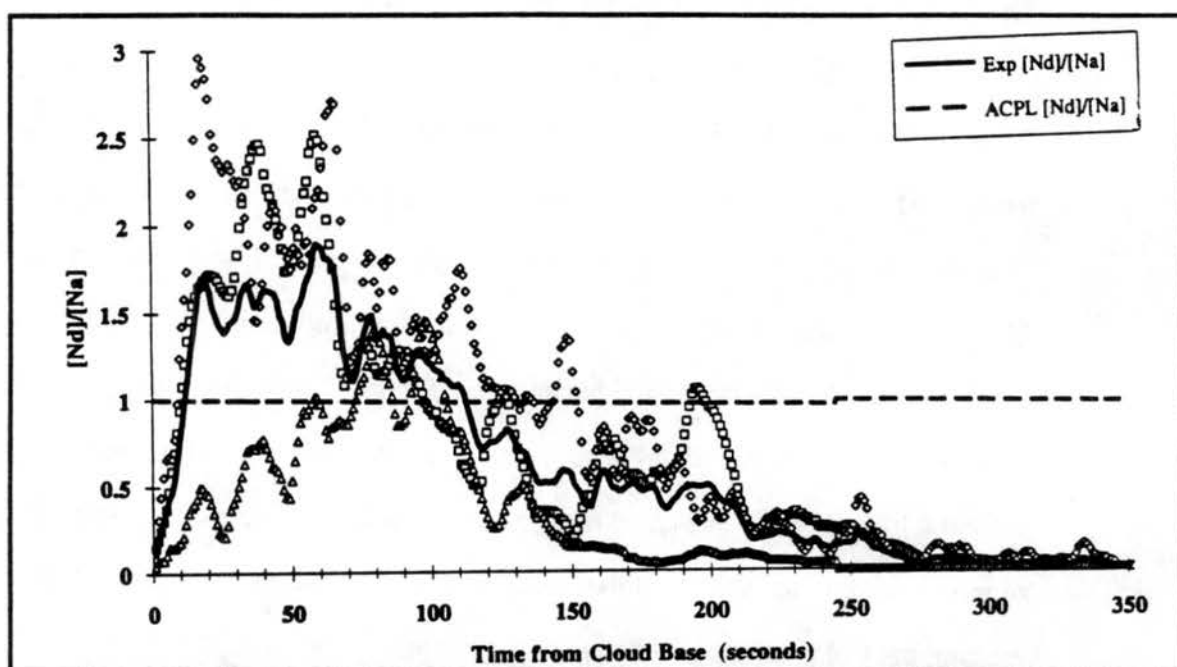


Figure 4.21 Comparison of Average Experimental (solid) to Average ACPL (dashed) Nucleated Aerosol Fraction for 100 Large particle Experiments at 2.0 m s^{-1} . Individual Experiments represented by open symbols: Experiment 22 (squares), Experiment 23 (diamonds), and Experiment 49 (triangles)

Figure 4.21 shows a comparison of experimental nucleated aerosol fraction to ACPL model output for a 100 large particle experiment at 1.0 m s^{-1} (Experiment 47). Comparison of this figure to Figure 4.22 highlights that aerosol fraction nucleated is significantly reduced at the slower updraft velocity. Figure 4.23 depicts the nucleated aerosol fraction at 0.5 m s^{-1} (Experiment 43). Not only is observed nucleated aerosol fraction reduced, which is similar to observations made by Hindman et al., (1989), but the data appears to be significantly more variable.

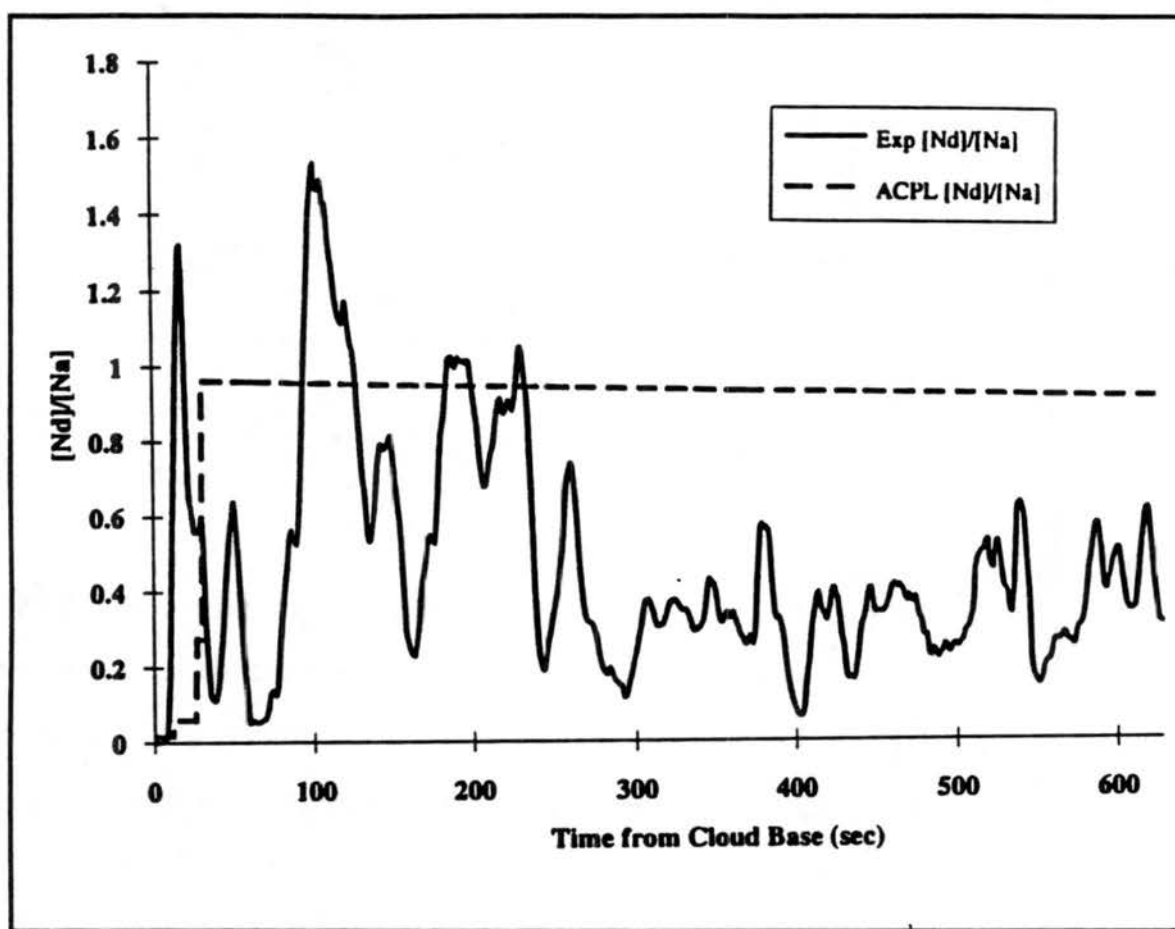


Figure 4.22 Comparison of Experimental (solid line) to ACPL (dashed line) Nucleated Aerosol Fraction for Experiment 47 (100 Large particle Experiment at 1.0 m s^{-1}).

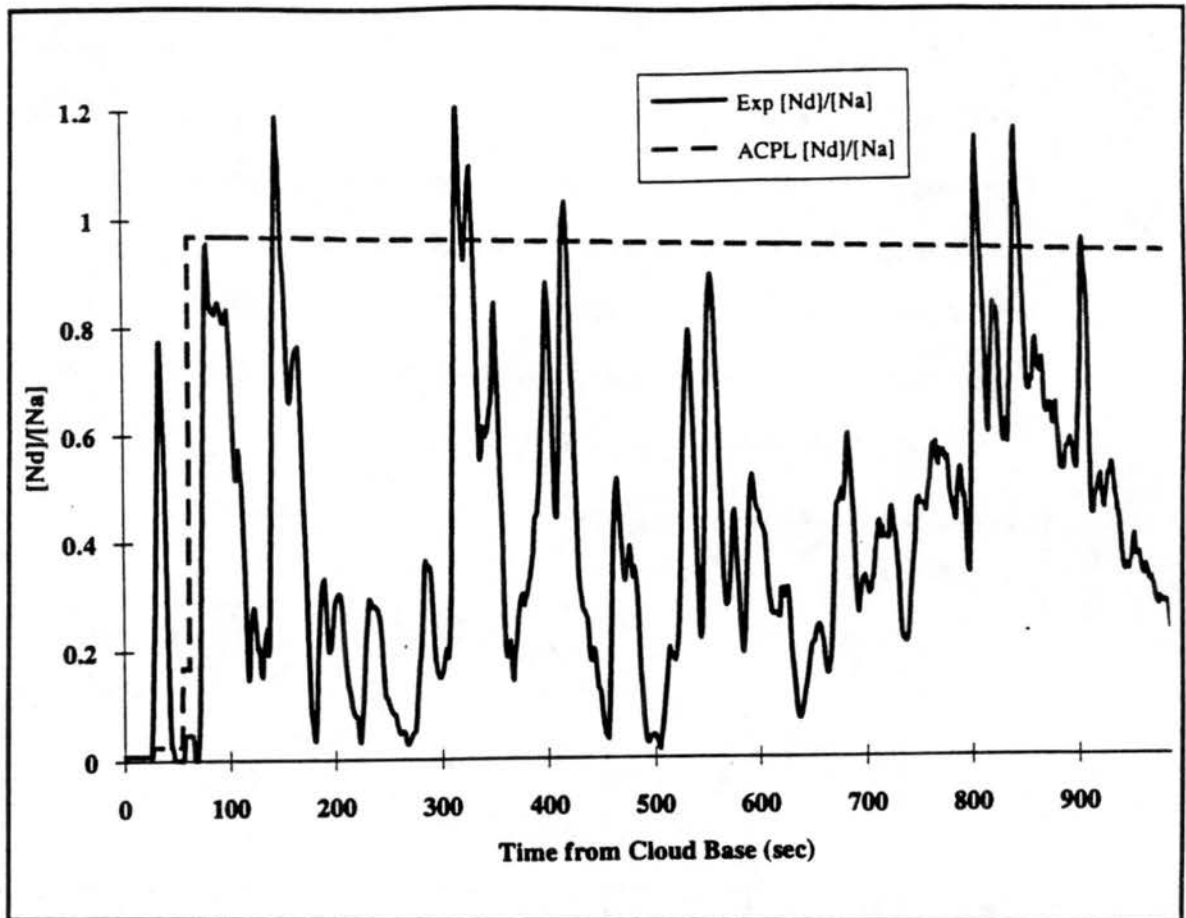


Figure 4.23 Comparison of Experimental (solid line) to ACPL (dashed line) Nucleated Aerosol Fraction for Experiment 43 (100 Large particle Experiment at 0.5 m s^{-1})

The highly variable nature of the slow expansion experiments may be a result of inhomogeneities induced by wall effects or the non-adiabatic conditions indicated in Figure 4.13c. The residence time of the air at any particular state (temperature and pressure) may be long enough to allow for thermal gradients to set up, thus causing turbulence that propagates out from the wall. Significant "patchiness" was observed in the cloud while 0.5 m s^{-1} experiments were conducted. This patchiness appears to be represented in the nucleated aerosol fraction data taken at this low updraft velocity, and may indicate that the lower bound of updraft velocity for experiment may be between 0.5 m s^{-1} and 1.0 m s^{-1} .

MEAN DIAMETER

A composite plot for 100 big particles at 2 m s^{-1} updraft velocity of mean diameter of the droplet distribution is shown in Figure 4.24. The average mean diameter for the three experiments (solid line) appears to be in very good agreement with the average mean diameter calculated by the ACPL model (dashed line). It should be noted that the FSSP does not detect droplets until they are larger than $2.0 \mu\text{m}$. For comparison, ACPL data was filtered to remove droplet sizes smaller than $2.0 \mu\text{m}$. Variations in the droplet growth rate about the ACPL model results for the various experiments (open symbols) can be attributed to control of the supersaturation. Experiment 23 is used to discuss this possibility.

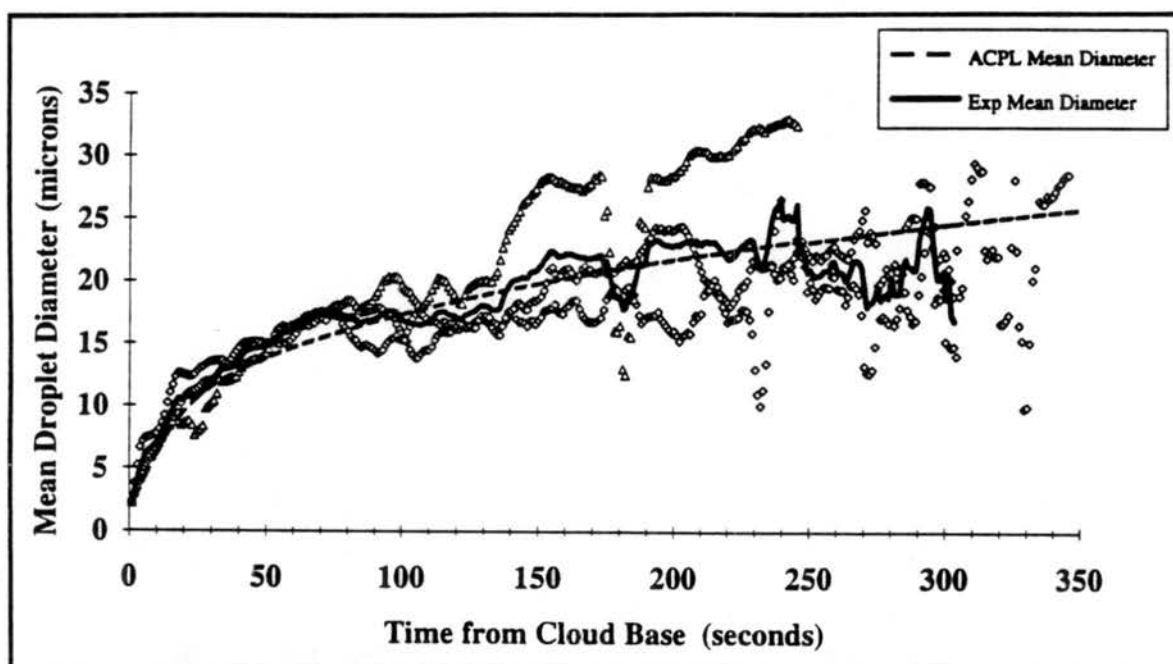


Figure 4.24 Comparison of Experimental (solid line) to ACPL (dashed line) Mean Droplet Diameter for 100 Large particle Experiment at 2.0 m s^{-1} . Individual Experiments Represented by Open Symbols: Experiment 22 (squares), Experiment 23 (diamonds), Experiment 49 (triangles).

Figure 4.25 indicates the program temperature changes in slope at approximately 280 seconds into the experiment, which indicates where temperature control changed from controlling at the dry adiabatic lapse rate, described by (4.2) to controlling at a moist adiabatic lapse rate, described by (4.3). This change of lapse rate should ideally come at cloud point. However, at the point the cloud forms (approximately 250 seconds), the air temperature trace indicates that the air continued cooling at the dry adiabatic lapse rate (the slope is very similar to the program pressure slope). The "insensitivity" of the wall temperature control can be attributed to two things; specification of a initial dewpoint temperature and overcompensation for expected diabatic effects.

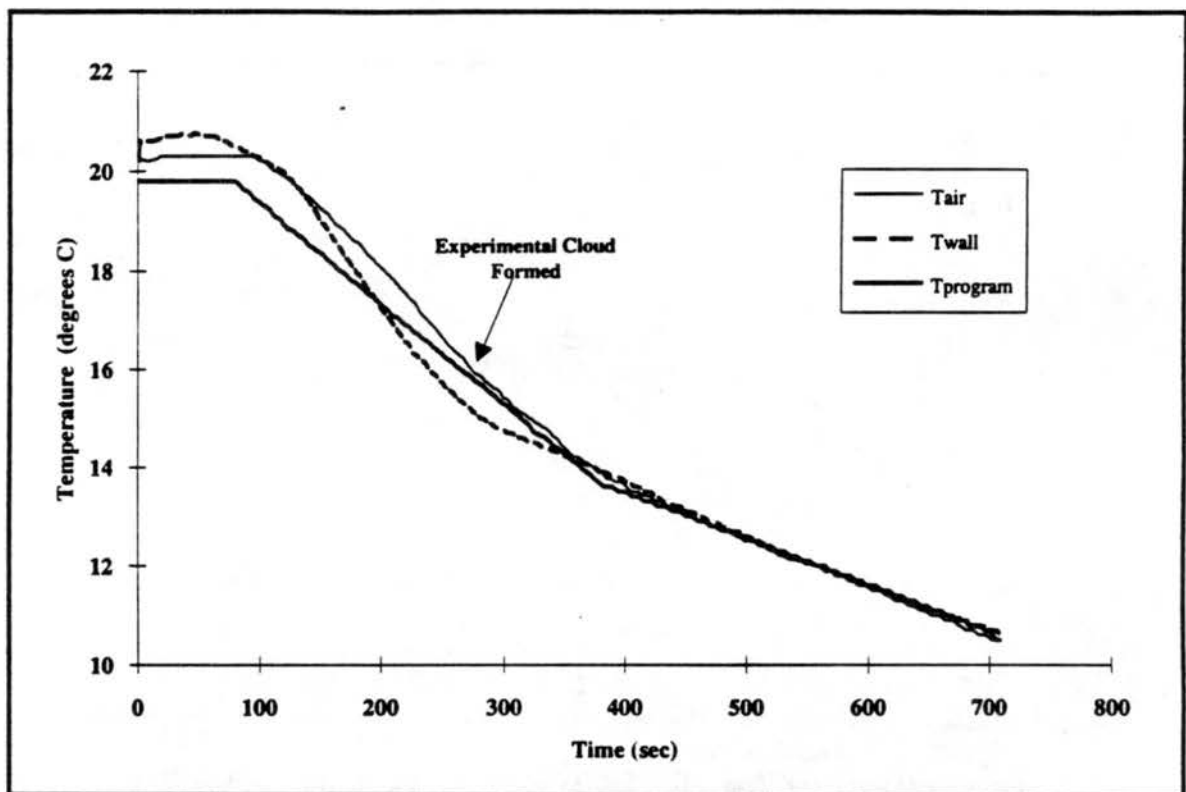


Figure 4.25 Air (thin line), Wall (dashed line) and Program (thick line) Temperature for Experiment 23.

Agreement in the slope of the program temperature and experimental air temperature for the first 100 seconds of the cloud (as shown in Figure 4.25) suggests the air in the chamber is saturating at the dry adiabatic lapse rate for the first 100 seconds of the cloud. The experimental RH shown in Figure 4.26 continues to have the same slope as the ACPL model predicted RH for at least 100 seconds after the experimental cloud forms. This indicates that the chamber air (thick solid line) is, in fact, saturating at a dry adiabatic lapse for the first 100 seconds of the cloud.

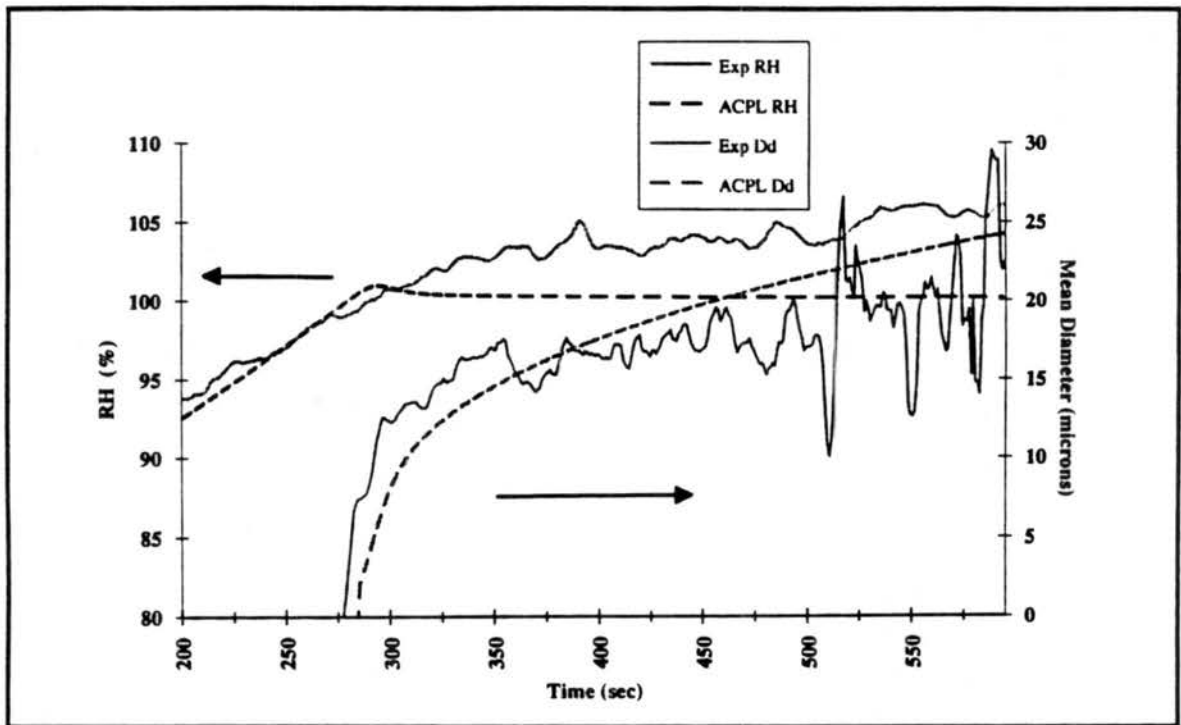


Figure 4.26 Comparison of Experimental (solid line) and ACPL (dashed line) Relative Humidity and Mean Droplet Diameter for Experiment 23. Relative Humidity Values May Be Read Off of Left Axis and Mean Diameter Values May Be Read Off of Right Axis.

Cloud droplets grow more rapidly at higher supersaturations. As can be seen in Figure 4.26, the ACPL model reaches its peak supersaturation near cloud point and levels

off while the experimental saturation is still increasing. This suggests that the mean diameter of Experiment 23 should be increasing faster than that of the ACPL model run. Comparison of the two traces in Figure 4.26 supports this suggestion. The mean diameter measured in Experiment 23 at approximately 30 seconds into the cloud is close to 13 μm , whereas the ACPL predicted mean diameter is approximately 11 μm . To provide a more complete comparison, the ACPL model needs to be forced to continue saturating at the dry adiabatic lapse rate until the experimental lapse rate changes. This is possible, but requires considerably more input and will be done later, as described in the Future Work Chapter.

DISPERSION COEFFICIENT

The dispersion coefficient of the cloud droplet spectra is calculated using (4.7). A dispersion coefficient of 0.0 represents a perfectly monodisperse distribution and of 1.0 represents a broad polydisperse distribution with equal concentration of droplets in each diameter bin. Calibration tests indicate that the cloud chamber FSSP may broaden the measured dispersion coefficient by 0.10 to 0.15. For example, if the distribution was nearly monodisperse, with a dispersion of 0.01, the FSSP may measure 0.16. Or, if the actual dispersion is 0.15, the FSSP may measure the dispersion as 0.30 (see Appendix C).

Figure 4.27 compares the average model dispersion coefficient output (dashed line) for Experiments 22, 23 and 49 to the average measured experimental dispersion coefficient (solid line) of these three experiments. The model results show a rapid increase then sharp fall off in dispersion in the first 20 seconds of the cloud. This initial

broadness of the distribution occurs as each size particle reaches its critical supersaturation and nucleates.

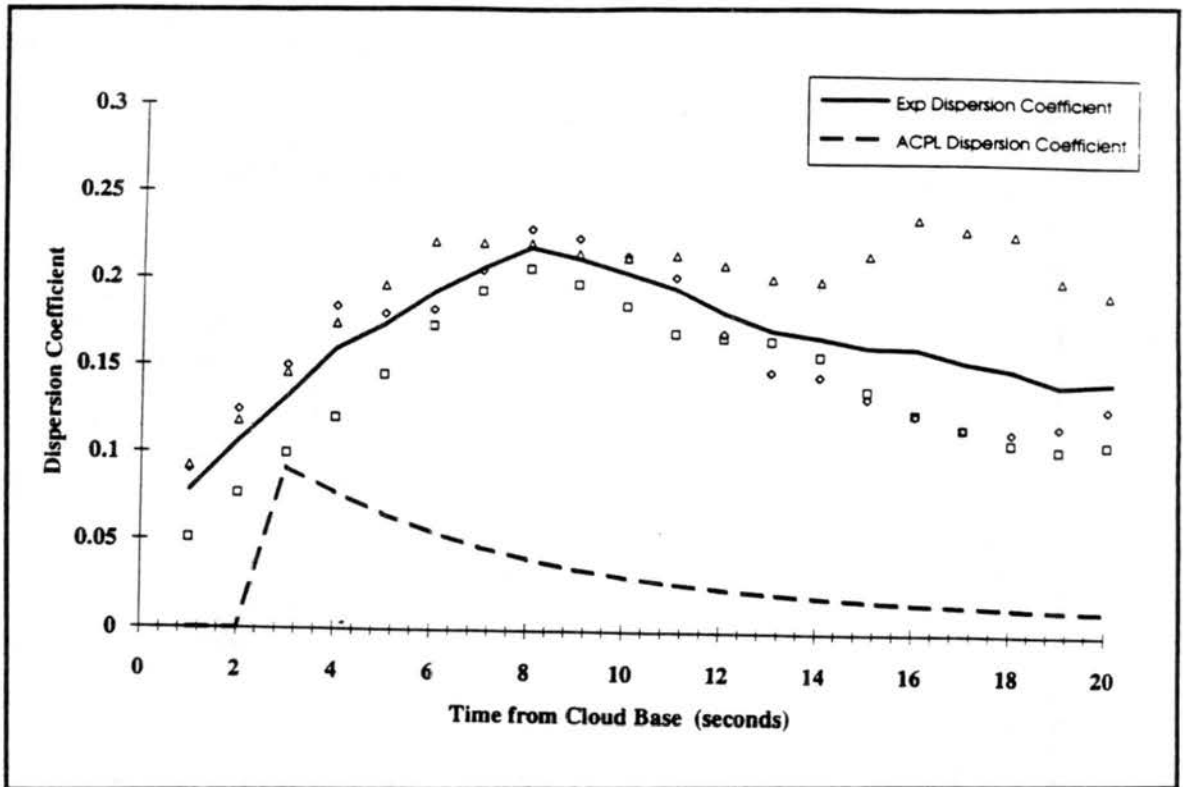


Figure 4.27 Comparison of Average Experimental (solid line) and Average ACPL (dashed) Dispersion Coefficient for 100 Large particle Experiment at 2.0 m s^{-1} . Individual Experiments are Represented by Open Symbols: Experiment 22 (squares), Experiment 23 (diamonds), and Experiment 49 (triangles).

Once nucleated, the droplets grow quickly and the distribution narrows. For a monodisperse distribution of CCN, there should be very little nucleation activity other than the primary burst. The model shows that the dispersion coefficient of a cloud formed on aerosol similar to the experimental monodisperse distribution should peak approximately 3 seconds into the cloud with a value of approximately 0.9. Figure 4.27 shows that this general trend was also seen in the experimental data. The experimental

data peaks at approximately 8 seconds into the cloud with a dispersion coefficient of 0.2 and drops off in a similar manner to the model output.

The continual nucleation of small particles in a polydisperse aerosol distribution causes the dispersion coefficient to remain at fairly high values (0.2 to 0.5) after initial nucleation. Figure 4.28 shows a comparison between Experiment 45, a polydisperse aerosol type experiment conducted at 2.0 m s^{-1} , to the corresponding ACPL model

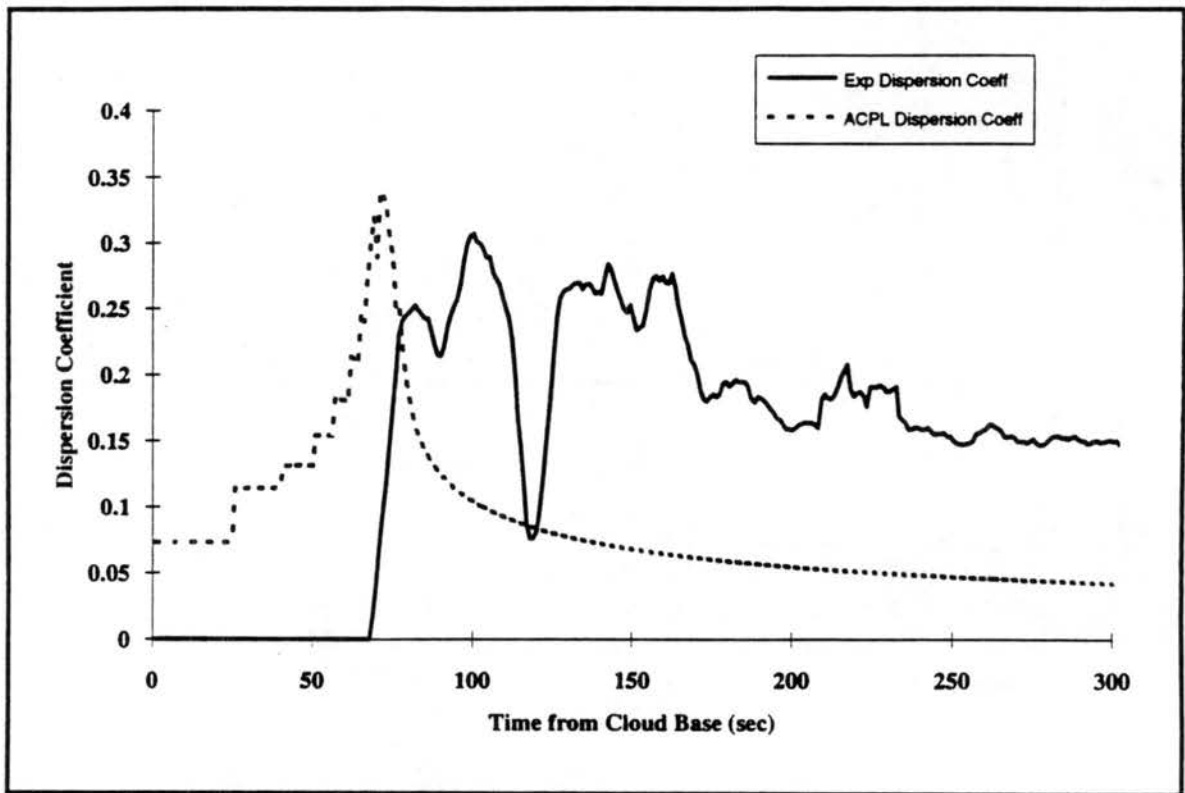


Figure 4.28 Comparison of Experimental (solid line) to ACPL (dashed line) Dispersion Coefficient for Experiment 45 (Polydisperse Experiment at 2.0 m s^{-1})

output. Both the experimental data (solid line) and the ACPL model data (dashed line) show a rapid increase in dispersion coefficient in the first minute of the cloud and then a slow decrease in the coefficient as the cloud ages.

After approximately 200 seconds, both ACPL and experimental dispersion coefficients appear to decrease at approximately the same rate. An offset of 0.15 in the ACPL dispersion coefficient from the ACPL dispersion coefficient is evident. This lends support to the idea that the dispersion coefficients measured by the FSSP may be biased by 0.10 to 0.15.

One other interesting feature in Figure 4.28 is the "structure" of the dispersion coefficient trace of the ACPL model. This structure is not evident in the experimental data. Limitations induced by the lower boundary of the FSSP range may be the cause of this lack of "structure".

Ranges 2 and 3 of the FSSP provide reasonable resolution in the size range necessary to look at nucleation and initial growth (0.5 μm to 5 μm). However, bin structure of the FSSP is less well defined in these ranges. Also, the mean droplet diameter moves out of these ranges quickly. Therefore, to capture more defined cloud droplet distribution information would require rapid changes in FSSP ranges during critical phases of nucleation and cloud growth. For this reason, measurements were taken using Range 1, which has a minimum diameter measurement of 2 μm . To make comparisons between model output and experimental data more simple, the ACPL model data presented in Figure 4.29 were passed through a filter that throws out diameters less than 2 μm . Dispersion coefficient values were then calculated using the revised ACPL droplet distribution. Figure 4.29 shows the same experimental data shown in Figure 4.28 compare to the filtered ACPL dispersion coefficient data. The filtering process made comparison more easy, but also pointed out that much of the interesting structure of the dispersion coefficient traces, especially for experiments using the polydisperse CCN, occurred while the droplets were less than 2 μm .

Another example of this can be seen in Figure 4.30, which depicts the experimental data for Experiment 37 accompanied by the model dispersion coefficient for both with and without the 2 μm filter applied to the model data. The primary structure of the model droplet dispersion is seen in the dispersion trace without filter (light dashed line) in the first 40 seconds of the cloud. This structure is lost when the 2 μm filter is applied (dark dashed line). Similar losses in model dispersion coefficient structure were seen for all types of initial aerosol distribution types. Comparison of experimental data (solid line) to model output indicates that the filtered data is a good estimate for the experimental data, confirming FSSP limits may be partially responsible for the differences between experimental dispersion coefficient and ACPL dispersion coefficient. A detector for droplets below 2 μm is needed if model predictions for nucleation and initial growth of droplets are to be compared with experimental results.

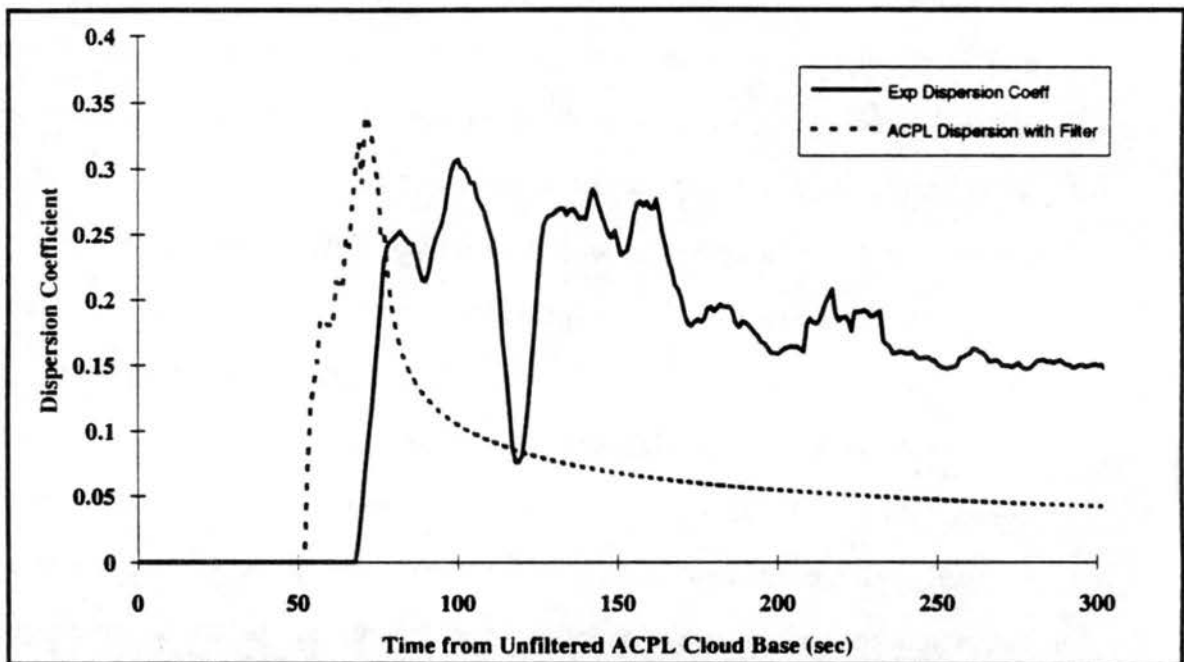


Figure 4.28 Comparison of Experimental (solid line) to Filtered ACPL (dashed line) Dispersion Coefficient for Experiment 45 (Polydisperse Experiment at 2.0 m s⁻¹)

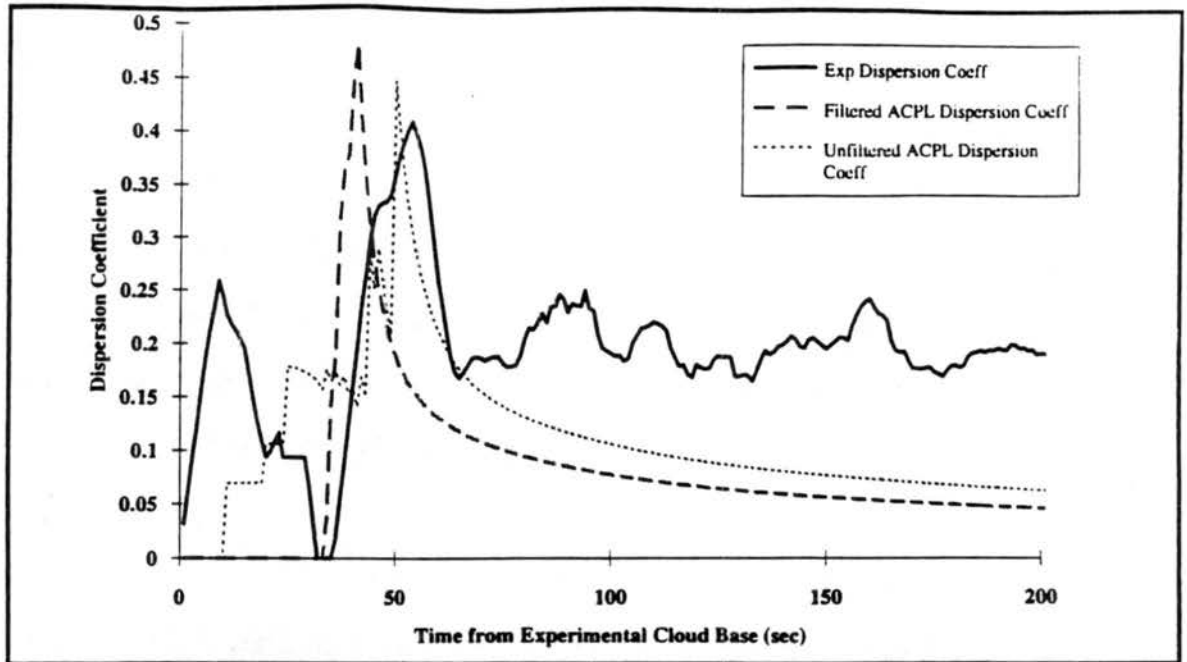


Figure 4.29 Comparison of Experimental (solid line) to Unfiltered (thin dashed line) and Filtered (thick dashed line) ACPL Dispersion Coefficient for Experiment 37 (2 Spike Experiment at 2.0 m s^{-1})

4.5 Summary

The overall objective of the cloud chamber experiments was to study the effect of variations in submicron aerosol loading and updraft velocity on clouds simulated in the cloud chamber. There were several stages of experiment development that contributed to attaining this objective.

First, through analysis of background contamination in the chamber and the actual distribution of aerosol injected by the DMA, it was determined that experiments of the marine stratus nature could be done using the cloud chamber. The chamber was cleaned of CCN and returned to low background contaminants between each experiment. Background contaminant concentrations appeared to remain at less than 0.1 particle

cm⁻³, which was assumed to be inconsequential in the experimental results, even with the low aerosol loading.

Due to instrumental limitations, there is a finite width to the monodisperse aerosol distribution isolated by the DMA. Measured distributions of generated "monodisperse" aerosol indicate a second, smaller peak at a larger diameter. This second peak appeared to be insignificant when compared to the larger concentration primary peak. FSSP broadening of the dispersion coefficient of the cloud droplets makes it difficult to determine if the double charging peak in the injected aerosol peak did contribute to differences in the dispersion coefficient.

Second, aerosol generation and injection techniques were developed to allow several variations in possible injected aerosol distribution types. These types included "monodisperse" distributions centered at 0.04 μm or 0.17 μm , a 2 spike distribution with peaks at 0.04 μm and 0.17 μm , a spike at 0.26 μm with a polydisperse distribution of diameters less than 0.14 μm , and a polydisperse distribution of diameters less than at least 0.54 μm . Primarily, a six jet atomizer filled with ammonium sulfate solution was used to generate a polydisperse aerosol stream. Monodisperse aerosol was selected out of the stream by a DMA. It took approximately 20 to 40 minutes to complete an injection, depending on aerosol distribution type. Verification of the distribution was completed using the DMPS system and took approximately 20 minutes. The injected aerosol distribution appeared to remain stable for the duration of the injection and distribution verification process.

Third, experimental data were compared to ACPL model results. Agreement of pressure and temperature time histories indicate that the experiments were primarily adiabatic in nature. Nucleated aerosol fractions near 1.5 occurred initially for all experiments. The enhancements are too large to be explained by uncertainty alone.

This may be the result of either sampling problems or errors introduced in the data inversion of the FSSP probe, or inhomogeneities observed in the chamber cloud.

When nucleated aerosol fraction was averaged over the time it took for the mean droplet diameter of each experiment to reach 15 μm , the over-estimation of nucleated aerosol fraction is not evident. These averaged values showed a trend of increasing nucleated aerosol fraction with increasing updraft velocity was observed in experimental data. This trend was similar to that predicted by the ACPL model, the results of Chuang and Penner's (1990) modeling study, and Twomey's (1959) theoretical calculations.

Comparison of a nucleated aerosol fraction time history measured during a 1.0 m s^{-1} expansion indicated that the enhanced nucleation may be a function of updraft velocity, and that, on average the aerosol fraction nucleated at 1.0 m s^{-1} is less than that at 2.0 m s^{-1} . A nucleated aerosol fraction time history measured at 0.5 m s^{-1} indicated that inhomogeneities induced by wall temperature control problems may have influenced experiments conducted at that velocity.

Experimental data indicates that increased updraft velocity tends to decrease dispersion coefficient values by approximately 13 %. Decreases of 10 to 15 % in dispersion coefficient with increasing updraft velocity in continental cumulus clouds were observed by Fitzgerald (1972), which may indicate that this trend occurs regardless of cloud type. The dispersion coefficient plots pointed out the need for an addition to the chamber instrument package of a probe that has better resolution in the 0.5 μm to 2.0 μm droplet diameter range. Much of the interesting information is associated with droplet distributions with mean diameters less than 2.0 μm .

There was good agreement between experimental data and ACPL model output in mean diameter and dispersion coefficient. However, the mean diameter versus time plots highlighted a wall temperature control problem that should be corrected in the future.

Finally, based on the results of the cloud chamber experiments and comparison to the ACPL model output, limiting factors on the success of these experiments were determined and lower boundaries of updraft velocity and aerosol number loading have been discussed. The limiting factor on the updraft velocities employable in the chamber was the wall temperature control problem. Information obtained at 0.5 m s^{-1} updraft velocity appeared to have much larger fluctuation in values than those taken at 1.0 m s^{-1} and 2.0 m s^{-1} . This may indicate that the lower boundary of reliable updraft velocities may lie between 0.5 and 1.0 m s^{-1} and most certainly that experiments conducted below 0.5 m s^{-1} will have to wait for improvements to be made in the temperature control algorithm. The FSSP measurements appeared to be the limiting factor of an explicit comparison of number loading influences on marine stratus clouds. More work needs to be done to explain the discontinuities noted.

On average, the experiments agreed with theoretical predictions. It appeared that the chamber (at updrafts greater than 0.5 m s^{-1}) could be used as a link between theoretical studies and natural cloud observation. Ideas for improvements in the cloud chamber facility have been generated by this study and are detailed in Chapter 6.

CHAPTER 5

CONCLUSIONS

A well characterized study of the effect of submicron aerosol on initial stratus cloud properties was conducted. Field measurements taken during the June, 1992 were used to determine the initial conditions of the CSU dynamic cloud chamber for a cloud nucleation study.

Measurements were taken in the North Atlantic in support of the ASTEX/MAGE field project. Over 240 aerosol mobility distributions, representing one hour scans, were taken during the month long project. Aerosol size distributions, surface area distributions, and volume distributions were calculated from the mobility distribution.

Bimodal and monomodal distributions were most frequently observed. Preliminary back trajectory analysis, as well as total submicron number concentration, implied that bimodal air masses were associated with clean, or "marine", air masses. Under such conditions, total submicron aerosol concentrations were measured to be 100 to 900 particles cm^{-3} . On average, peaks in number concentration occurred at 0.04 and 0.17 μm . Bimodal distributions occurred 5 times more frequently than monomodal concentrations. These observations were similar to those made in the North Atlantic and reported by Hoppel et al. (1990).

Monomodal distributions were associated with polluted, or "continentally influenced" air masses. Under these conditions, total submicron aerosol concentrations

ranged from 800 to 1400 cm^{-3} . On average, peaks in number concentration occurred at 0.2 μm .

Sharp concentration gradients in the marine boundary layer were evident in some of the measurements. Rapid increases and decreases in number concentration were accompanied with changes in aerosol distribution shape. Mesoscale horizontal variability was also evident. Changes in the fraction of aerosol in the accumulation and nucleation mode were apparent in consecutive hourly measurements. Such changes are probably caused by mesoscale meteorological influences such as drizzle deposition of the accumulation mode aerosol.

Information from the marine boundary layer measurements was used to initialize a well characterized study of the activation of ammonium sulfate particles as cloud droplets. The experiments were conducted in the CSU dynamic cloud chamber (non-flow through). The ability of the cloud chamber to simulate marine stratus conditions was ascertained by comparing experimental results from the cloud chamber with predictions from the ACPL cloud model.

First, background particle contamination levels were determined to be less than 0.1 cm^{-3} during the injection process and down to 750 mb. Also, the injected aerosol population was found to be stable for more than one hour.

Second, a technique for generation of an essentially monodisperse ammonium sulfate aerosol was developed. These aerosol were then used to determine if the chamber was capable of reproducing a theoretically simple cloud. The diameter and concentration of the monodisperse aerosol were chosen to represent the individual peaks of the bimodal distribution measured during the field project.

Third, experiments using the monodisperse aerosol were conducted to simulated updraft velocities of 0.5, 1.0 and 2.0 m s^{-1} . Several variations in total aerosol

concentration were used. From chamber pressure and temperature data, it was determined that the chamber performed nearly adiabatic expansions at all but the slowest (0.5 m s^{-1}) updraft velocities. However, based on experimental cloud microphysical quantities, it appeared that the experiments conducted at 2.0 m s^{-1} most nearly represented the cloud predicted by theory. Nucleated aerosol fraction and dispersion coefficient were used to make this determination. Repeatability of experiments was determined to be fair. Control of inner liner wall temperatures was implicated in some of the variability evident in the experimental data. Until control of the wall temperature is improved, the lower bound of updraft velocity the chamber is capable of simulating is probably between 1.0 m s^{-1} and 0.5 m s^{-1} .

Finally, once it was determined that, for the most part, the chamber performed nearly adiabatic experiments, other aerosol distribution shapes were introduced. Aerosol generation techniques for each of the new distribution shapes were developed. These shapes included two spike (to represent a "first order approximation" of the bimodal distributions measured during the field project), spike and polydisperse (to represent a "second order approximation" of the bimodal distribution), and polydisperse (to allow for comparison to previous experiments).

Experiments using these new aerosol distribution shapes were also conducted at all three updraft velocities. Comparison of experimental microphysical properties with those predicted by ACPL model indicated that the trends in data from all the experiments were the similar to those modeled. However, the values of the microphysical parameters (nucleated aerosol fraction, mean droplet diameter, and dispersion coefficient) did not match those predicted. An investigation into the contribution of the FSSP sampling system to the observed discrepancies was undertaken. Preliminary results from this investigation indicate that FSSP may be over-estimating the number concentration of

cloud droplets. This may be related to the flow profile that is set up in the sample inlet of the cloud chamber version of the FSSP or to the concentration profile within the flow profile. However, it is uncertain exactly what the concentration profile is and further work on this problem is recommended.

In all, there were 50 experiments conducted for this study of the effect of marine aerosol on initial marine stratus cloud properties. Nucleated aerosol fraction was found to increase with updraft velocity, but decrease with increased aerosol loading. These results agree with those of Chuang and Penner (1990) and Twomey (1959). Dispersion decreased with increased updraft velocity. This result agrees with the observations made by Fitzgerald (1972). Mean droplet diameter was found to increase with updraft velocity and decrease with increased aerosol number loading in agreement with theory given by Pruppacher and Klett (1978).

CHAPTER 6

RECOMMENDATIONS FOR FUTURE RESEARCH

There are numerous areas of improvement and several new avenues of research that have been illuminated by this study. The data set obtained during ASTEX/MAGE has a vast amount of information to still be analyzed. Improvements in sampling technique and software can be implemented with the DMA and CNC and deployed on more ship-based experiments to further the understanding of the marine boundary layer aerosols. The data set obtained in the cloud chamber study can be used to determine improvements that could be made on the cloud chamber and also possibly understand the FSSP measurements biases. The data set, with some enhancements, could be used to improve parameterizations of aerosol-cloud interactions in global climate models. Specific suggestions for further research are detailed below.

6.1 Marine Aerosol Measurement

6.1a Data Set

There is much information to still be gained from the data set collected during ASTEX/MAGE. First, the data taken by the DMPS system, the ASASP and the CN counter on the Malcolm Baldrige should be merged. Aerosol chemistry information should also be incorporated to complete the aerosol information. Back trajectory

information (to be provided by Dr. Chris Bretherton at the University of Washington) can then be used to identify possible areas of aged aerosol as opposed to newer particles. The origins of the aerosol measured from the *Malcolm Baldrige* will then be better understood. Once it is established when the *Malcolm Baldrige* was in clean air masses, it might be possible to investigate the issue of new particle formation from dimethyl sulfide (DMS).

6.1b Technologic Improvements

After comparing data with that taken from instruments operating at higher frequencies, it has become evident that the DMPS software may be more suitable for laboratory use, where aerosol characteristics are much more stable in time. However, there are other options available that measure distributions using the same instrumentation. TSI has marketed software that allows for much quicker distribution measurements to be obtained with sampling statistics that are acceptable. Deployment of a similar instrument configuration as used in ASTEX/MAGE with the addition of the TSI Scanning Mobility Particle Sizer (SMPS) software would improve marine aerosol measurement. Additional information, such as size differentiated marine aerosol composition can be obtained using the MOUDI as well as another configuration of the instruments used in this thesis. The configuration is called Tandem DMA. In this configuration, a dry, monodisperse aerosol stream (isolated using one DMA) is humidified and the distribution is measured by a second DMA. The change via water uptake from a monodisperse aerosol to a polydisperse distribution would provide information on particle hygroscopicity as a function of size.

6.2 Cloud Chamber Studies

6.2a Data Set

The analysis of this data set was exhaustive, but by no means complete. Continued investigation and understanding of the FSSP sampling is a suggested use for this data set. Also, more precise initialization ACPL model runs would allow for assessment of comparison sensitivity to uncertainties in experimental measurements.

Comparison of the data set to other model output is also suggested. For example, Edwards and Penner's (1988) model of CN activation could be initialized with injected aerosol distributions from this set and the output could be compared. Additions to the data set of more variations of the bimodal and monomodal injected aerosol distributions are also suggested. A long term research goal is to use the data obtained during this project and the additions made to it in the future for implementing parameterizations of aerosol-cloud interactions in a global climate model, such as GRANTOUR.

6.2b Technologic Improvements

Several ideas for improvements to the CSU dynamic cloud chamber have formed in the process of developing the experimental design of the project and in collecting the data. For reasons described in section 4.4, Range 1 on the FSSP was used for this investigation. One suggestion that can be made is to use Range 2, or possibly Range 3, of the FSSP when conducting experiments droplet nucleation experiments. As found in this investigation, Range 1 does not allow droplet information, crucial for comparison to

theory to be collected. Another suggestion is to include an optical particle counter like the Climet, or the ASASP, in the instrumentation package used during these types of experiments. The Climet has better diameter resolution than the FSSP.

There are two ideas for improving the cloud chamber FSSP sampling that appear to be fairly straightforward. First, a new, larger inlet design would allow more droplets to cross the laser beam. Preliminary calculations show that volume flow can be increased up to 5 times without perturbing cloud processes within the chamber. This could eliminate some of the sampling statistics problems evidenced in the lower concentration experiments. Second, determination of the distribution of accepted transit times could more exactly define the sample volume, or suggest modifications to do so (refer to Appendix B for a detailed discussion of problem).

There are also several more complicated improvements to the cloud chamber that are suggested. First, improvements should be made to the CCN mixing technique in the chamber. When conducting the experiments, there were times when it was not evident that the small mixing fan was sufficiently mixing the aerosol.

Second, improvements can be made to the pressure control of the chamber. One thing that should be done is to install a smaller valve with a more precise stepping motor that can be used for slow expansions. Another item that should be explored is to find a way to communicate changes in pressure outside the inner liner to the center of the inner liner volume quicker. It is not clear at this moment how to do this, however it appears to be crucial for slow expansions like 0.5 m s^{-1} .

Third, automating the control of the wall temperature with a better control scheme could improve the reliability of results obtained from expansion rates below 1.0 m s^{-1} . Changes in the algorithm that is used to determine the valve positions is recommended. This algorithm must account for both the approximately 30 second time

lag between the valve location and the walls, as well as the fact that the coolant source temperature varies over a 10 °C range. Only the slope of the required temperature change is considered in the current version of the wall temperature algorithm. The coolant source temperature is not currently considered. Another possible change could be to compute the ascent profile point in real time and to include a flag that indicates a cloud has formed and the moist adiabatic cooling rate should be used. Currently the determination of the point where the change from dry to moist adiabatic cooling is based off of initial dewpoint. A cloud flag in the control program would eliminate the influence of the uncertainty of the dewpoint measurement on the cloud.

6.2c Other Suggestions

Once some of these improvements are implemented in the chamber, suggested research includes extending the experimental data to include different chemical species, such as partially neutralized sulfate or volatile organic gases. Another area of research that should be explored with the CSU dynamic cloud chamber is droplet growth, and possibly "cloud cycling" of aerosol, with warm based clouds, especially at slower and variable updraft velocities. A more far reaching suggestion is to perform the experiment described in this thesis in zero-gravity to avoid the effects of sedimentation sorting, which is not included in the ACPL model. In the interim, a more realistic approach to the sedimentation sorting problem in the chamber would be to model the effect.

REFERENCES

- Albrecht, B. A., 1989: Aerosols, cloud microphysics and fractional cloudiness. *Science*, **245**, 1227-1230.
- Alkezweeny, A.J., D.A. Burrows, and C.A. Grainger, 1993: Measurements of cloud droplet size distributions in polluted and unpolluted stratiform clouds. *J. Appl. Met*, **32**, 106 - 115.
- Alofs, D.J., D.E. Hagen and M.B. Trueblood, 1989: Measured spectra of the hygroscopic fraction of atmospheric aerosol particles. *J. Appl. Meteor.*, **28**, 126-136.
- Borrmann, S., R. Jaenicke, and P. Neumann, 1993: On spatial distributions and inter-droplet distances measured in stratus cloud with in-line holography. *Atmos. Research*, **29**, 229-245.
- Braham, R. R., 1977: University of Chicago contribution to METROMEX - II: Final technical report to the National Science Foundation. *U of Chicago Tech. Note 50*, pp. 105.
- Charlson, R. J., J. E. Lovelock, M. O. Andrea, and S. G. Warren, 1987: Ocean phytoplankton, atmospheric sulfur, cloud albedo and climate. *Nature*, **326**, 655-661.
- Chuang, C., and J. E. Penner, 1990: The relationship between aerosol and drop size distributions in the marine atmosphere. *Preprint: 1990 Fall Meeting AGU meeting, San Francisco, Dec. 3-7, 1990*.
- Cooper, W. A., 1989: Effects of variable droplet growth histories on droplet size distributions. Part I: Theory. *J. Atmos. Sci.*, **46**, 1301-1310.
- DeMott, P.J., 1990: Quantifying ice nucleation by silver iodide aerosols. Ph.D. Dissertation, Department of Atmospheric Science, Colorado State University, Fort Collins, Colorado, 253pp.
- , 1993: *personal communication*.

- DeMott, P.J. and D.C. Rogers, 1990: Freezing nucleation rates of dilute solution droplets measured between -30 and -40 °C in laboratory simulations of natural cloud formation. *J. Atmos. Sci.*, **47**, 1056- 1064.
- DeMott, P. J., D. C. Rogers, and R. P. Lawson, 1990: Improvements in the CSU controlled-expansion cloud chamber. *Preprint: 1990 Conference on Cloud Physics, San Francisco, Jun. 23-27, 1990.*
- DeMott, P.J., W.G. Finnegan and L.O. Grant, 1983: An application of chemical kinetic theory and methodology to characterize the ice nucleating properties of aerosols used in weather modification. *J. Climate Appl. Meteor.*, **22**, 1190-1203.
- Dennis, R., ed., 1976: *Handbook on Aerosols*, GCA Corporation, Bedford MA, TID-26608.
- Eagen, R. C., P. V. Hobbs, and L. F. Radke, 1974: Measurements of cloud condensation nuclei and cloud droplet size distributions in the vicinity of forest fires. *J. Appl. Met.*, **13**, 553-557.
- Edwards, L. L. and J. E. Penner, 1988: Potential nucleation scavenging of smoke particles over large fires: A parametric study. *Aerosols and Climate*, P. V. Hobbs and M.P. McCormick, Eds., A. Deepak, 423-434.
- Fitzgerald, J. W., 1972: A study of the initial phase of cloud droplet growth by condensation: Comparison between theory and observation. *U. of Chicago Tech Note 44*. p.144.
- Fitzgerald, J. W., 1991: Marine aerosol: A review. *Atmos. Environ.*, **25A**, 533-545.
- Hagen, D.E., J. Schmitt, M. Trueblood, J. Carstens, D.R. White and D.J. Alofs, 1989: Condensation coefficient measurement for water in the UMR cloud simulation chamber. *J. Atmos. Sci.*, **46**, 803-816.
- Hegg, D.A., L. F. Radke, and P. V. Hobbs, 1984: Measurements of transformations in the physical and chemical properties of clouds associated with onshore flow in Washington State. *J. Clim. Appl. Met.*, **23 (6)**, 979-984.
- , -----, and -----, 1991: Measurements of Aitken nuclei and cloud condensation nuclei in the marine atmosphere and their relation to the DMS-cloud-climate hypothesis. *J. Geophys. Res.*, **96**, 18,727 - 18, 733.

- , R.J. Ferek and P. V. Hobbs, 1993: Aerosol size distributions in the cloudy atmospheric boundary layer of the North Atlantic Ocean. Submitted to *J. Geophys. Res.*
- Hindman, E. E. II, 1989: Formation and optical properties of a warm cloud in a slow expansion cloud chamber. *J. Atmos. Sci.*, **46**, 3653-3663.
- , P. V. Hobbs, L. F. Radke, 1977: Cloud condensation nuclei from a paper mill. Part I: Measured effects on clouds. *J. Appl. Met.*, **16**, 745-752.
- , -----, -----, 1977: Cloud condensation nucleus size distributions and their effects on cloud droplet distribution. *J. Atmos. Sci.*, **34**, 951-956.
- Hobbs, P. V., L. F. Radke, and S. E. Shumway, 1970: Cloud condensation nuclei from industrial sources and their apparent influence on precipitation in Washington State., *J. Atmos. Sci.*, **27**, 81-89.
- , J. L. Stith and L. F. Radke, 1980: Cloud-active nuclei from coal fired electric power plants and their interactions with clouds. *J. Appl. Met.*, **19**, 439-451.
- Hoppel, W.A., J.W. Fitzgerald, G.M. Frick, and R.E. Larson, 1990: Aerosol size distribution and optical properties found in the marine boundary layer over the *Atlantic Ocean*. *J. Geophys. Res.*, **95**, 3659-3686.
- Hudson, J.G., 1993: Cloud condensation nuclei near marine cumulus. *J Geophys. Res.*, **98**, 2693-2702.
- and P.R. Frisbie, 1991: Cloud condensation nuclei near marine stratus. *J. Geophys. Res.*, **96**, D11, 20795-20808.
- and A.D. Clarke, 1992: Aerosol and cloud condensation nuclei measurements in the Kuwait plume. *J. Geophys. Res.*, **97**, 14,533-14,536.
- , J. Hallet, and C.F. Rogers, 1991: Field measurements of cloud forming properties on combustion aerosols. *J. Geophys. Res.*, **96**, 10,847-10,859.
- Jensen, J.B. and R.J. Charlson, 1984: On the efficiency of nucleation scavenging. *Tellus*, **36B**, 367-375.
- King, M. D., L.F. Radke, and P.V. Hobbs 1993: Optical properties of marine stratocumulus clouds modified by ships. *J. Geophys. Res.*, **98**, 2729-2739.

- Lee, I.Y., G. Hanel, and H.R. Pruppacher, 1980: A numerical determination of the evolution of cloud drop spectra due to condensation on natural aerosol particles. *J. Atmos. Sci.*, **37**, 1839-1853.
- Mordy, W., 1959: Computations of the growth by condensation of a population of cloud droplets., *Tellus*, **11**, 16-44.
- Penner, J. E., S. J. Ghan, and J. J. Walton, 1991: The role of biomass burning in the budget and cycle of carbonaceous soot aerosols and their climate impact. *Global Biomass Burning*. J. Levine, Ed., MIT Press, 387-393.
- Politovich, M.K. and G. Vali, 1983: Observations of liquid water in orographic clouds over Elk Mountain. *J. Atmos. Sci.*, **40**, 1300-1312.
- Pruppacher, H.R. and J.D. Klett, 1978: *Microphysics of Clouds and Precipitation*. D. Reidel, Boston, 714 pp.
- Radke, L. F., 1989: Airborne observations of cloud microphysics modified by anthropogenic forcing. *Preprint: Symposium on the Role of Clouds in Atmospheric Chemistry and Global Climate, Anaheim, Jan. 30 - Feb. 2, 1989*, 310-315.
- , J. H. Lyons, P. V. Hobbs, and J. E. Coakley, 1988: In situ measurements of "ship tracks". In *Proceedings of the 10th International Cloud Physics Conference, Bad Hamburg, FRG*.
- Rogers, D.C. and P.J. DeMott, 1990: Measuring ice nucleation rates in a cloud chamber - correcting for delays in crystal detection. *Preprints, Conf. on Cloud Physics, 23-27 July, San Francisco, CA*, 146-148.
- Rogers, R. R., and Yau, M. K., 1989: *A Short Course in Cloud Physics; Third Edition*, Pergamon Press, New York, 60-150.
- Seinfeld, J.H., 1986: *Atmospheric Chemistry and Physics of Air Pollution*, John Wiley & Sons, New York, 23 - 26.
- Squires, P., 1956: The microstructure of cumuli in marine and continental air. *Tellus*, **8**, 443.
- , 1958a: The microstructure and colloidal stability of warm clouds. Part I: The relation between structure and stability. *Tellus*, **256**, 256-262.

- , 1958b: The microstructure and colloidal stability of warm clouds. Part II: The causes of the variations in microstructure. *Tellus*, **256**, 262.
- , and J. Warner, 1959: Some measurements in the orographic cloud of the island of Hawaii and in trade wind cumuli. *Tellus*, **9**, 475.
- TSI, 1983: *Model 3071 Electrostatic Classifier Instruction Manual*. St Paul, Mn.
- TSI, 1988: *Model 3022 Condensation Nucleus Counter Instruction Manual*, St. Paul, Mn.
- Takeda, T., and N. Kuba, 1982: Numerical study of the effect of CCN on the size distribution of cloud droplets. Part I: Cloud droplets in the stage of condensation growth. *J Meteor. Soc. Japan*, **60**, 978-993.
- Twomey, S. A., 1959: The nuclei of natural cloud formation. Part II: The supersaturation in natural clouds and the variation of cloud droplet concentration, *J Appl. Geophy.*, **43**, 243-250.
- , 1977: *Atmospheric Aerosols*, Elsevier, 302 pp.
- Warner, J., 1969: The microstructure of cumulus cloud. Part II: The effect of droplet size distribution of the cloud nucleus spectrum and updraft velocity. *J. Atmos. Sci.*, **26**, 1272-1282.
- White, D., J.L. Kassner, J.C. Carstens, D.E. Hagen, J.L. Schmitt, D.J. Alofs, A.R. Hopkins, M.B. Trueblood, M.W. Alcorn, and W.L. Walker, 1987: University of Missouri-Rolla cloud simulation facility: Proto II chamber. *Rev. Sci. Instrum.*, **58**, 826-834.

APPENDIX A
INSTRUMENTATION

Differential Mobility Analyzer

In the monodisperse aerosol generation mode, the TSI model 3071 Electrostatic Classifier, also called a differential mobility analyzer (DMA), is used to remove a known size fraction of submicron particles from the incoming polydisperse aerosol. The aerosol enters a Kr⁸⁵ neutralizer and is exposed to high concentrations of bipolar ions. The particles quickly reach a state of equilibrium, in which the particles carry a bipolar charge distribution that is assumed to be symmetric around zero and is defined as a Boltzman Distribution.

Once charged, the particles pass from the neutralizer into the main portion of the DMA, depicted by Figure A.1. The DMA is made up of two concentric metal cylinders. The inner cylinder is a collector rod maintained at a controlled negative charge. The outer cylinder is electrically grounded. This creates an electric field between the two cylinders, causing the positively charged particles to be attracted toward the collector rod.

The polydisperse aerosol and the sheath air are introduced at the top of the cylinders and flow through the annular space created by the two cylinders, with the sheath air surrounding the collector rod and the polydisperse outside of that. The flows are laminar with no turbulent mixing of the two streams. Positively charged particles are attracted to the collector rod through the sheath airflow and are precipitated out along the length of the rod. However, not all particles are removed. Some particles exit with the monodisperse aerosol flow through a small slit at the base of the collector rod and the rest are removed in the excess air flow. The electrical mobility of a particle determines whether it exits the DMA through the monodisperse slit.

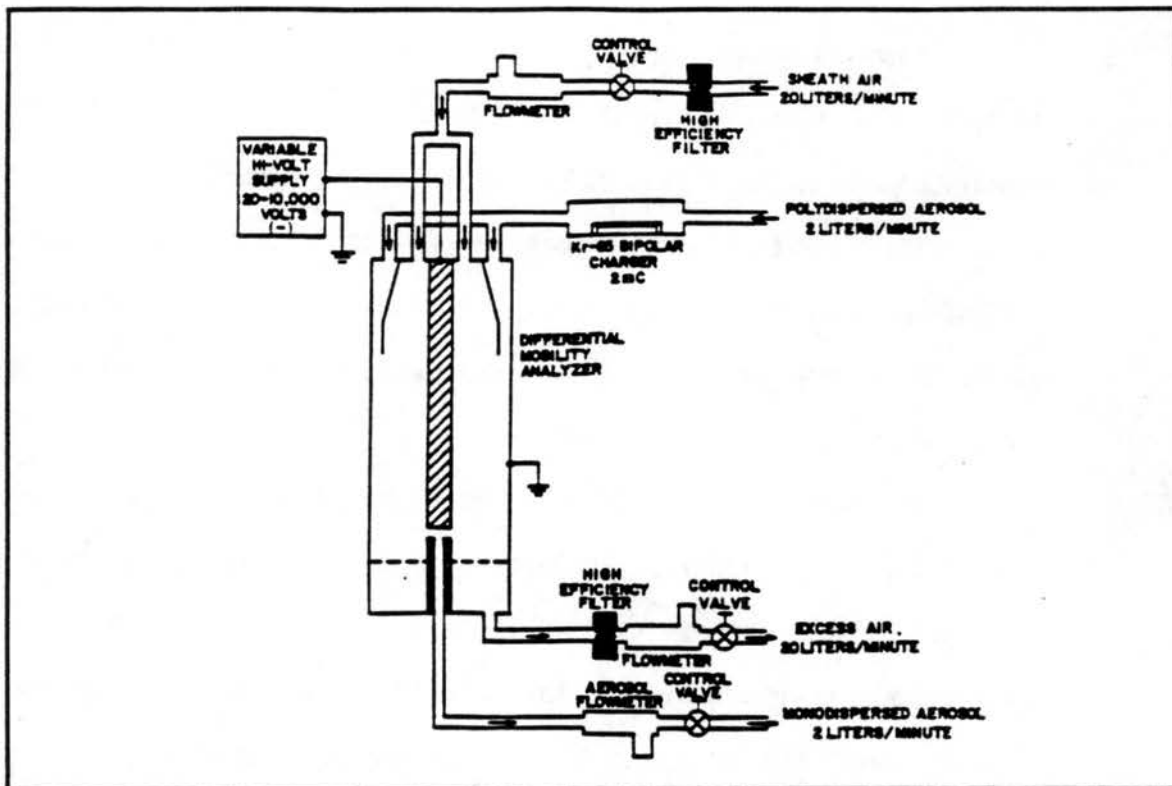


Figure A.1 Schematic of Differential Mobility Analyzer (Model 3071 Instruction Manual, TSI, 1983)

Condensation Nucleus Counter

Particle concentrations were measured using two types of condensation nuclei counters (CNC) The TSI model 3022 was used during the field project and the TSI model 3010 was used in the cloud chamber experiments. Air is pulled through the CNC using an internal pump and mass flowmeter at a rate of 0.5 m s^{-1} . The operating principles of both instruments is relatively similar. Figure A.2 depicts the schematic for the model 3010. Air flows from the inlet immediately through the saturator block, which consists of a reservoir filled with butanol and surfaces lined with butanol soaked felt.

The saturated air then enters a cooled condenser where the butanol vapor condenses on the particles in the air stream, thus forming droplets large enough to be detected by the CNC's optics. The droplets then pass from the condenser tube through a nozzle into the optical detector.

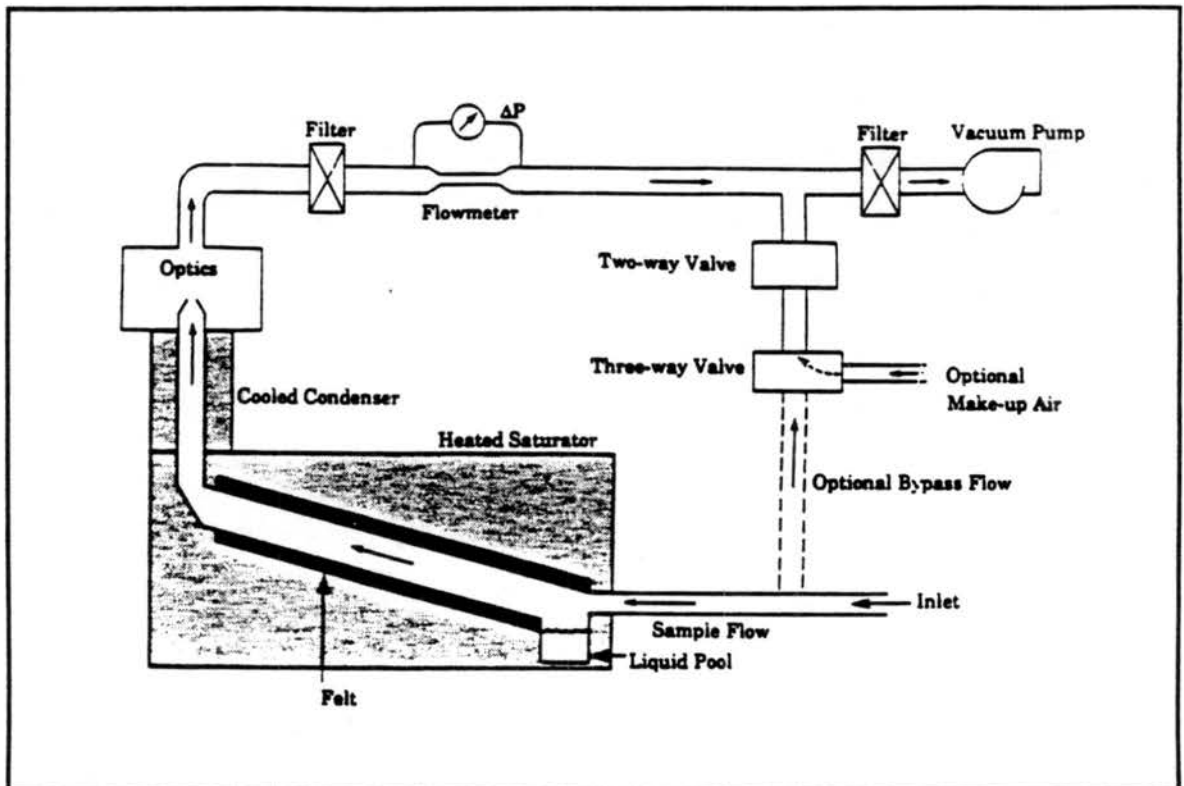


Figure A.2 Schematic for TSI Model 3010 Condensation Nucleus Counter (Model 3010 Instruction Manual, TSI, 1990)

The CNC's focusing optics consist of a laser diode, collimating lens and cylindrical lens, which creates a thin ribbon of light above the exit nozzle. The collecting optics incorporate a pair of aspheric lenses that collect the light scattered by particles passing through the focusing beam, and focuses it onto a low-noise photodiode. The

main beam is blocked by a light-stop in the rear of the sensing chamber. A reference photodiode that monitors the intensity of the incident beam is located behind the light stop.

At concentrations below 1000 particles cm^{-3} , individual electrical pulses generated by light scattered from individual droplets are counted in "real-time" or "count mode". At concentrations between 1000 and 10,000 particles cm^{-3} , these electrical pulses are counted, but only when the signal-processing electronics are available for processing. At concentrations above 10,000 particles cm^{-3} , the instrument measures the total light scattered from all droplets present in the viewing volume at any time. During this study, the concentration was primarily below 1,000 particles cm^{-3} , at any one time, so measurements were made in the "count mode".

Differential Mobility Particle Sizer

Polydisperse aerosol is drawn through the DMA, which produces a monodisperse stream of aerosol, and into the CNC by a pump. The concentrations of monodisperse aerosol are counted in the CNC are recorded, along with the voltage the DMA was set at to generate the monodisperse aerosol, by the DMPS software. The software controls what voltages are used by the DMA based on sheath and polydisperse flow velocities and what size range of particles are needed to be measured.

This particle sizing system was used in both parts of the study. In the field experiment portion, it was used to measure submicron marine aerosol. In the cloud chamber experiments, it was used to verify the aerosol size distribution of the injected aerosol. The plumbing of the system was primarily the same for both portions. During

the field experiment however, the TSI model 3022 CNC was used, while during the cloud chamber work, a model 3010 CNC was used.

Six-jet atomizer

A compressed air-line at 25 psi is attached to the TSI six-jet atomizer. Anywhere from 1 to 6 valves can be opened inside the casing of the instrument, allowing the clean, compressed air into the system. The jet of air rushes over the top of a capillary tube, which is submerged in the solution (in this case - 1 % by weight ammonium sulfate). The rising volume of solution interacts with the jet of air to form a sheet of solution. The sheet then breaks down into small droplets that are forced out of the jet area. Pressurization then forces the droplets out of the atomizer through a port in the top. As the liquid evaporates from the droplets a wet residue particle is left behind. The aerosol then passes through a glass reservoir, to remove large particles from the air flow by impaction on the base of the reservoir, and is dried by a molecular sieve dryer before reaching the DMA. Approximately $6 \times 10^6 \text{ cm}^{-3}$ are produced by the atomizer. The loss through the diffusion dryers is approximately 50%. Figure A.3 shows the distribution of aerosol generated by this configuration.

One-jet Bubbler

The one-jet plastic bubbler system works on the same principle as the six jet atomizer. A compressed air line is connected to a glass pipette that is sealed into the lid of a plastic wide-mouth bottle on one end and submerged in solution on the other end. The clean compressed air forces bubbles to form and burst at the surface, leaving behind

a particle residue which are forced out through another port sealed into the top of the bottle. The air then follows the same path as that described above for the six-jet atomizer. Figure A.4 show a schematic of how the six-jet atomizer and the one-jet bubbler interface with the tubing system described.

Micro-orifice Uniform Deposit Impactor

The MOUDI is a cascade impactor that is generally used for aerosol studies. It is composed of eight stages that have cutpoints ranging from 18 μm to 0.05 μm . Each stage is specifically designed to create a jet of air that is impinged upon an impaction plate. Particles larger than the cut sizes of that stage cross the air streamlines and are collected upon impaction. The smaller particles follow the streamlines and proceed onto the next stage. This is continued through the cascade impactor until the smallest particles are removed. Figure A.5 is a schematic diagram of a typical MOUDI stage. Air is

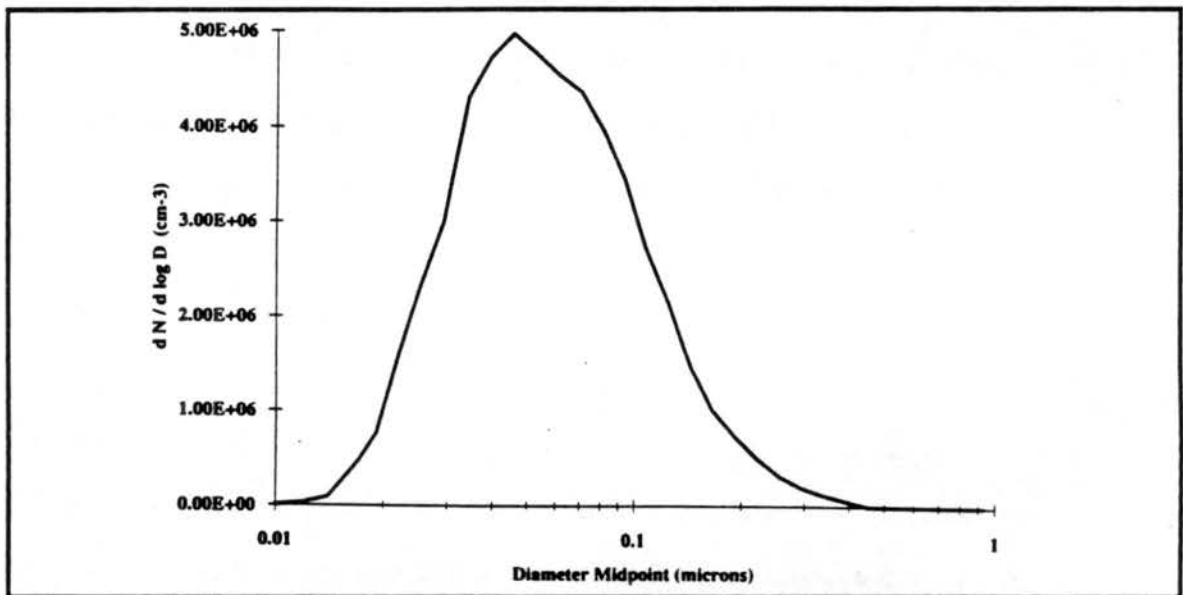


Figure A.3 Aerosol Size Distribution Generated Using Six Jet Atomizer

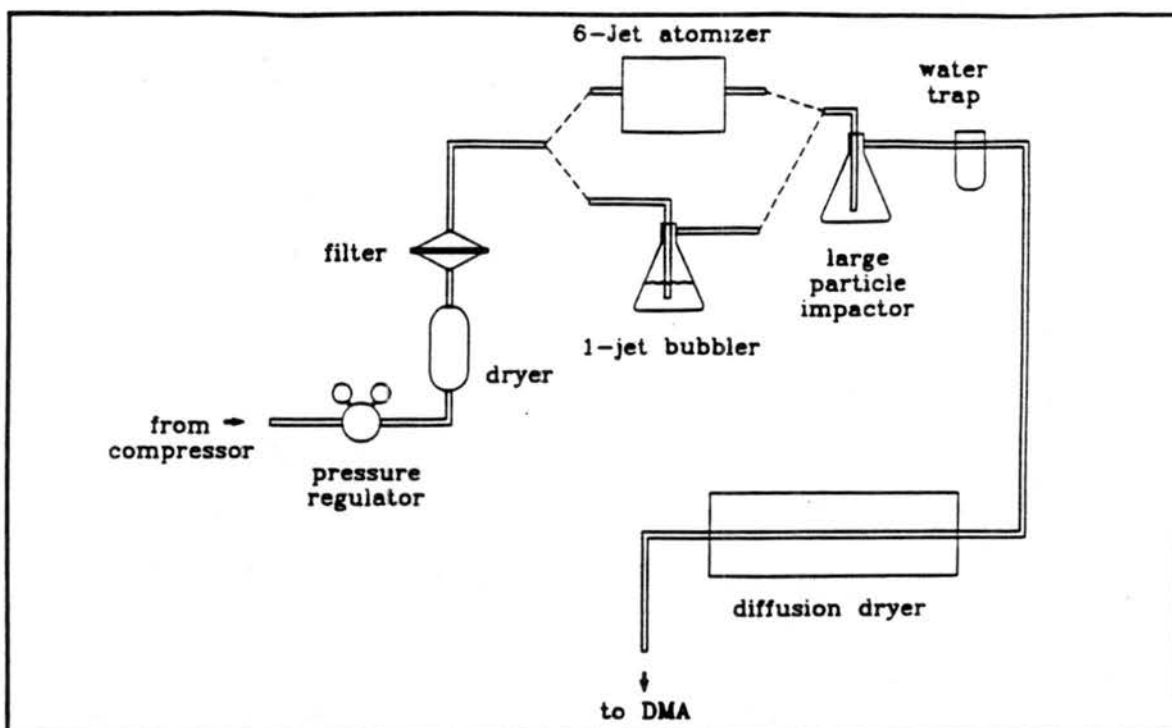


Figure A.4 Schematic of Aerosol Generation System

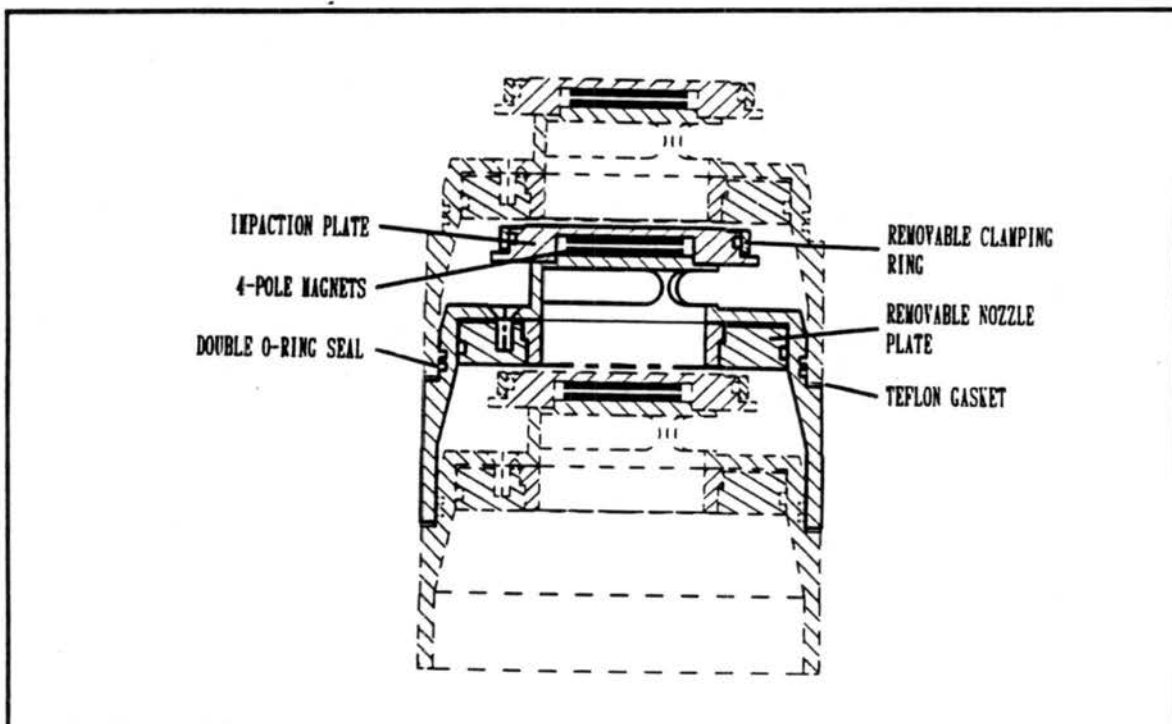


Figure A.5 Schematic of Microorifice Uniform Deposit Impactor (MOUDI Instruction Manual, MSP Corp., 1991)

generally pulled through the MOUDI by an external pump at 30 lpm. For this study, however, the aerosol was pushed through the stages by the pressure of the one-jet bubbler. Only seven stages were used, with the last one having a cutpoint of 0.1 μm .

Dynamic cloud chamber

The dynamic cloud chamber consists of a 2.0 m³ stainless steel outer pressure vessel which houses a thin cylindrical inner copper line. The line is vented to the pressure vessel by small holes in the top and bottom plates. The total experimental working volume of this inner line is 1.19 m³. In the adiabatic expansion mode, air is evacuated at a controlled rate from the pressure vessel using a vacuum pump and, in most cases, a valve controlled by a stepping-motor, to produce expansion cooling of the sample air. For the study reported in this thesis, the stepping-motor controlled valve was over-ridden and a valve was controlled manually using a flowmeter. The evacuation rate is calculated by computer and displayed, based on pre-determined initial conditions of temperature, pressure, humidity and ascent rate. Initially, the automated valve A rotameter flowmeter was manually regulated so that the actual pressure in the chamber was similar to the program pressure and to ensure a continuously smooth expansion. The volume between the pressure vessel and the inner liner acts to dampen changes in flow rate out of the inner volume. The temperature of the inner liner wall is cooled to match calculated mean air temperature by circulating LEXSOL fluid (from Santa Barbara Chemical Company) through spiral-wound copper tubing soldered to the exterior of the copper liner. Large compressors are used to cool the fluid. The rate at which the cooling fluid is circulated through the loop is regulated by a computer-controlled digital valve. (DeMott, 1990)

The temperature is controlled manually before the expansion by setting digital valve positions according to the deviation of the wall temperature from the desired value. Humidity is controlled by a steam boiler system that is tapped into a preconditioning system and is usually set before sample aerosol is injected into the chamber. Initial pressure is usually considered to be the ambient pressure at the time of the expansion. The simulated ascents are based on equations for dry adiabatic expansion until a cloud forms, and then on moist adiabatic expansion. Computed air parcel pressure and temperatures are output to an ascent profile memory system that is initiated just prior to reaching the desired initial conditions. A relatively homogeneous working volume, free from large thermal or vapor gradients, is thus made to simulate a wide range of air parcel and cloud conditions (see Table A.1).

Table A.1.
Dynamic Cloud Chamber Working Ranges and System Tolerances

Type	Range	Tolerance
Temperature	-55° to +40° C	+/- 0.2 ° C
Pressure	300 mb to 900 mb	+/- 0.5 mb
Relative Humidity	0.1 % to >100 %	+/- 0.5 in dewpoint temp.
FSSP diameter (Range 1)	2.0 to 32.0 μm	
Simulated Ascent Rate	0.2 m s ⁻¹ to 20 m s ⁻¹	

* Values taken from DeMott, 1990.

Various measurement systems are used during experimentation. Temperature is measured continuously using an array of ten copper-Constantan thermocouples (0.508 mm wire) located on the inner liner and four type E fine-wire (12.5 μm) thermocouples inserted 25 cm into the inner air volume. Pressure is measured using two strain gauge

type transducers. Humidity is measured using two optical condensational-type dewpoint hygrometers. The usable ranges and system tolerances of the dynamic cloud chamber can be found in Table A.1.

Cloud droplet sizes and concentrations and their changes in time are measured using a Particle Measuring Systems (PMS, Boulder Colorado) Forward Scattering Spectrometer Probe (FSSP-100). A special sampling system has been designed to draw cloudy air from the chamber through the laser optics of the probe. The FSSP sampling frequency is 1 Hz. Measurements accumulate in the FSSP and are downloaded to the data system once per second. The FSSP measurements are also used to compute dispersion coefficient for the droplet distribution and liquid water content. The dispersion coefficient is defined as the standard deviation divided by mean diameter of each distribution constructed by the FSSP. Liquid water content is the amount of available liquid water per unit volume of air sampled.

The current data acquisition system is based on an IBM-compatible PC-386 20 MHz computer. All variables stated above and some not included in this thesis are recorded using this system. The software which controls the data system and some of the control operations discussed previously have been designed for maximum flexibility, including layered windows and real-time display of state parameters and hydrometeor spectra. Displays are updated once per second and are selectable in real-time. Data are recorded, also once per second, onto a 150 MB hard disk and can be downloaded to high density tapes for permanent storage (DeMott, 1990).

References

- DeMott, P.J., 1990: *Quantifying ice nucleation by silver iodide aerosols*. Ph.D. Dissertation, Department of Atmospheric Science, Colorado State University, Fort Collins, Colorado, 253pp.

APPENDIX B

**FSSP VELOCITY ACCEPTANCE RATIO AND SAMPLE VOLUME
RELATIONSHIP**

(Contributed by Paul J. DeMott)

In order to accommodate sampling of cloud droplets from the CSU dynamic cloud chamber during experimentation, a suction sampling system was adapted to a Particle Measuring Systems Forward Scattering Spectrometer Probe (FSSP-100). This system has been described by DeMott and Rogers (1990) in some detail, but this appendix describes further details of the system in order to more carefully define uncertainties involved in measuring both droplet concentrations and diameters.

The intent of the sampling system designed for the FSSP in about 1981 was to draw droplets into the FSSP in a horizontal mounting position, focus the droplet stream into the laser beam so as to well define the depth of field for measurement, and provide a sensitive sampling volume of approximately $1 \text{ cm}^3 \text{ s}^{-1}$ so that the concentration signal from the probe did not need correction. While the particular design eliminates a number of potential measurement uncertainties and subsequent corrections required for the FSSP when flown on an aircraft as discussed by DeMott and Rogers, a more careful analysis reveals that sample volume definition remains a rather elusive problem barring further study or electronic modification.

This discussion is organized to describe the geometry and mechanics of the sampling system and then consider the effect of these characteristics on uncertainty in measuring concentrations of cloud droplets sampled from the cloud chamber. Peculiarities of the FSSP and the interaction of these characteristics with the sampling system are also analyzed. Finally, a best estimate of effective sampling volume is made and uncertainty described. The second part of this document describes calibration tests performed to more clearly define the size bin limits and artificial spectral broadening of droplet size distributions for the FSSP in this research.

FSSP Sampling System Design

Figure B.1 shows a schematic of the FSSP sampling system geometry. The glass tube inlet begins about 10 cm inside the inner liner of the cloud chamber. The inside diameter of the inlet is 1 cm at this point. In about 1 cm distance along the inlet the tube necks trumpet-like down to 0.3 cm. Within another few centimeters of length, the tube achieves its final inside diameter of 0.065 cm. The sample flows through this diameter tube for the final 18 cm until it exits 0.1 cm in front of the FSSP laser beam. The laser crosses perpendicular to the droplet stream path. Its diameter is specified as 0.0187 cm by the manufacturer, and this value was verified during calibration tests by Droplet Measurement Technologies (Boulder, CO) in 1987. Using fine wires, the droplet stream was focused through the laser beam such that the beam passes through the very center of the droplet field. The width (diameter) of the droplet stream defines the DOF of the FSSP in this application. This is a simplification over the situation presented on an aircraft.

Sample flow rate has been measured as $6.667 \text{ cm}^3 \text{ s}^{-1}$ on various occasion. An automated flow control circuit using a pressure transducer is designed to control this flow rate within 5% as pressure changes in the cloud chamber. In reality, the uncertainty in flow rate is much less during controlled expansion. In the experiments reported in this thesis, manual control was used to smooth out the normally stepwise expansion profile. The flow rate uncertainty in this configuration was less than 0.2%, leading to concentration uncertainties of the same order.

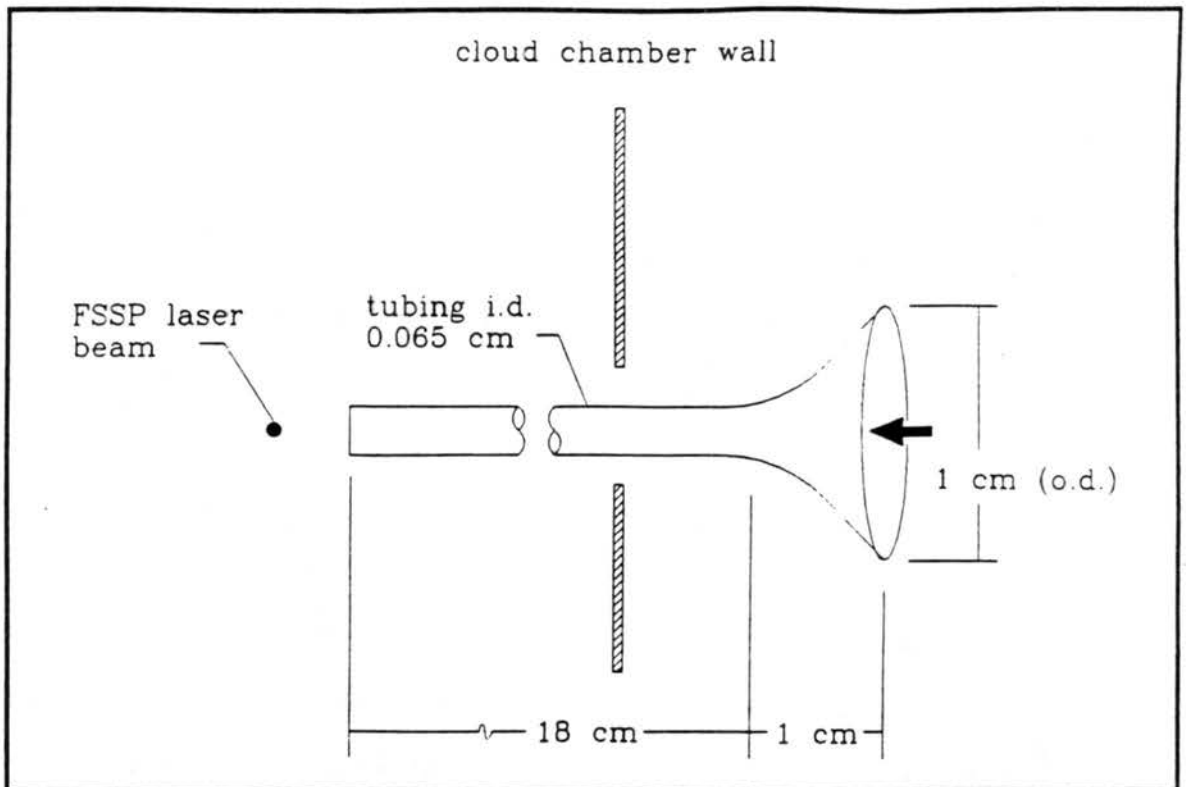


Figure B.1. Schematic of FSSP sampling system inlet. Drawing is to scale excepting the trumpet section of the inlet tube.

A flow rate of $6.667 \text{ cm}^3 \text{ s}^{-1}$ through the inlet implies an average velocity of 2009 cm s^{-1} where the droplet stream exits and crosses the FSSP laser beam. The area intercepted by the laser beam is $1.216 \times 10^{-3} \text{ cm}^2$. Thus, the simplest considerations imply a total sample volume flow rate of $2.44 \text{ cm}^3 \text{ s}^{-1}$ through the laser beam. Of course, the "effective" sample volume for most FSSP's is on the order of 50% of this value. The effective sample volume s^{-1} is more exactly determined by the Velocity Averaging circuitry of the FSSP. The purpose of this circuit is to "reject" particles which have transits through the laser beam which are too much shorter than the average or through too short of a transect of the beam to be sized properly. As designed for aircraft use, this circuitry rejects particles which transit through the edges of the beam where the instrument is known to undersize particles due to weaker scattered power (e.g., Dye and

Baumgardner, 1984). The circuit operates by gating particle transits through the beam with a 10 MHz clock. Counts are done on an 8-bit (256 resolution) counter. Counts are averaged from the start of cloud entry and the average is upcounted or downcounted by the difference between the average and the count of each new droplet as time goes on. Particles which have counts less than the average are included in the average but are rejected from the effective sample volume for being too fast in transecting the beam. The ratio of the "accepted" particles transecting the DOF to the total particles in the DOF (total strobes) during a sample period is referred to as the Velocity Acceptance Ratio (VAR). This quantity can be measured and is recorded on the CSU data system. Experience has shown that the VAR in cloud chamber experiments has ranged from about 0.3 to 0.5. So, as desired in the original design, the sampling system provides a volume sample volume flow rate of near $1.0 \text{ cm}^3 \text{ s}^{-1}$ if the flow is a constant 2009 cm s^{-1} through the laser beam. Such a straightforward relationship has been assumed in the past, but it is not really valid.

Sample System Flow Profile

The validity of the assumption of constant flow is now analyzed. The Reynold's number of the flow in the sample tube may be calculated as,

$$\text{Re} = \frac{U d}{\nu} \quad (\text{B.1})$$

where U is the average velocity, d is the tube diameter, and ν is the kinematic viscosity of air. Taking $U = 2009 \text{ cm s}^{-1}$, $d = 0.065 \text{ cm}$, and $\nu = 0.15 \text{ cm}^2 \text{ s}^{-1}$, Re is evaluated to be 837. This places the flow solidly in the laminar flow regime. Values exceeding 2000 are

typically associated with turbulent flow (see, e.g., Knudsen and Katz, 1979). If a tube is long enough, parabolic laminar flow results. The distance required to develop fully parabolic flow is given by,

$$Z_t = 0.03 \text{ Re } d \quad (\text{B.2})$$

ZT is 1.6 cm for the sample inlet used. Thus, parabolic flow is assured by the time the sample flow exits to the region of the laser beam. Since the distance between exit and interception of the laser beam is only about 0.1 cm, it is unlikely that the parabolic flow profile is much disturbed by the $2000 \text{ cm}^{-3} \text{ s}^{-1}$ average velocity sheath flow which surrounds the droplet stream in the measurement region. This sheath flow is intended simply to keep the droplet stream intact through the measurement region. Smoke tests were used to verify this design aspect.

Figure B.2 shows a schematic of various view perspectives of the analyzed flow intercepting the laser beam. For flow through a pipe, the velocity u at any point (x,y) from the tube center is given by,

$$u(x,y) = \frac{2Q (R^2 - (x^2 + y^2))}{\pi R^4} \quad (\text{B.3})$$

where Q is the average volume flow rate. As a result, the laser beam intercepts an average flow not of Q , but of,

$$Q_c = \frac{8Q (R^2 - (x^2 + y^2))}{\pi R^4} dx dy \quad (\text{B.4})$$

This is an approximation which neglects the curvature of the intercepting droplet stream near the edge of the beam. It can be calculated that Q_c is $3.11 \text{ cm}^{-3} \text{ s}^{-1}$. Q_c would be less if the beam were not centered through the droplet stream. Nevertheless, this flow

exceeds the $2.44 \text{ cm}^{-3} \text{ s}^{-1}$ computed earlier based on the average flow velocity. The effective sample volume flow rate is determined by the interaction between the VAR circuit and the flow profile, as now addressed.

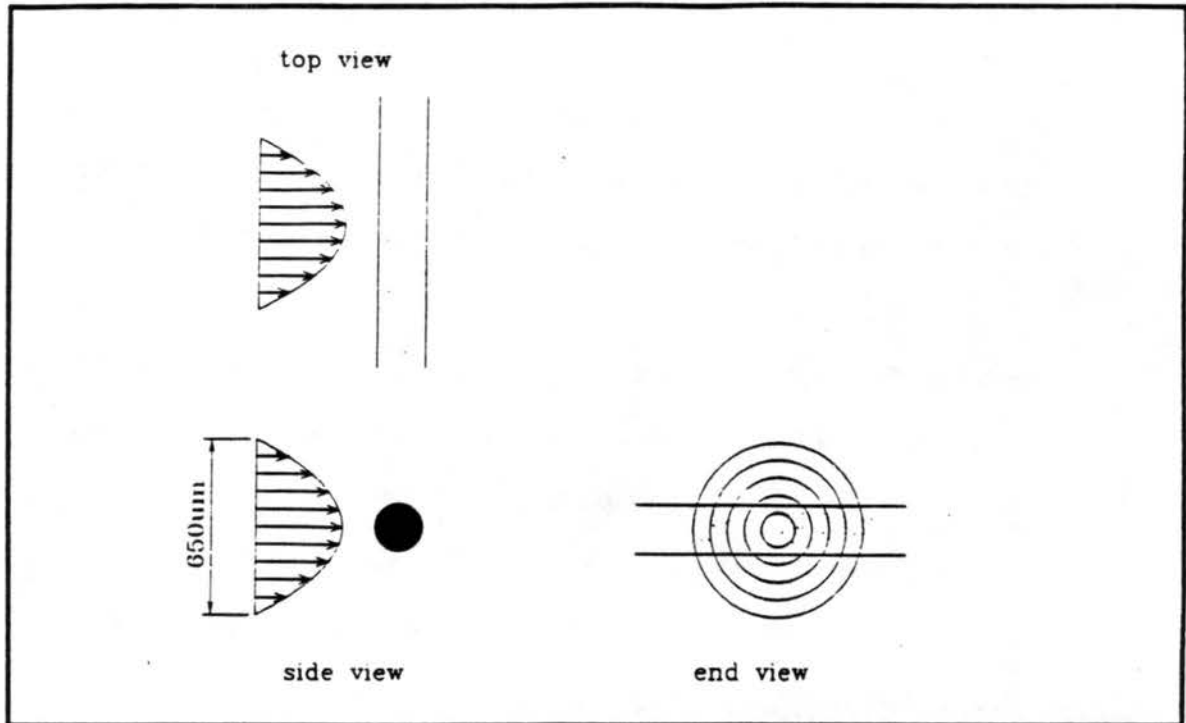


Figure B.2. Schematic diagram of various perspectives of FSSP sample flow intersecting the laser beam.

VAR and Effective Sample Volume for the CSU FSSP Sampling System

The meaning of VAR is not clear for the sample flow profile into the FSSP in the dynamic cloud chamber. It does not represent a simple ratio between the accepted and rejected areas of the beam as it was intended, and the rejection region is not likely to be as intended. In order to estimate the effective sample volume flow rate, a computer program was written to compute the transit times at various positions in the beam based on the beam depth, $b_w = 2 (R_b^2 - y^2)^{0.5}$, and the velocity $u(x,y)$. Then, given a spatial

distribution of droplets, the average transit time was calculated as the ratio of particles with transit times greater than the average to those with transit times less than or equal to the average. The accepted sample area and volume could also be calculated. The major uncertainties involved are the nature of the spatial distribution of droplets, the resolution and accuracy of the FSSP measurement of the transit time average, and the existence of a minimum velocity required for accepting a valid droplet count.

The nature of the particle distribution profile with respect to the flow is perhaps the most uncertain of the variables involved in the sample volume calculation. The three distribution profiles considered here are shown schematically in Figure B.3. Some guidance as to which profile is most likely realized experimentally is given by comparing the corrected droplet concentrations which result from each assumption to the numbers plausible based on the number concentrations of CCN injected in the experiments described in this thesis. A uniformly distributed population of droplets crossing the laser beam was a reasonable first assumption. However, two factors probably invalidate this assumption ultimately. These factors are the likely y-component of particle trajectories at the funneled sample entry (depicted in Figure B.3), and the repositioning of droplets by sedimentation during transit through the sample tube. No calculations are presented here regarding the first factor. Specific trajectory calculations would be one approach. The second factor will become an important one as droplets exceed 20 μm in diameter. While a careful analysis of this problem is not offered here, since droplet diameters were less than 20 μm through the sensitive portion of the experiments described in this thesis, Table B.1 gives estimates of particle penetration P (defined as the ratio of concentrations entering versus exiting the sample tube) based on the calculations outlined on pages 207-208 of Vincent (1989). The combined effects of the two repositioning factors would be the concentration of particles within the central

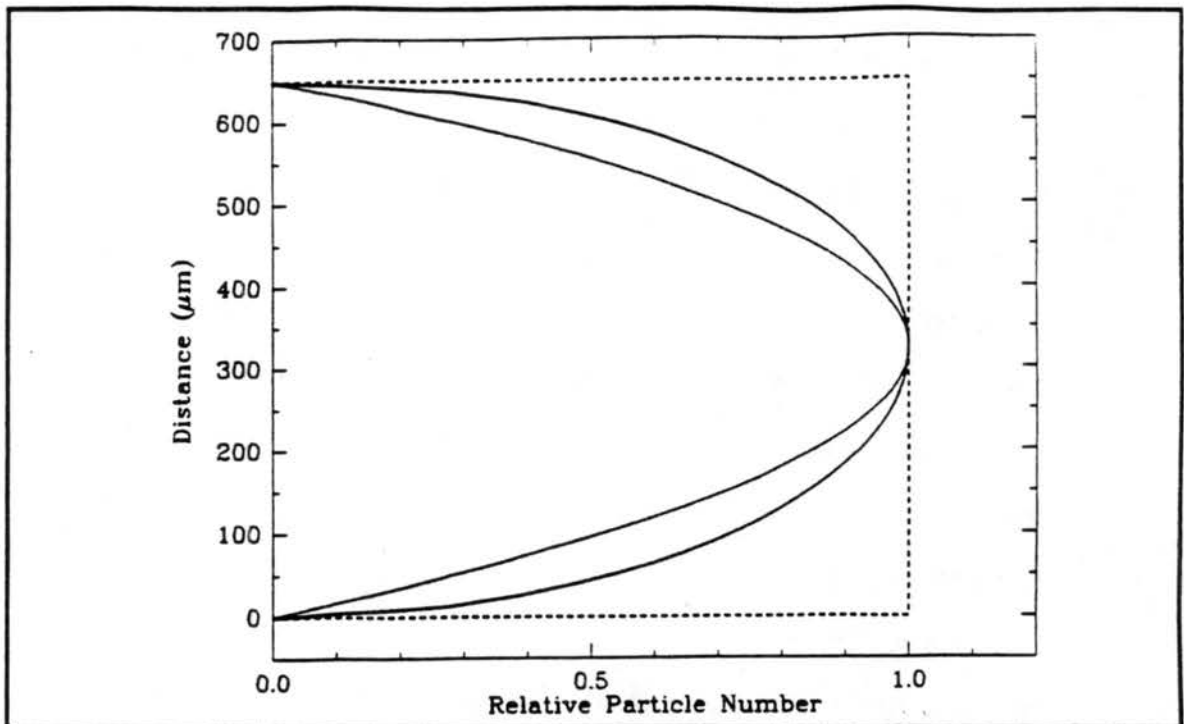


Figure B.3. Schematic showing the three assumptions made for the spatial distribution function of particles in the FSSP sample flow. These were a uniform distribution (a), parabolic distribution (b), and the square root of parabolic (c).

Table B.1.
Particle penetration through FSSP sample tube

Droplet Diameter (μm)	Penetration
10	0.96
20	0.80
30	0.58

part of the sample tube and the creation of a mostly droplet-free zone at least at the top region of the tube. For these reasons, a parabolic particle distribution profile was considered as a possible extreme case, and a more likely profile following the square root of the parabolic values was considered. Uncertainties precluded considering any more complex profiles. Each profile was considered as a nominal situation upon which

the uncertainties due to transit time average calculation were superimposed to determine a nominal uncertainty for measured droplet concentrations.

The velocity averaging technique introduces fairly well defined uncertainties into a calculation of effective sampling volume. The transit time t may be calculated as,

$$t = \frac{bw \text{ (clock rate)}}{u(x,y)} \quad (\text{B.5})$$

The clock rate of the FSSP was changed in 1987 to 5 MHz in order to keep the counts at the average sample flow rate within the dynamic range of the counter. This determines that the resolution of transit time is 0.2 μs . This resolution carries through to the average of all particle transits in a unit time, so may be taken to define a nominal minimum uncertainty in calculating droplet concentration for each assumed particle distribution profile. There is probably as much or more uncertainty in ascribing a known transit time to particles 5 to 20 μm , particularly toward the edges of the beam. For example, a 10 μm particle passing through a point 50 μm above the laser beam centerpoint and 200 μm to the left or the right of a vertical line through the center of the droplet stream would span a range of transit times of 6.6 \pm 0.2 μs . For a 20 μm droplet the range of t it covers at this point in the beam is 6.6 \pm 0.4 μs . Thus, the accuracy of the transit time average may be much less than the apparent electronic resolution.

Due to the electronic method of computing VAR and the average transit time, particles may be rejected for all velocities less than 365 cm s^{-1} (730 cm s^{-1} with a 10MHz clock; thus the PMS quote of approximately 10 m s^{-1} as recommended minimum velocity). At this velocity, the transit time counter will "rollover". Although the counts generated after rollover may be too small for acceptance, the incorrect transit time will be averaged in with all other pulses. This was accounted for in calculations. This 365 cm

s^{-1} limit is fairly vague. Coupled with the likelihood that few particles will pass through the region of velocities below 1000 cm s^{-1} , it is suspected that this causes much of the variation in VAR noted in cloud chamber experiments (although Dye and Baumgardner note substantial variability in VAR even for an FSSP flown on an aircraft). For this reason, a relationship was established between VAR and sample volume for each particle distribution profile by assuming minimum velocities between 1 and 20 m s^{-1} below which no particles were assumed to transit the beam or those that did were rejected.

The calculated VAR region for an assumed uniform particle distribution across the droplet stream and a minimum accepted velocity of 1000 cm s^{-1} is depicted in Figure B.4. The area represented in the accepted region is 33% of the total area of the droplet stream which intercepts the laser beam at velocities greater than 1000 cm s^{-1} . Since the

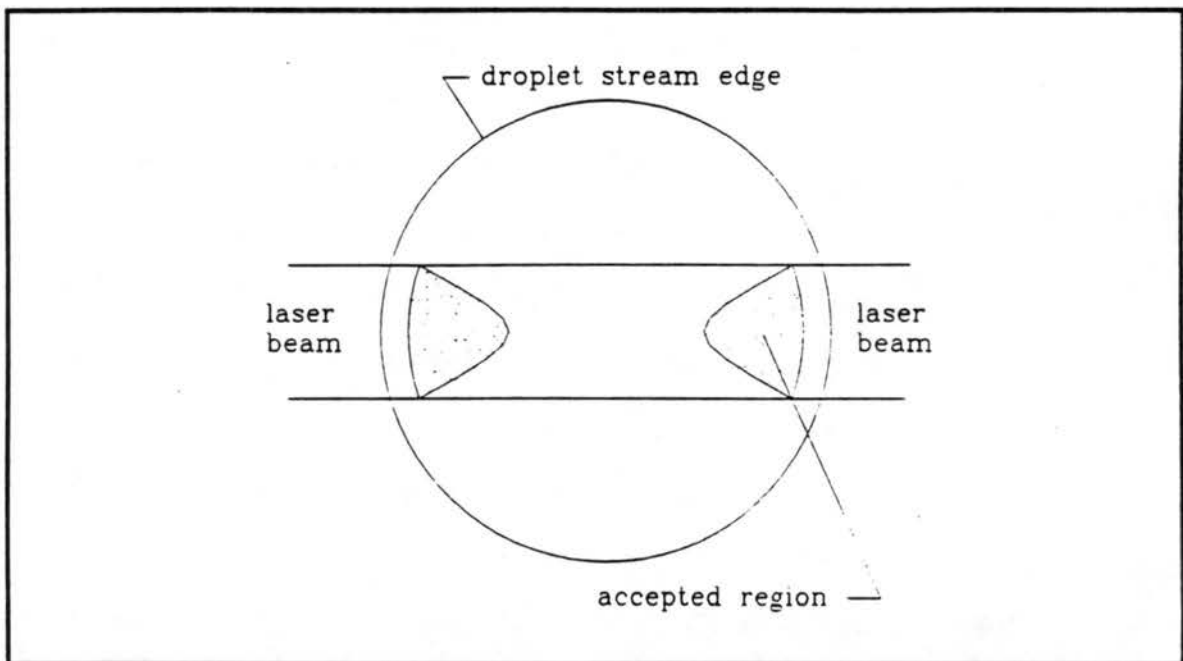


Figure B.4. Cross-section of FSSP laser beam intercepting sample flow, showing the region where uniformly distributed droplets have transit times greater than average ("Accepted"). A minimum required particle velocity of 10 m s^{-1} was assumed in this case.

particles are uniformly distributed, the VAR is 0.33. Q_c through this region is $0.7 \text{ cm}^{-3} \text{ s}^{-1}$. Of note is the rejection of particles through the center of the droplet stream where airflow is highest and transit times are too short.

Figure B.5 shows the sample volume versus VAR relationship obtained by varying the velocity limit. Table B.2 lists the values plotted. Increasing the velocity limit increases VAR and sample volume while decreasing the velocity limit decreases these quantities. Lower or higher values of VAR could only result from a very non-uniform droplet distribution in the beam. This becomes a concern for low droplet concentration measurements. The nominal uncertainty of the relationship shown in Figure B.5, as determined only by the minimum transit time resolution is displayed by

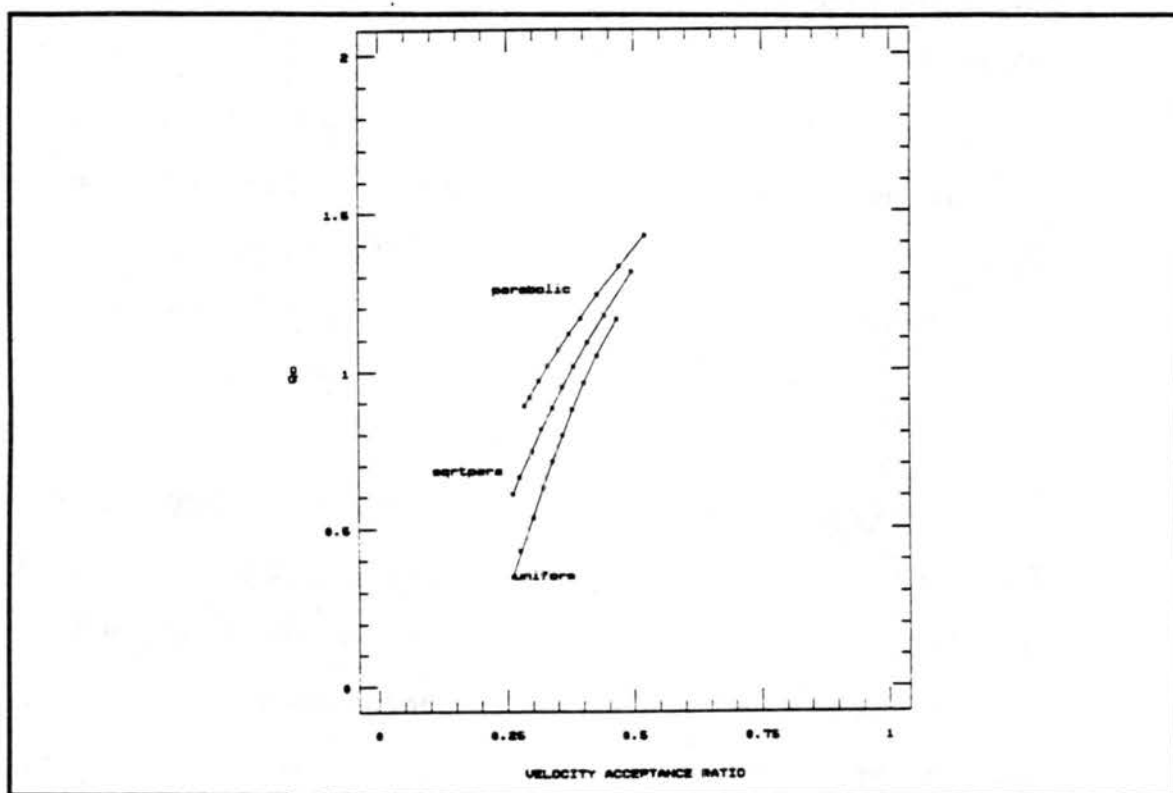


Figure B.5. Sample volume versus VAR for the three assumed droplet spatial distribution functions.

error bars. Since VAR averaged close to 0.3 in the experiments performed in this thesis, an assumption of a uniform distribution profile in the droplet stream seems quite unrealistic because it suggests nearly a factor of 2 correction to droplet concentration values ($1 \text{ cm}^{-3} \text{ s}^{-1}$ sample volume was assumed). This would imply a factor of two higher droplet concentrations compared to available CCN concentrations in some of the experiments, which is impossible.

Sample volume versus VAR values calculated assuming a parabolic distribution of droplets across the laser beam are also plotted in Figure B.5 and are listed in Table B.2. It is noted that the relationship between the two quantities has a lower slope than for the uniform distribution assumption. This is more consistent with the measured variations of VAR and droplet concentration in the experiments performed. The implied Q_c for the average experimental VAR is $0.94 \text{ cm}^{-3} \text{ s}^{-1}$. The true distribution of droplets through the beam over a sufficient sample period is most likely somewhere between the extreme cases of uniform and parabolic profiles. The calculations with a droplet distribution which is the square root of the parabolic were made as a best estimate of this true distribution in the sample flow. These results are also shown in Figure B.5 and Table B.2. For an average VAR of 0.30 measured, Q_c is given as $0.750 \text{ cm}^{-3} \text{ s}^{-1}$. The most exact calculation of FSSP concentrations from total counts is to apply a best fit to the calculated VAR versus sample volume flow relationship. A polynomial fit of the form $Q_c = a(\text{VAR}) + (b(\text{VAR}))^2 + (c(\text{VAR}))^3 + (d(\text{VAR}))^4$ gives $a = -2.2498$, $b = 32.6466$, $c = -71.6218$, and $d = 51.8157$ with a correlation coefficient squared of very nearly 1.0. However, it cannot be expected that the relationship between VAR and volume sampling rate will be the same outside of the range calculated for the reasons previously mentioned. For a simpler linear correction valid within about 5% over the calculated

Table B.2.
Sample volume versus VAR as function of particle distribution in beam.

a) Droplets Uniformly Distributed in Beam Space:

VAR	Qc (cm ⁻³ s ⁻¹)	Velocity limit (m s ⁻¹)
0.262	0.348 (+ 0.021/-0.020)	1
0.276	0.429	4
0.302	0.534	6
0.322	0.627	8
0.340	0.711 (+ 0.081/-0.069)	10
0.358	0.795	12
0.379	0.896	14
0.402	0.960	16
0.428	1.048	18
0.466	1.162 (+ 0.342/-0.233)	20

b) Droplets Parabolically Distributed in Beam Space:

VAR	Qc (cm ⁻³ s ⁻¹)	Velocity limit (m s ⁻¹)
0.285	0.888 (+ 0.100/-0.084)	1
0.295	0.916	4
0.313	0.968	6
0.331	1.016	8
0.352	1.067 (+ 0.056/-0.044)	10
0.373	1.117	12
0.395	1.164	14
0.428	1.238	16
0.471	1.327	18
0.521	1.427 (+ 0.232/-0.349)	20

c) Droplets distributed as (parabolic value)^{0.5} in beam space:

VAR	Qc (cm ⁻³ s ⁻¹)	Velocity limit (m s ⁻¹)
0.262	0.607 (+ 0.051/-0.047)	1
0.275	0.660	4
0.298	0.742	6
0.318	0.813	8
0.339	0.882 (+ 0.117/-0.095)	10
0.359	0.948	12
0.381	1.014	14
0.409	1.091	16
0.442	1.175	18
0.495	1.310 (+ 0.273/-0.311)	20

range, concentration values can be calculated by normalizing to the average VAR conditions. That is,

$$nd = \frac{(\text{total strobos}) \text{ VAR}}{Q_c} = 0.4 (\text{total strobos}) \quad (\text{B.6})$$

An analysis of the uncertainty introduced just by the sample transit time measurement resolution implies a nominal minimum sample volume uncertainty of approximately 15%. This translates to the same minimum uncertainty in droplet concentrations. In reality, the uncertainty may be twice this value, as suggested previously by DeMott and Rogers (1990).

It appears feasible that the distribution of transit times can be measured for future experiments, giving more information about the distribution of particles in space in the sample inlet stream. This should result in a much more accurate estimate to be made of Q_c and its variability and relationship to VAR for the sample system as it now exists. It may also be possible to electronically restrict accepted transit times to enclose a known sample volume. Such studies should also include a measurement of the temporal distribution of particle transit events (along the lines of "fast FSSP" modifications made by Brenguier et al., 1993 and Baumgardner et al., 1993) since this would give a quantitative estimate of the validity of the assumption of negligible droplet interactions made in the theory of the growth of droplet populations.

One final point should be made regarding the unusual VAR region which results from the existence of parabolic sample flow. This is that it places some portion (perhaps less than 10%) of the accepted sample volume in a region near the edge of the laser beam where droplet diameters may be underestimated by as much as 20%. Dye and Baumgardner, Cerni (1983), and others discuss this artificial droplet broadening by the FSSP which appears to be related to laser beam inhomogeneities and to loss of scattered

power away from the beam center. No attempt is made to address this effect on the measurements of cloud droplet diameters and dispersion in this study, except for calibration tests of the broadening effect on distributions of non-water particles of known diameters. This is the subject of Appendix C.

Other Potential Uncertainties

Other sources of error in measuring cloud droplet concentrations with the FSSP-100 are minimized by the sampling system employed. These include potential coincidence error and what are referred to as dead-time errors. The manufacturer does not recommend using the FSSP when particle transit rates (s^{-1}) exceed 100 KHz. The existence of coincidence errors under these circumstances have been discussed, verified, and quantified by Dye and Baumgardner (1984) and Baumgardner et al. (1985). Typical transit rates in the experiments performed in the dynamic cloud chamber are approximately less than or equal to 1 KHz. Thus, coincidence errors are negligible. "Dead-time" refers to the period when the FSSP is not measuring because of electronic housekeeping. A careful calculation of errors in measuring droplet concentration because of this inactive time requires measurement of various delay times as described by Baumgardner et al. (1985). This is probably not necessary due to the small magnitude of the error compared to uncertainties described previously. A typical average transit time for particles in the CSU sampling system is about 6 μs . This is nearly the same value as the typical "slow" delay time of an FSSP. Therefore, few particles should be missed during delays. As a maximum estimate of error, the typical cumulative dead-time over 1 second for an FSSP recording 1000 total strobes per second (typical value in most

experiments) is about 0.005 s. Thus, maximum dead-time losses probably did not exceed 0.5% in the experiments performed.

References

- Baumgardner, D., B. Baker, and K. Weaver, 1993: A technique for the measurement of cloud structure on centimeter scales. *J. Atmos. Ocean. Technol.*, **10**, 557-565.
- D. Baumgardner, W. Strapp, and J.E. Dye 1984: Evaluation of the Forward Scattering Spectrometer Probe: Part II. Corrections for coincidence and dead-time losses. *J. Atmos. Ocean. Technol.*, **1**, 329-344.
- Brenguier J-L., A.R. Rodi, G. Gordon, and P. Wechsler, 1993: Real-time detection of performance degradation of the Forward-Scattering Spectrometer Probe. *J. Atmos. Ocean. Technol.*, **10**, 27-33.
- Cerni, T.A., 1983: Determination of size and concentration of cloud drops with an FSSP. *J. Clim. Appl. Meteor.*, **22**, 1346-1355.
- DeMott, P.J. and D.C. Rogers, 1990: Freezing nucleation rates of dilute solution droplets measured between -30 and -40C in laboratory simulations of natural clouds. *J. Atmos. Sci.*, **47**, 1056-1064.
- Dye, J.E. and D. Baumgardner, 1984: Evaluation of the Forward Scattering Spectrometer Probe: Part I. Electronic and optical studies. *J. Atmos. Ocean. Technol.*, **1**, 329-344.
- Knudsen, J.G. and D.L. Katz, 1979: *Fluid Dynamics and Heat Transfer*. Robert E. Krieger Publishing, Huntington, NY, 576 pp.
- Vincent, J.H., 1989: *Aerosol Sampling: Science and Practice*. John Wiley and Sons, Chichester, 390 pp.

APPENDIX C
FSSP CALIBRATIONS

(Contributed by Paul J. DeMott)

Recalibration

The FSSP was recalibrated at the conclusion of the experimental program described in the body of this thesis. This calibration was performed following the recommendations of PMS by drawing glass beads of different known sizes through the sampling inlet. Knowing the differences between the indices of refraction of water and glass, the expected peak diameter of the beads as measured by the FSSP (assuming they are water) is provided by the manufacturer. As the results given here will show, differences were found which imply that the FSSP was undersizing particles exceeding about 10 μm in diameter during the research program. Since the last documented calibration occurred in 1987, it is assumed that this measurement degradation occurred over time and was approximately at the same level of error in the three months preceding the calibration in August 1993. Dr. Darrel Baumgardner of the National Center for Atmospheric Research provided computer code which was used to recalculate droplet bin diameters based on the calibration data. This recalibration is described here following the presentation of calibration test procedures and results. The glass bead calibrations were supplemented by FSSP bench tests of two sizes of polystyrene latex beads. The standard deviation of these latex beads were narrower than for the glass beads and were well characterized by the manufacturer, so these tests also provided an opportunity to estimate the magnitude of the artificial broadening effect of the FSSP. This was important in understanding differences between the experimentally measured dispersion of the cloud droplet distribution and the dispersion expected based on numerical model calculations.

Glass bead tests were conducted by mounting the FSSP in a vertical position on a laboratory bench. Flow rate through the sample system was controlled to be the same as for cloud chamber operations. The beads were manufactured by Particle Information Services, Incorporated, the company recommended in the FSSP manual. Beads were specified to be within a range of sizes rather than a single size. Verification that modal diameter was within the specified ranges was made with an optical microscope, but detailed size distribution measurements were not made. Little variation between batches of these beads has been noted by regular users of these calibration beads (personal communication with Dr. Darrel Baumgardner). The bead size categories used were 3 to 9 μm , 10 to 15 μm , 15 to 25 μm , and 25 to 35 μm . Most tests were done using range 1 of the FSSP since most measurements were taken in this size range and since this is the recommended range setting for calibration. Nevertheless, some data were collected in all range settings. PMS calibration points for these beads sized are shown in Figure C.1, as copied from the FSSP manual (Serial No. 28).

The size distributions measured by the FSSP for glass beads in size range 1 (2-32 μm) are shown in Figures C.2 to C.5. At least two tests were conducted for each bead sample. Each individual test consisted of using a VCR head cleaning swab to gather beads and to disperse them above the sampling inlet with a flicking motion. This was done several times within each recorded test. Then the data were accumulated to obtain the size distributions shown. It is clear that rather broad spectra exist for the bead samples and that the peak sizes are mostly less than as specified by PMS for a properly calibrated probe. Although this implies that the probe is somewhat undersizing currently, possibly due to a decrease in scattered power due to dirty optics, no guidance is provided by PMS as to how to correct for noted calibration errors. Cerni (1983) used a single "scale factor" for each probe range to redefine the mie-scattered power versus

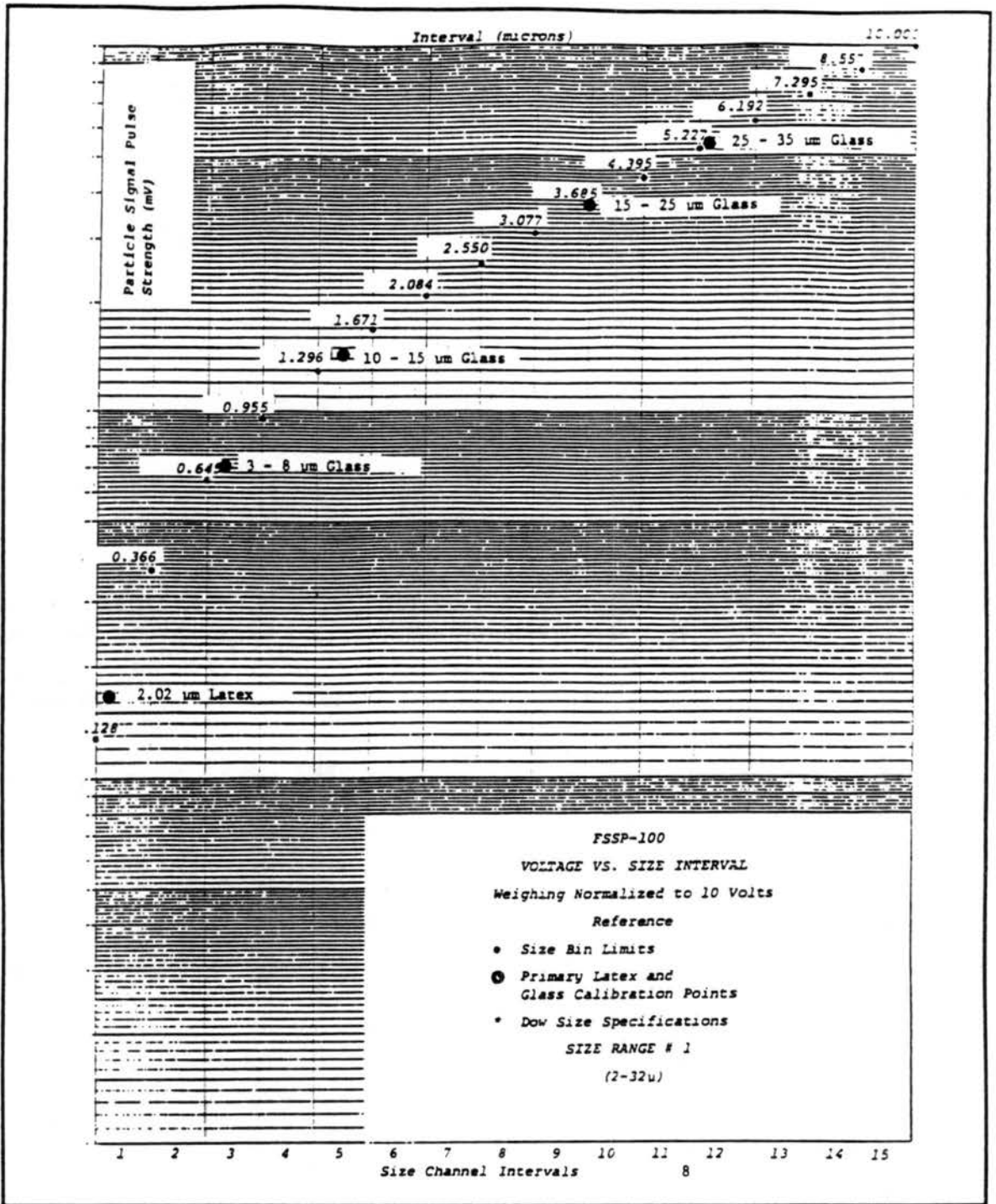


Figure C.1. Original bin size definitions on FSSP range 1 for probe Serial Number 28, from the manual. Bin limits are defined by the particle signal pulse strength.

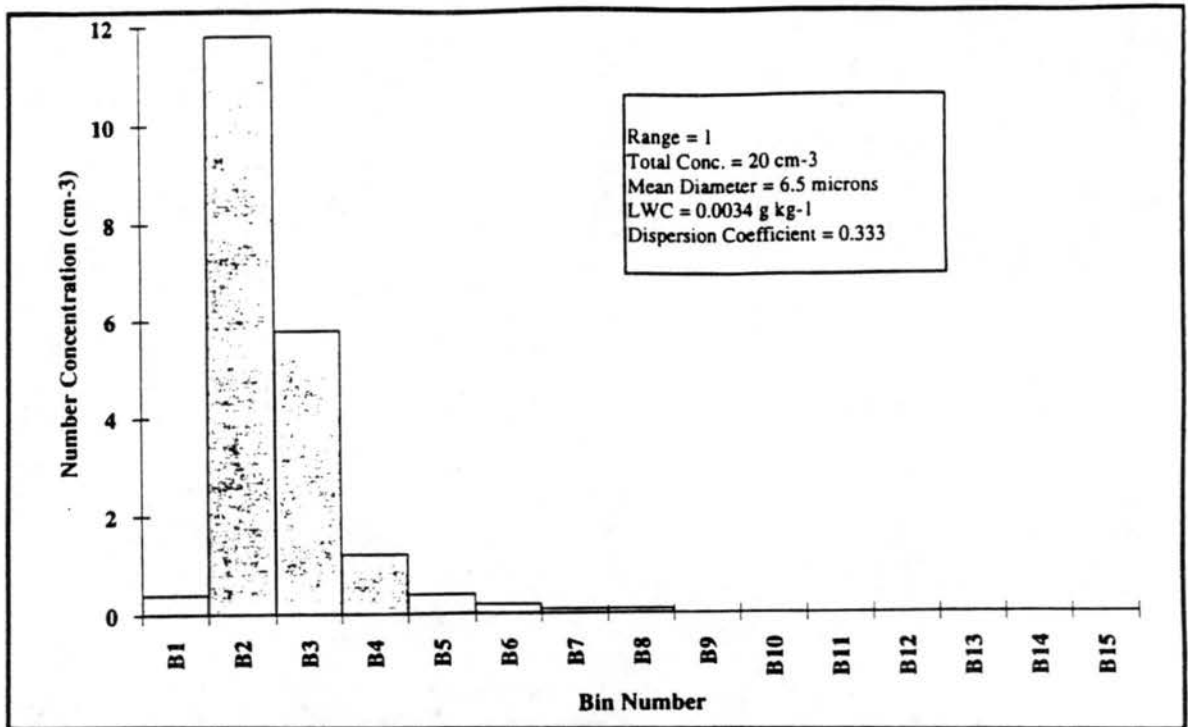


Figure C.2. Droplet size distribution measured for 3 to 9 μm glass beads (range 1).

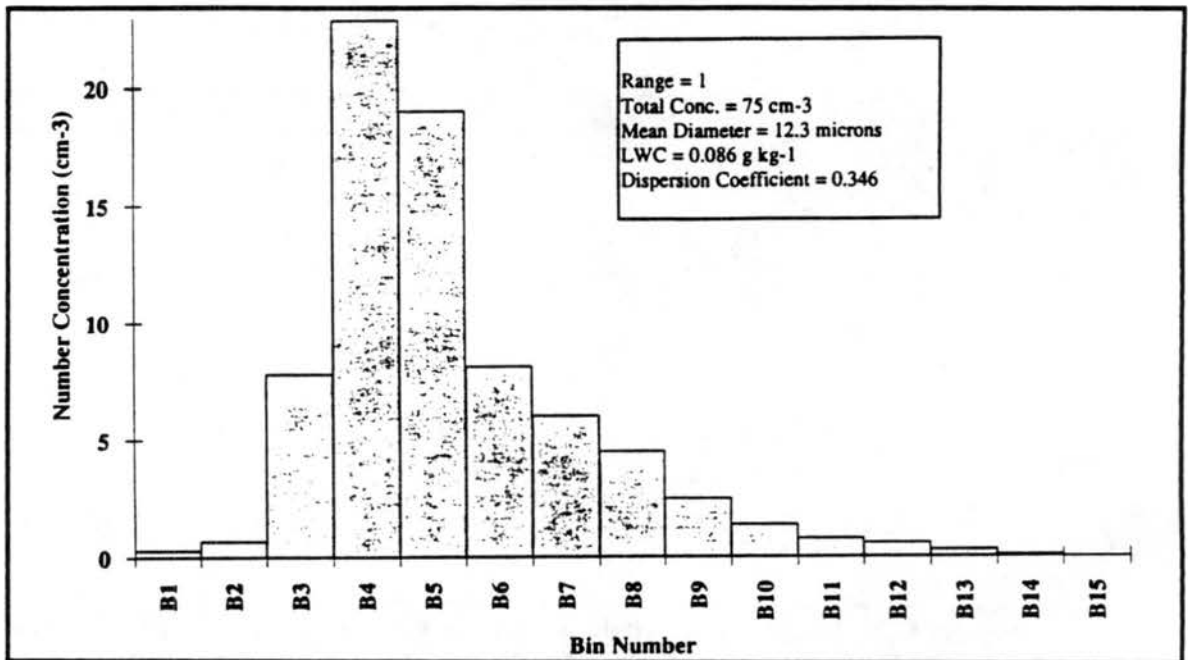


Figure C.3. Droplet size distribution measured for 10 to 15 μm glass beads (range 1).

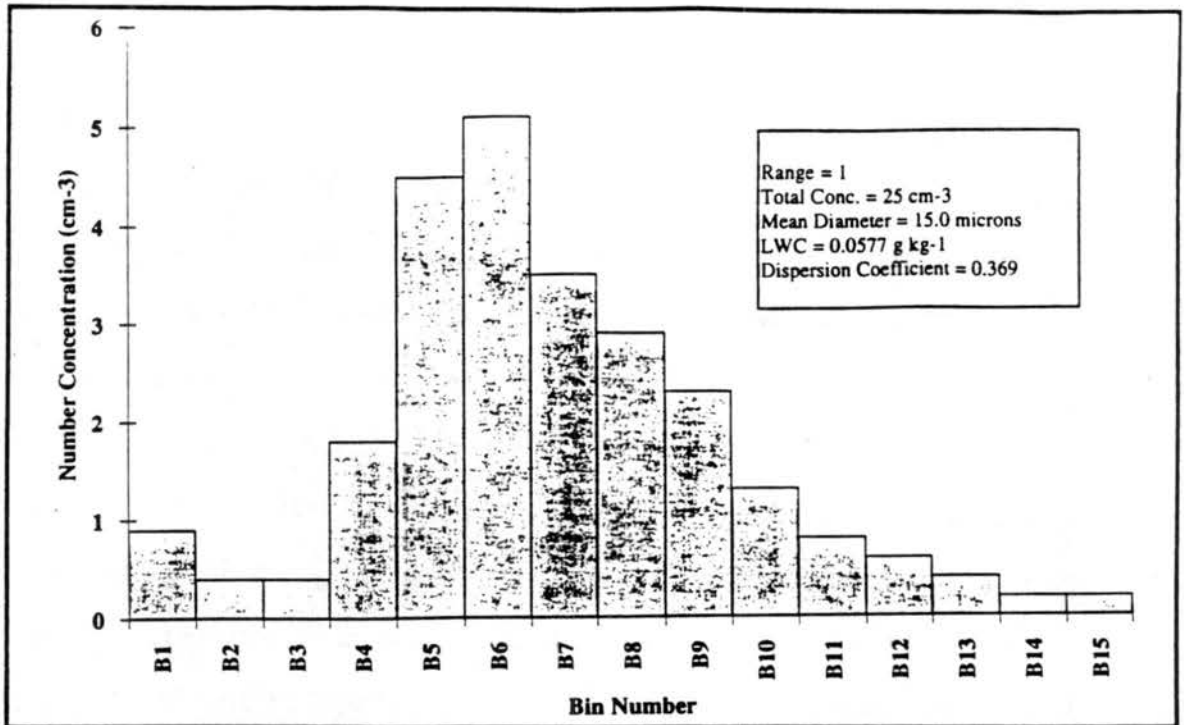


Figure C.4. Droplet size distribution measured for 15 to 25 μm glass beads (range 1).

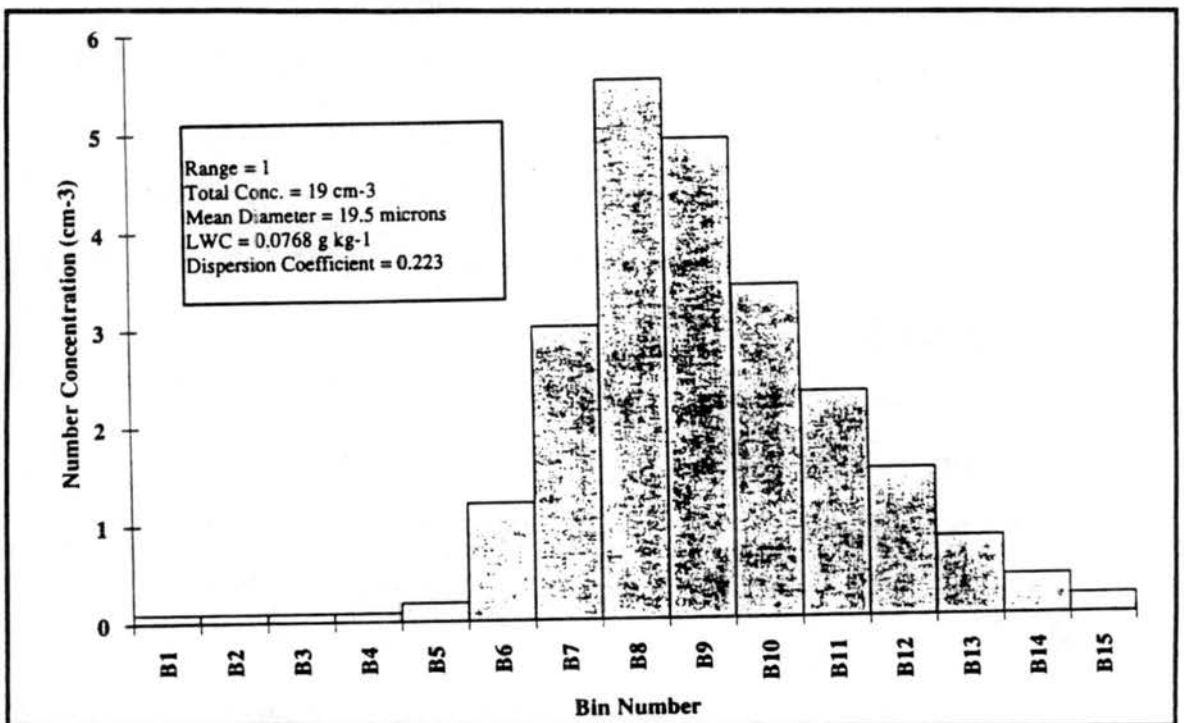


Figure C.5. Droplet size distribution measured for 25 to 35 μm glass beads (range 1).

FSSP voltage relationship. The measured pulse height analyzer (PHA) voltage levels then define the size limits of bins. This procedure is the basis for a computer program provided by Dr. Darrel Baumgardner of NCAR to facilitate recalibration.

The calibration program first determines the equivalent droplet size for a given glass bead size by searching through tables of mie-scattered power generated based on the laser wavelength and the index of refraction of the appropriate particle. The scale factor is determined as the ratio of the mie power to the FSSP voltage for the calibration particle. This factor is applied to each PHA voltage to define size bin limits from the mie table. A range in the size of each bin limit is determined where multiple mie values are possible. Although the measured PHA voltages should be used in this procedure, only small differences between manufacturer specified values and measured values have ever been noted in past studies. Manufacturer values were used in this recalibration. The average glass bead sizes used for calibrations were 6.4 μm , 11.4 μm , 20.6 μm , and 30 μm . The average size of the smallest beads were previously estimated at the CSU laboratory, the next two sizes were taken from Cerni (1983), and the largest is simply the midpoint of the largest bead sample size tested. There were very few of the 20.6 μm bead size available for calibration.

Calibration results for FSSP range 1 are given in Tables C.1 to C.4. The channel numbers listed give the uncertainty in the size of the bin limits. The results for the first two bead sizes were quite consistent and indicate only slight undersizing for particles smaller than 15 μm . The larger bead calibration results suggest marked undersizing if using the manufacturer-specified bin sizes. Tests on FSSP ranges 2 and 3 (Tables C.5 to C.7) confirmed the consistent results obtained for the smallest beads, again indicating only slight undersizing of droplets smaller than 15 μm .

Calibration data were also collected for latex beads with manufacturer-specified mean diameters of 2.97 (+/-0.037) μm and 11.9 (+/-1.9) μm . The beads were generated using a TSI Model 9306 Six Jet Atomizer after dilution with specification-grade water. It was necessary to place the probe in a horizontal bench orientation for these tests. The latex bead size distributions on FSSP range 1 are shown in Figures C.6 and C.7. The recalibration results for the 3 μm latex beads (Tables C.8, 10, 11) were extremely consistent with the smaller glass bead results across ranges 1 to 3 of the probe. This was reassuring. However, the 12 μm latex bead results (Table C.9) actually suggest slight oversizing by the FSSP. This contradicts the results obtained for glass beads in this size range. This is confusing and unresolved at this time.

Given the balance of evidence obtained, the FSSP in its current operating condition is undersizing most sizes of cloud droplets. The data obtained can be used to reconfigure the measured size bin limits into corrected bin limits and thereby recompute cloud quantities such as average diameter and dispersion. The effect would be very small for droplets less than 15 μm diameter.

Artificial Broadening of Droplet Spectra by the FSSP

The latex bead test results provided a measure of the artificial broadening of cloud droplet spectra by the FSSP. In order to estimate the artificial contribution to broadening, the mean and standard deviation values quoted for the latex beads were used to produce a relative size distribution for each FSSP size range used for calibration. The standard bin limits specified for the FSSP were used to define this distribution. A more exact method would use the new bin limits determined by calibration to define the actual FSSP latex bead distributions. However, since the calibration corrections were not

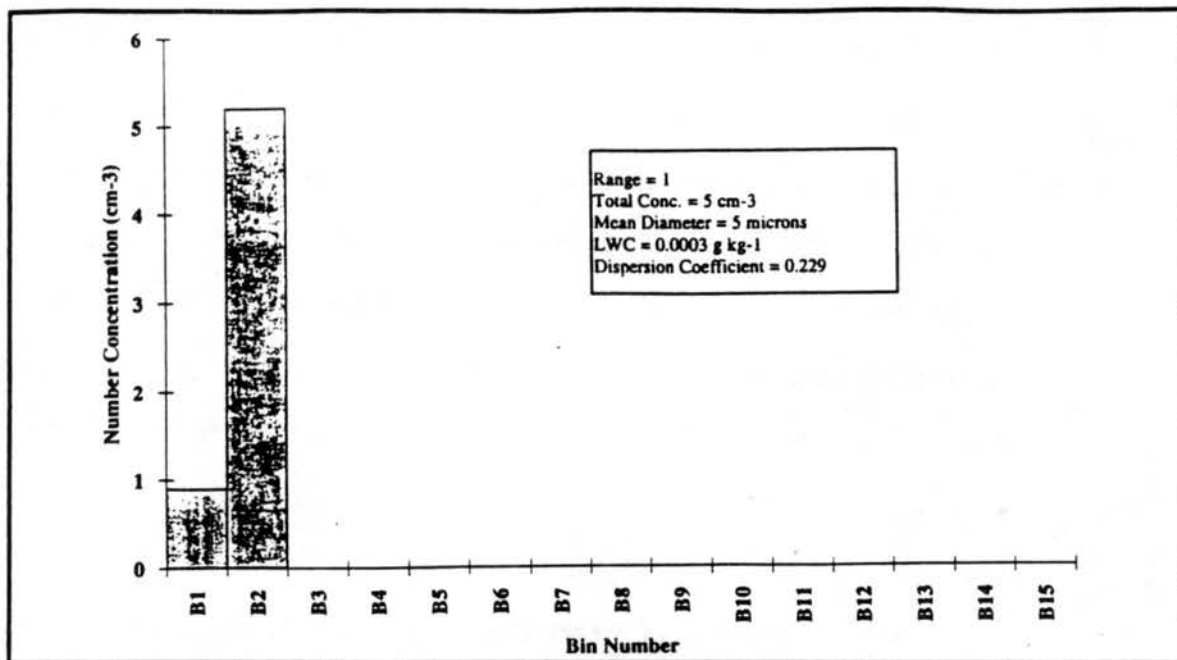


Figure C.6. Droplet size distribution measured for 2.97 μm latex beads (range 1).

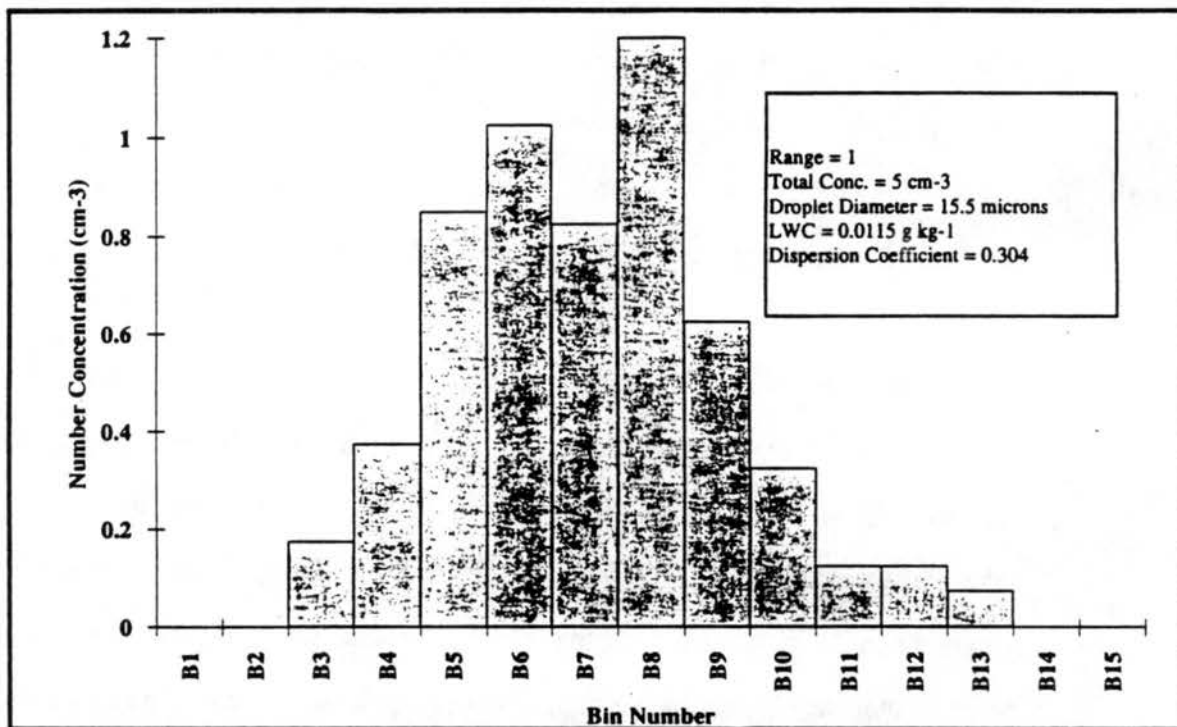


Figure C.7. Droplet size distribution measured for 11.9 μm latex beads (range 1).

Tables C.1 to C.2:
Calibration Test Results for Glass Beads (sizes in μm)

Table C.1

Bead Size = 6.4
Equivalent Size = 6.0 @ n = 1.33
FSSP Range = 1
Mean Channel # of Bead Calibration = 3.0

Ch. #1	1.5 - 2.6
Ch. #2	2.9 - 4.5
Ch. #3	5.1 - 7.2
Ch. #4	8.2 - 9.6
Ch. #5	9.9 - 11.2
Ch. #6	11.5 - 12.8
Ch. #7	13.4 - 14.9
Ch. #8	16.3 - 17.7
Ch. #9	18.1 - 18.1
Ch. #10	20.1 - 20.1
Ch. #11	22.0 - 22.0
Ch. #12	24.7 - 24.7
Ch. #13	26.9 - 28.3
Ch. #14	28.8 - 31.1
Ch. #15	32.7 - 53.1
Ch. #16	33.0 - 53.1

Table C.2

Bead Size = 11.4
Equivalent Size = 10.6 @ n = 1.33
FSSP Range = 1
Mean Channel # of Bead Calibration = 5.2

Ch. #1	1.6 - 2.6
Ch. #2	2.9 - 4.5
Ch. #3	5.2 - 9.2
Ch. #4	8.2 - 9.6
Ch. #5	9.9 - 11.2
Ch. #6	11.5 - 12.9
Ch. #7	13.5 - 15.0
Ch. #8	16.4 - 17.7
Ch. #9	18.1 - 19.4
Ch. #10	20.2 - 20.2
Ch. #11	22.0 - 23.0
Ch. #12	24.8 - 25.9
Ch. #13	28.4 - 28.4
Ch. #14	28.9 - 31.2
Ch. #15	32.8 - 53.1
Ch. #16	33.0 - 53.1

Tables C.3 to C.4:
Calibration Test Results for Glass Beads (sizes in μm)

Table C.3

Bead Size = 20.6
 Equivalent Size = 18.0 @ n = 1.33
 FSSP Range = 1
 Mean Channel # of Bead Calibration = 7.3

Ch. #1	2.6 - 2.6
Ch. #2	3.0 - 4.7
Ch. #3	7.8 - 9.4
Ch. #4	9.8 - 11.0
Ch. #5	11.4 - 12.7
Ch. #6	13.5 - 15.0
Ch. #7	16.4 - 17.7
Ch. #8	18.2 - 19.7
Ch. #9	20.3 - 21.5
Ch. #10	22.1 - 23.3
Ch. #11	25.1 - 26.2
Ch. #12	28.5 - 28.5
Ch. #13	29.1 - 53.0
Ch. #14	32.9 - 53.1
Ch. #15	33.1 - 54.4
Ch. #16	39.4 - 54.7

Table C.4

Bead Size = 30.0
 Equivalent Size = 25.4 @ n = 1.33
 FSSP Range = 1
 Mean Channel # of Bead Calibration = 9.0

Ch. #1	2.7 - 2.7
Ch. #2	5.1 - 7.2
Ch. #3	9.7 - 11.0
Ch. #4	11.5 - 12.9
Ch. #5	13.7 - 15.2
Ch. #6	18.0 - 18.0
Ch. #7	20.1 - 20.1
Ch. #8	22.0 - 23.0
Ch. #9	24.9 - 26.0
Ch. #10	28.5 - 28.5
Ch. #11	29.0 - 53.0
Ch. #12	32.9 - 53.1
Ch. #13	33.2 - 54.4
Ch. #14	39.5 - 56.1
Ch. #15	42.0 - 56.2
Ch. #16	45.0 - 56.3

Tables C.5 to C.6:
 Calibration Test Results for Glass Beads (sizes in μm)

Table C.5

Bead Size = 6.4
 Equivalent Size = 6.0 @ $n = 1.33$
 FSSP Range = 2
 Mean Channel # of Bead Calibration = 5.0

Ch. #1	1.0 - 1.0
Ch. #2	2.6 - 2.6
Ch. #3	2.8 - 4.3
Ch. #4	3.0 - 4.7
Ch. #5	5.0 - 7.2
Ch. #6	7.8 - 9.4
Ch. #7	9.6 - 9.6
Ch. #8	9.8 - 11.0
Ch. #9	10.0 - 11.2
Ch. #10	11.4 - 12.5
Ch. #11	13.2 - 13.2
Ch. #12	13.5 - 15.0
Ch. #13	13.7 - 15.6
Ch. #14	16.4 - 17.7
Ch. #15	16.7 - 18.0
Ch. #16	18.2 - 19.5

Table C.6

Bead Size = 11.4
 Equivalent Size = 10.6 @ $n = 1.33$
 FSSP Range = 2
 Mean Channel # of Bead Calibration = 9.0

Ch. #1	1.0 - 1.0
Ch. #2	2.6 - 2.6
Ch. #3	2.8 - 4.3
Ch. #4	3.0 - 4.7
Ch. #5	5.0 - 7.2
Ch. #6	7.8 - 9.4
Ch. #7	9.6 - 9.6
Ch. #8	9.8 - 11.0
Ch. #9	10.0 - 11.2
Ch. #10	11.4 - 12.5
Ch. #11	13.2 - 13.2
Ch. #12	13.5 - 15.0
Ch. #13	13.7 - 15.6
Ch. #14	16.4 - 17.7
Ch. #15	16.7 - 18.0
Ch. #16	18.2 - 19.5

Table C.7:
Calibration Test Results for Glass Beads (sizes in μm)

Table C.7
Bead Size = 6.4
Equivalent Size = 6.0 @ $n = 1.33$
FSSP Range = 3
Mean Channel# of Bead Calibration = 10.5

Ch. #1	0.7 - 0.7
Ch. #2	1.0 - 1.0
Ch. #3	1.3 - 2.5
Ch. #4	2.6 - 2.6
Ch. #5	2.7 - 2.7
Ch. #6	2.8 - 4.3
Ch. #7	2.8 - 4.4
Ch. #8	2.9 - 4.5
Ch. #9	3.0 - 4.7
Ch. #10	3.2 - 7.0
Ch. #11	5.0 - 7.2
Ch. #12	5.6 - 9.3
Ch. #13	7.7 - 9.4
Ch. #14	8.0 - 9.5
Ch. #15	8.2 - 9.6
Ch. #16	9.7 - 9.7

Tables C.8 to C.9:
 Calibration Test Results for Polystyrene Latex Beads (sizes in μm)

Table C.8

Bead Size = 3.0
 Equivalent Size = 3.7 @ $n = 1.33$
 FSSP Range = 1
 Mean Channel # of Bead Calibration = 1.9

Ch. #1	1.5 - 2.5
Ch. #2	2.9 - 4.5
Ch. #3	5.0 - 7.2
Ch. #4	8.2 - 9.5
Ch. #5	9.8 - 11.1
Ch. #6	11.4 - 12.7
Ch. #7	13.4 - 14.8
Ch. #8	15.4 - 17.6
Ch. #9	18.1 - 18.1
Ch. #10	20.0 - 20.0
Ch. #11	22.0 - 22.0
Ch. #12	23.7 - 24.2
Ch. #13	26.7 - 28.2
Ch. #14	28.7 - 31.1
Ch. #15	30.8 - 53.1
Ch. #16	33.0 - 53.1

Table C.9

Bead Size = 11.9
 Equivalent Size = 10.6 @ $n = 1.33$
 FSSP Range = 1
 Mean Channel # of Bead Calibration = 7.0

Ch. #1	1.3 - 2.5
Ch. #2	2.7 - 4.1
Ch. #3	3.0 - 4.6
Ch. #4	5.1 - 7.2
Ch. #5	7.9 - 9.5
Ch. #6	9.7 - 11.0
Ch. #7	10.0 - 11.2
Ch. #8	11.5 - 12.9
Ch. #9	13.4 - 14.9
Ch. #10	15.4 - 17.6
Ch. #11	18.0 - 18.0
Ch. #12	18.4 - 19.9
Ch. #13	20.5 - 22.0
Ch. #14	22.3 - 23.5
Ch. #15	26.4 - 26.4
Ch. #16	28.6 - 29.9

Tables C.10 to C.11:
 Calibration Test Results for Polystyrene Latex Beads (sizes in μm)

Table C.10

Bead Size = 3.0
 Equivalent Size = 3.7 @ $n = 1.33$
 FSSP Range = 2
 Mean Channel # of Bead Calibration = 3.9

Ch. #1	1.0 - 1.0
Ch. #2	1.6 - 2.6
Ch. #3	2.7 - 4.1
Ch. #4	2.9 - 4.5
Ch. #5	3.1 - 6.7
Ch. #6	5.2 - 9.2
Ch. #7	7.8 - 9.4
Ch. #8	8.3 - 9.6
Ch. #9	9.7 - 11.0
Ch. #10	9.9 - 11.2
Ch. #11	11.4 - 11.4
Ch. #12	11.5 - 13.0
Ch. #13	13.2 - 13.2
Ch. #14	13.5 - 15.2
Ch. #15	13.9 - 15.6
Ch. #16	16.4 - 17.7

Table C.11

Bead Size = 3.0
 Equivalent Size = 3.7 @ $n = 1.33$
 FSSP Range = 3
 Mean Channel # of Bead Calibration = 7.9

Ch. #1	0.7 - 0.7
Ch. #2	1.0 - 1.0
Ch. #3	1.3 - 2.4
Ch. #4	1.6 - 2.6
Ch. #5	2.6 - 2.6
Ch. #6	2.8 - 4.1
Ch. #7	2.8 - 4.4
Ch. #8	2.9 - 4.5
Ch. #9	3.0 - 4.6
Ch. #10	3.1 - 6.7
Ch. #11	4.9 - 7.2
Ch. #12	5.2 - 9.2
Ch. #13	7.6 - 9.4
Ch. #14	7.9 - 9.5
Ch. #15	8.1 - 9.5
Ch. #16	9.6 - 9.6

applied to the data presented in this thesis, using the PMS size bins seemed most consistent. Then, the mie program was used to predict the mean diameter and standard deviation of the relative size distribution expected for water droplets. Table C.12 summarizes the actual, predicted and measured mean diameters, standard deviations, and dispersions for the 3 and 11.9 μm latex beads. For example, the 11.9 μm beads have an actual dispersion of 0.16, but are predicted to have a dispersion of 0.20 when measured as water droplets. The actual measured dispersion for these beads on FSSP range 1 is approximately 0.30. Thus, the instrument artificially introduces 0.10 to the measured dispersion. Very nearly the same result was found for the small latex beads. Following Cerni (1983), the square of the instrumentally-introduced standard deviation may be considered to be the difference between the squares of the measured and predicted standard deviations, respectively. The instrumental standard deviation inferred for the larger particles is thus about 4.1 μm . This value is probably exaggerated because the measured diameter is so much larger than predicted. Cerni measured $S_{\text{inst}} = 2$ to 3 μm for similar sized glass beads. For smaller droplets, the instrumental standard deviation measured was about 0.65 μm .

Table C.12.

Latex Bead Test Diameter, Dispersion, and Standard Deviation

Mean Droplet Diameter			Standard Deviation			Dispersion Coefficient		
Actual	Pred.	Meas	Actual	Pred.	Meas	Actual	Pred.	Meas
2.97	3.60	4.40	0.037	0.048	0.572	0.013	0.013	0.13
11.9	10.6	15.3	1.900	2.400	5.400	0.160	0.200	0.30

References

- Cerni, T.A., 1983: Determination of size and concentration of cloud drops with an FSSP.
J. Clim. Appl. Meteor., **22**, 1346-1355.

APPENDIX D

DIFFERENTIAL MOBILITY PARTICLE SIZER THEORY

Generation of Mobility Distribution

The work of Hoppel (1978), and the data reduction technique developed by Fissan et al. (1983) were used by TSI (Thermo Systems, Inc., St Paul, MN) to develop the data inversion software used by the Differential Mobility Particle Sizing (DMSP) system. The approximation of the bipolar charge distribution used in the data inversion was taken by TSI from the work of Wiedensohler (1986) and Wiedensohler and Fissan (1988).

Hoppel (1978) summarized the work of Knutson and Whitby (1975), who described an electric mobility analyzer where the charged fraction of aerosols is separated from the sample by an electric field and removed from the instrument in a sheath air flow. The equations included in this section are those presented in Hoppel's paper and are repeated here as a basis for the data inversion described later.

Figure D.1 shows a schematic of the mobility chamber of a differential mobility analyzer (DMA). The sheath air flow is denoted by ϕ_1 , the polydisperse air flow by ϕ_2 , the monodisperse air flow by ϕ_3 , and the excess air flow by ϕ_4 . The flow in the chamber must be laminar for the following equations to apply. The critical mobilities of a charged particle must follow the trajectories (dashed lines) depicted in Figure D.1. These trajectories are represented by k_1 , k_2 , k_3 , k_4 . The critical mobilities are a function of chamber parameters and are given by:

$$k_1 = \frac{\phi_1 + \phi_2 - \phi_3}{4\pi cv} \quad (D.1a)$$

$$k_2 = \frac{\phi_1 + \phi_2}{4\pi cv} \quad (D.1b)$$

$$k_3 = \frac{\phi_1 - \phi_3}{4\pi cv} \quad (D.1c)$$

$$k_4 = \frac{\phi_1}{4\pi cv} \quad (D.1d)$$

where c is the electrical capacitance between the inner and outer cylinder and v is the voltage between the cylinders. A mobility, k , that is the envelope created by trajectories for k_1 and k_3 will be collected as well as those between k_2 and k_4 . Therefore, if

$$k_3 < k < k_1$$

or

$$k_4 < k < k_2$$

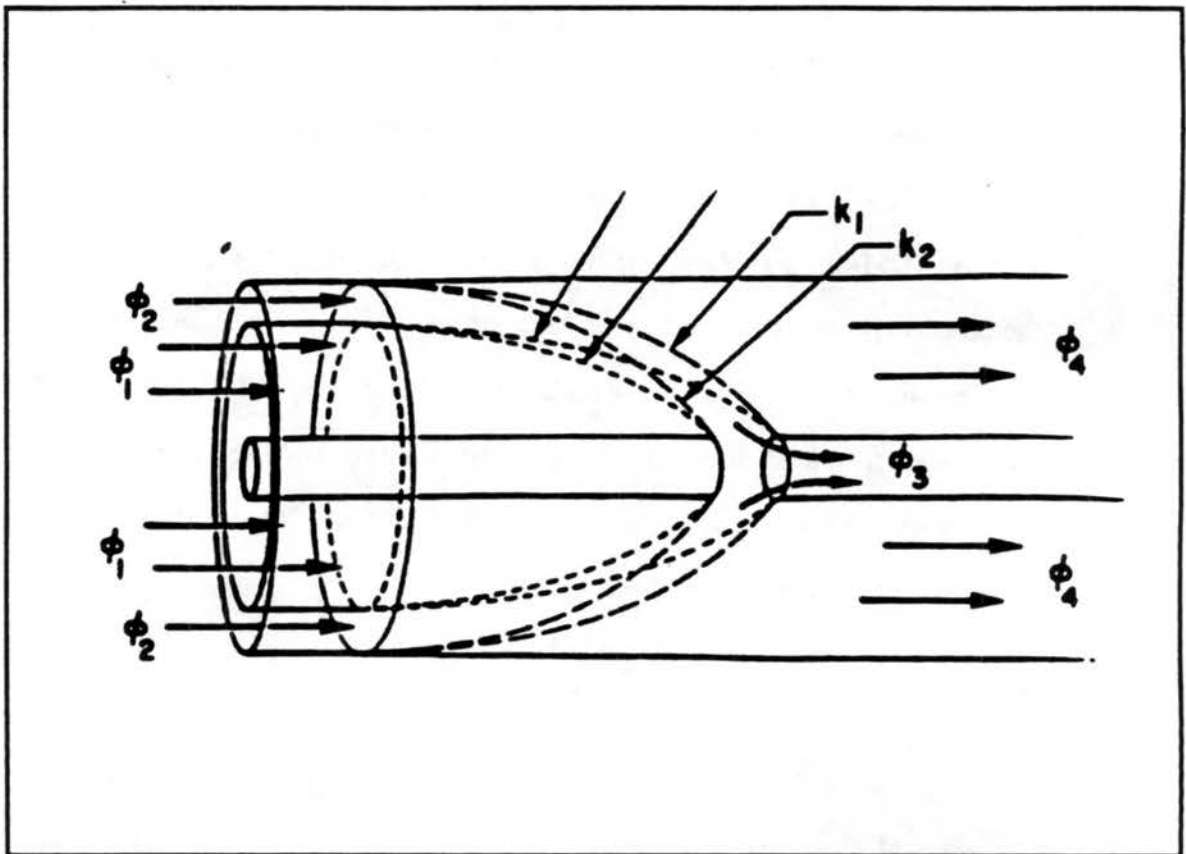


Figure D.1 Schematic of the Critical Mobilities of a Charged Particle in the DMA Chamber. (Hoppel, 1978)

the particle with mobility k will be collected and leave the chamber in flow ϕ_3 . The current (number per second) of aerosol leaving the chamber in flow ϕ_3 is given by

$$I(k_1) = \int_{k_3}^{k_1} \left[\frac{k\phi_1}{k_4} - (\phi_1 - \phi_3) \right] f(k) dk + \phi_2 \int_{k_1}^{k_4} f(k) dk + \int_{k_4}^{k_2} \left[(\phi_1 - \phi_2) - \frac{k\phi_1}{k_4} \right] f(k) dk \quad (D.2)$$

where $f(k)$ is the mobility distribution function. When aerosol of a single mobility are present the solution to (D.2) is given by

$$I(k_1) = \left[\frac{k_0\phi_1}{k_4} - (\phi_1 - \phi_3) \right] N_0 \quad \text{if } k_3 < k_0 < k_1 \quad (D.3a)$$

$$I(k_1) = N_0\phi_2 \quad \text{if } k_1 < k_0 < k_4 \quad (D.3b)$$

$$I(k_1) = \left[(\phi_1 + \phi_2) - \frac{k_0\phi_1}{k_4} \right] N_0 \quad \text{if } k_4 < k_0 < k_2 \quad (D.3c)$$

The best mobility resolution occurs when $k_1 = k_4$, which requires the polydisperse air flow to equal the monodisperse air flow, ($\phi_2 = \phi_3$). The other factor affecting the mobility resolution is the rise distance of the mobility space; i.e. the mobility interval between the peak signal and where the signal vanishes. When $\phi_2 = \phi_3$, the relative rise distance is proportional to

$$R = \frac{k_1 - k_3}{k_1} = \frac{k_2 - k_1}{k_1} = \frac{\phi_2}{\phi_1} \quad (D.4)$$

Also when $\phi_2 = \phi_3$, (D.2) reduces to

$$I(k_1) = \int_{k_2}^{k_1} \left[\frac{k\phi_1}{k_1} - (\phi_1 - \phi_2) \right] f(k) dk + \int_{k_1}^{k_2} \left[(\phi_1 + \phi_2) - \frac{k\phi_1}{k_1} \right] f(k) dk \quad (D.5)$$

If the polydisperse flow is much less than the sheath air flow, the interval of integration in (D.5) is small and $f(k)$ can be approximated as $\overline{f(k)}_{k_2, k_1}$ by the mean value theorem.

Integration of (D.5) give the following relation

$$\frac{I(k_1)}{\phi_2} = \frac{\phi_2}{\phi_1} k_1 \overline{f(k)}_{k_2, k_1} \quad (D.6)$$

The total number of particles if found by integrating $\overline{f(k)}_{k_2, k_1}$. If $R = 0.1$ ($\phi_1 = 10\phi_2$), the error in the integrated value is only about one part in 600.

Conversion of Mobility Distribution to Size Distribution

If there were only singly charged particles moving through the DMA, the conversion from mobility to size distributions would be simple. However, the charger used in the DMA produces singly as well as multiply charged particles. Systematic approximations must be used in order to unravel the pattern of multiply charged particles. Hoppel (1978) details the equations used to convert a mobility distribution to a particle size distribution. If $k(r)$ is the mobility of a singly charged particle of radius r , the mobility of a particle with p -charges is

$$pk(r) = \frac{p}{6\pi\eta r} \left(\frac{e}{300} \right) \left\{ 1 + \frac{L}{r} \left[A + B \exp\left(-\frac{Cr}{L}\right) \right] \right\} \quad (D.7)$$

where p is the number of elementary charges of magnitude e , A , B , and C are constants determined empirically, r is the radius, η is the kinematic viscosity of air, and L is the

mean free path. The units of this equation has units of $\text{cm}^2 \text{V}^{-1} \text{s}^{-1}$, e is in e.s.u., and all other quantities are in c.g.s. units.

The total number density of aerosols of radius r without regard to the charge is denoted by Z and calculated using

$$Z(r) = N_0(r) + 2 \sum_{p=1}^{\infty} N^p(r) \quad (\text{D.8})$$

The charge distribution on aerosols of radius r is given by

$$N^p(r) = N_0(r) \exp\left(-\frac{p^2 e^2}{2rKT}\right) \quad (\text{D.9})$$

where $N^p(r)$ is the number of particles carrying p -elementary charges, $N_0(r)$ is the number density of unchanged aerosols, K is Boltzmann's constant and T is the temperature. Combining equation (D.8) and (D.9) gives

$$Z(r) = \frac{N^p(r)}{R_p(r)} \left[1 + 2 \sum_{p=1}^{\infty} R_p(r) \right] \quad (\text{D.10})$$

which is the total number density of aerosols with p -elemental charges, where

$$R_p(r) = \exp\left(-\frac{p^2 e^2}{2rKT}\right) \quad (\text{D.11})$$

The number of charged aerosol in the mobility range $(k_{j+1} - k_j)$ can be written as

$$\Delta N(k_{j+1} - k_j) = \Delta N^{(1)}(k_{j+1} - k_j) + \Delta N^{(2)}\left(\frac{k_{j+1}}{2} - \frac{k_j}{2}\right) + \dots + \Delta N^{(p)}\left(\frac{k_{j+1}}{p} - \frac{k_j}{p}\right) \quad (\text{D.12})$$

where $\Delta N^p(k_{j+1}/p - k_j/p)$ is the number of charges in the mobility range $(k_{j+1} - k_j)$ characterized by a mobility range expected by an equivalent single charge mobility range.

To begin the inversion process from mobility distribution to size distribution, a first order approximation that assumes all charged aerosols in the mobility interval are singly charge is used. The equation for this approximation is

$$\Delta^1 N^{(1)}[r(k_{j+1}) - r(k_j)] = \Delta N[r(k_{j+1}) - r(k_j)] \quad (D.13)$$

where the Roman numeral denotes the first order approximation. $\Delta N[r(k_{j+1}) - r(k_j)]$ is obtained from the measured DMA mobility distribution function. The first order size distribution is then obtained from equation (D.10) by calculating $\Delta^1 Z$ for each mobility interval using

$$\Delta^1 Z[r(k_{j+1}) - r(k_j)] = \left[\left(1 + 2 \sum_{p=1}^{\infty} R_p(\bar{r}_j) \right) / R_1(\bar{r}_j) \right] \Delta^1 N^{(1)}[r(k_{j+1}) - r(k_j)] \quad (D.14)$$

where r_j is the size corresponding to the average mobility of the $(k_{j+1} - k_j)$ interval. For higher order approximations, the contribution of multiply charged aerosols is considered. For example the second order approximation of the mobility and, eventually, the size distribution are given as

$$\Delta^2 N^{(1)}[r(k_{j+1}) - r(k_j)] = \Delta N[r(k_{j+1}) - r(k_j)] - \Delta^1 N^{(2)} \left[r\left(\frac{k_{j+1}}{2}\right) - r\left(\frac{k_j}{2}\right) \right] + \dots + \quad (D.15)$$

and

$$\Delta^2 Z[r(k_{j+1}) - r(k_j)] = \left[\left(1 + 2 \sum_{p=1}^{\infty} R_p(\bar{r}_j) \right) / R_1(\bar{r}_j) \right] \Delta^2 N^{(1)}[r(k_{j+1}) - r(k_j)] \quad (D.16)$$

where $\Delta^1 N^p$ is the first order approximation of (D.10) and is given by

$$\Delta^1 N^{(p)} \left[r \left(\frac{k_{j+1}}{p} \right) - r \left(\frac{k_j}{p} \right) \right] = \left[R_p(\bar{r}_j) / \left(1 + 2 \sum_{p=1}^{\infty} R_p(\bar{r}_j) \right) \right] \Delta^1 Z [r(k_{j+1}) - r(k_j)] \quad (D.17)$$

For higher order approximations, the equations (D.15) to (D.17) are repeated using the newly formed ΔZ until convergence of the scheme is within a specified error tolerance.

The TSI DMPS/C system software uses the equations described above to determine the aerosol size distribution measured. The diameter range available for measurement is established by the sheath air or monodisperse air flow chosen for the procedure. An assumption is made by the software that there are no particles larger than the maximum diameter. An impactor is placed in front of the Polydisperse inlet to ensure this assumption is correct. Concentrations measured by a TSI CNC (any model) at the maximum voltage setting, or, in other words, the largest diameter particle, is used by the software to begin the data inversion process. The inversion continues by decreasing size after each convergent iterative calculation. Information provided by the software includes mobility number distribution and size distributions for number, surface area, and volume.

References

- Fissan, H.J., C. Helsper, and H.J. Thielen, 1983: Determination of particle size distribution by means of an electrostatic classifier. *J. Aerosol Sci.*, **14**, 354.
- Hoppel, W. A., 1978: Determination of the aerosol size distribution from the mobility distribution of the charges fraction of aerosols. *J. Aerosol Sci.*, **9**, 41-54.
- Knutson, E.O., and K.T. Whitby, 1975: Aerosol classification by electric mobility: Apparatus theory and applications. *J. Aerosol Sci.*, **6**, 443.

Wiedensohler, A., and H.J. Fissan, 1988: Aerosol charging in high purity gases. *J. Aerosol Sci.*, **19**.

Wiedensohler A., E. Lutkemeier, M. Feldpausch, C. Helsper, 1986: Investigation of the bipolar charge distribution at various gas conditions. *J. Aerosol Sci.*, **17**, 413.

APPENDIX E

CLOUD CHAMBER EXPERIMENTAL PROCEDURES

Aerosol generation

Monodisperse

The DMA, in conjunction with a TSI six-jet atomizer, was used to generate aerosol from 1% by weight solution of ammonium sulfate. Clean, compressed air was supplied to the inlet of the atomizer to generate solution droplets. The dry aerosol then passed through an impactor with a 0.457 μm diameter cutpoint before entering the DMA through the Polydisperse aerosol inlet. The DMA voltage was set to the desired value based on Table E.1, which shows the typical voltages used and the corresponding diameters of monodisperse aerosol generated. The monodisperse aerosol proceeded through the Monodisperse aerosol outlet, which was connected to the injection line through a three-way valve that was initially open to the room.

Table E.1.
DMA Voltage Used to Select Specific Diameter Monodisperse Aerosols

Voltage	Peak Diameter
215 V	0.04 μm
2388 V	0.14 μm
2918 V	0.17 μm
3288 V	0.19 μm

Polydisperse

The one-jet bubbler, containing 0.01 % by weight ammonium sulfate solution, was connected to the MOUDI in an effort to limit the number of particles larger than 0.1 μm injected into the chamber. The MOUDI was set up using seven stages, with the

cutpoint of the final stage being 0.1 μm . The outlet of the MOUDI was connected to the injection line through a three way valve that was initially open to the room.

Polydisperse aerosol with diameters $> 0.14 \mu\text{m}$ was also needed for this study. The six-jet atomizer, containing 1 % by weight ammonium sulfate solution was used to generate the polydisperse aerosol. After the air moves through the molecular sieve dryer, it passed through a three-way valve that was connected to the injection line, but was initially open to the room.

Aerosol Injection

The chamber must be flushed of contaminated ambient air before the injection of the generated aerosol takes place. A filtered, recirculating system was used to obtain background concentrations of less than 0.10 cm^{-3} . The background concentration was monitored throughout the preconditioning phase by a TSI model 3010 CNC. When the concentrations of contaminants approaches 0.10 cm^{-3} , humidity was added to the chamber and the aerosol generation and injection process was started.

The precondition blower circulates room temperature air through the chamber, which was generally warmer than that desired for the experiment. Thus, temperature control was used to hold the inner liner walls at $20 \text{ }^\circ\text{C}$ in an attempt to hold the air temperature as close to $20 \text{ }^\circ\text{C}$ as possible. This procedure resulted in an air temperature of approximately $22 \text{ }^\circ\text{C}$ while the precondition blower was circulating air. When the precondition blower was turned off and the air temperature equilibrated with the wall temperature, the closed volume would cool and shrink. To counteract this vacuum, the chamber was pressurized slightly, thus avoiding possible contamination by ambient air.

The aerosol was injected through a port near the top of the chamber, via a stainless steel probe secured into the port so that it protruded approximately half the diameter of the chamber from the chamber wall, and was mixed through the chamber by the mixing fan. A long, stainless steel injection line ran from the Monodisperse Aerosol outlet to the chamber injection probe. To ensure the line was clean before injecting the generated aerosol, the injection line was flushed for approximately 1 minute with clean, compressed air.

Aerosol was drawn out of a port near the bottom of the chamber through a probe which protrudes from the chamber wall approximately 20 cm. The distance was minimized to avoid thermal conduction into the chamber by the line. The rising concentration in the chamber was monitored, through this sample port, by the CNC. When the CNC displayed the required concentration, the injection process was stopped, and the line was flushed for approximately 1 minute with compressed air. To avoid contamination of the sample in the lower portion of the chamber, the mixing fan was turned off, and the chamber was locked. Once the aerosol was injected into the chamber, verification of size distribution of the aerosol could be done.

Verification of Generated Aerosol Distribution

Immediately after injection, the distribution of the aerosol in the chamber could be measured using the DMPS system. The aerosol was drawn out of the chamber, through the sample port, and through the DMA and CNC using an external vacuum pump. Measurement scans took approximately 20 minutes to complete, not including adjusting the flows required to make the system work, therefore, the injected aerosol may have remained in the chamber for approximately 30 minutes before the expansion began.

Numerous distribution measurements of monodisperse aerosol injected into the chamber were taken over the course of developing the aerosol generation and injection technique. As a result, the monodisperse aerosol generation was found to be highly reproducible. To expedite the investigation, measurements were not taken for every experiment. Rather, measurements were taken of several distributions in every category. As a result of the large number of previously measured aerosol distributions, the distributions for the other experiments can be assumed with confidence.

CCN activation

Once the aerosol was injected, all three way valves were closed to the chamber, thus sealing the chamber, and the mixing fan was turned off. An ascent profile was computed on the computer and a checklist consulted. When all parameters were checked and at desired values, the ascent profile memory was enacted and the expansion began. During the expansion, for reasons explained in section 4.3, a person monitored the program pressure readout as well as the actual chamber pressure readout and adjusted the flowmeter accordingly to keep the actual pressure near the program pressure. The display readouts were monitored constantly to ensure all functions were operating as expected.

Data Collection

Several data were collected during the expansion. The important variables to this study were time, temperatures (air, wall, and program), chamber pressure, dewpoints (from both optical dewpoint hygrometers), calculated relative humidities (from both

optical dewpoint hygrometers), droplet size distribution and concentration, number of strobes encountered by FSSP, the velocity acceptance ratio of the FSSP and the calculated liquid water content. Data were recorded by the computer every one second and were extracted from an original file using two software programs.